ABSTRACT

Title of dissertation: NOVEL GRAPHENE HETEROSTRUCTURES FOR SENSITIVE ENVIRONMENTAL AND BIOLOGICAL SENSING

Michael Donald Pedowitz, Doctor of Philosophy, 2024

Dissertation directed by: Associate Professor Kevin M. Daniels, Department of Electrical and Computer Engineering, Institute for Research in Electronics and Applied Physics, Fischell Institute for Biomedical Devices

The COVID-19 pandemic has underscored the need for rapid, mobile, and adaptable sensing platforms to respond swiftly to pandemic-level emergencies. Additionally, smog and volatile organic compounds (VOCs), which posed significant health risks during last year's wildfires, highlight the critical need for environmental air quality monitoring. Graphene, with its high sensitivity and fast response times, shows promise as a powerful sensing platform. However, it faces challenges related to low selectivity and the complexities of device fabrication using conventional chemical vapor-deposited graphene grown on metal foil, which requires exfoliation and transfer to suitable substrates.

This dissertation explores the use of epitaxial graphene, which is graphene grown from the sublimation of silicon from silicon carbide, and forming heterostructures with legacy functional materials, such as transition metal oxides and selective capture probes like antibodies and aptamers to develop rapid, ultrasensitive, and selective sensors to address critical environmental and public health challenges. Epitaxial graphene provides a single-crystal, lithography-compatible graphene substrate that retains the desirable electronic properties of graphene without the drawbacks associated with transferred materials.

This work focuses on creating heterostructures using traditional functional materials, such as manganese dioxide and antibodies, to develop high-quality, selective sensors for both biological and environmental applications. The practical applications of these sensors are demonstrated and validated using techniques such as Raman spectroscopy, X-ray photoelectron spectroscopy, atomic force microscopy, scanning electron microscopy, and electrical characterization. Additionally, detailed material analysis on producing these heterostructures is provided, emphasizing their ability to be modified without damaging the underlying graphene surface. This highlights epitaxial graphene's robust and versatile nature and its potential for creating high-quality devices with relatively simple designs.

Finally, these biosensors are applied to alternate antibody-antigen systems, including influenza, to enhance disease-tracking capabilities. We also explore advanced functional materials, such as protease-peptide systems, which enable the creation of on-chip chemistry systems previously unattainable with current material systems.

NOVEL GRAPHENE HETEROSTRUCTURES FOR SENSITIVE ENVIRONMENTAL AND BIOLOGICAL SENSING

By

Michael Donald Pedowitz

Dissertation submitted to the Faculty of the Graduate School of the
University of Maryland, College Park, in partial fulfillment
of the requirements for the degree of
Doctor of Philosophy
2024

Advisory Committee

Associate Professor Kevin Daniels, Chair
Professor Pamela Abshire
Associate Professor Timothy Horiuchi
Professor Neil Goldsman
Wilson H. Elkins Professor Don Devoe

© Copyright by Michael Donald Pedowitz
2024 All Rights Reserved.

Dedication:
To my sister, Nichole, time to be Dr. Siblings

Acknowledgments

I am very thankful to the many people without whom this work would not have been possible. I would first like to thank my advisor, Dr. Kevin Daniels, for his guidance over the last five years. His presence and mastery of the field led to the work you see here today. Also, his love of discussion helped me get through some of the more challenging parts of this process. I would also like to thank Dr. Soaram Kim for developing the biosensors that have captured my attention in recent years and for helping me on my journey to understand characterization. In addition, I would also like to thank Dr. Pamela Abshire and Dr. Timothy Horiuchi for being on my committee and providing feedback through the candidacy process.

I would also like to thank Dr. Karen Gaskell, Department of Chemistry here at UMD, for assisting me in learning the XPS analysis and putting up with my endless quest to use the new instrument. Without her help, significant portions of this dissertation would not have been possible. I would also like to thank Dr. Don Milton, Dr. Sheldon Tai, and Dr. Don Devoe for providing support on biological systems when my own expertise was lacking. The University of Maryland has been a wonderful place to conduct my PhD; I wish them continued success.

I also deeply appreciate the support from the Naval Research Laboratory, particularly Dr. Racheal Myers-Ward, Dr. Dan Pennachio, and Dr. Jenifer Hajzus. Their contributions to the growth of the materials have been crucial to the completion of this dissertation. I also want to acknowledge Dr. Jimmy Kotsakidis at the Laboratory for Physical Sciences for his support in my material characterization efforts.

I am honored to have had the support of my lab mates and mentors at the Daniels Lab, Dr. Daniel Lewis, Brendan Jordan, Jenn DeMell, John Herboczek, and Weijian Xian. Their support and conversation helped me get through this PhD in one piece. I also thank Dr. Kurt

Gaskill, for taking time out of his retirement to provide pointers on presentations and research, without which I would not be as successful as I am today.

Finally, I would like to thank my family for their support throughout this process. My sister, Dr. Nichole Pedowitz, for not only helping me navigate graduate school but for being willing to collaborate with me despite the time difference. As well as my parents, Len Pedowitz and Nancy Bentz, for their support through this process and a roof for part of it. I would also like to thank my friends for standing by me despite months of work preventing us from spending time together. Late-night Dota 2 and LoL kept me sane for parts of this process. Thank you all once again for your support

Michael Donald Pedowitz

July 2024, College Park, MD USA

Table of Contents

List of Tables

List of Figures

Chapter 1: Introduction

COVID-19 (SARS-COV-2) proved to be a massive and disruptive force in the years between 2020-2022, with global impacts not seen since the Spanish flu in 1917[1]. Despite over a century of advancements in medical technology, the pandemic ravaged the globe, spreading to over 188 countries from November 2019 to April 2020[2]. One of the factors in this rapid spread was the lack of adequate and rapid testing for the virus. As of now, there are two methods of detecting SARS-CoV-2: polymerase chain reaction (PCR) based tests and “rapid” enzyme-linked immunosorbent assay (ELISA) based tests [3]. PCR tests rely on the amplification of existing virus RNA to a detectable level. This can detect the virus even in the early stages of infection but requires advanced laboratory equipment and can take over 24 hours to return results from the administration. Rapid tests detect the binding between antibodies and antigens, typically having immobilized antigens (such as the SARS COV-2 Spike protein) on the surface that react with antibodies the test subject has produced. This test can return results in as little as 10 minutes but can only detect the virus after a person’s viral load is already high enough to be contagious. It also is relatively inexact and suffers from significant false negative errors. As a result of these limitations, there is a lack of rapid and accurate point-of-care testing for not only COVID-19 but nearly all common infectious diseases, which limits our ability to control and monitor diseases as they move through society.

In a similar vein, the propagation of industrial technologies has significantly increased the production of many toxic gasses, including volatile organic compounds (VOCs) [4]. The effect of these gases on humans is not fully understood, but their toxicity has become increasingly apparent in recent years [5]. These risks exist even at concentrations that are colorless and odorless, benzene, for example, is highly carcinogenic with an occupation exposure limit of 0.05 ppm[6] but an odor threshold of 2.7 ppm[7]. This necessitates increased an more widespread air monitoring, especially around children who are more susceptible to these gasses[8]. The traditional method of detecting these gases is to use transition metal oxide sensors, which react readily with both redox and VOC gasses in a selective manner [9]. However, these sensors are limited by their high required operating temperature and have long response-recovery times, requiring large equipment to run. This severely limits conventional sensors ability to be deployed to many locations of interest.

High temperatures and laboratory analysis required in gas sensing and biosensing, respectively severely limit their ability to be deployed on a wide scale. Despite this, these techniques remain powerful in the detection and monitoring of health risks, and if these limitations could be removed, they would become an excellent tool for health monitoring. Graphene, a 2-dimensional (2D) layer of sp^2 carbon atoms and the first isolated 2D material, has attracted a massive amount of research interest since its discovery in 2004[10]. While initial research focused on the potential of graphene transistors[11], its ability to enhance existing functional materials has proven to be significant in a wide range of applications, including biological[12], gas[13], and light-sensing[14]. The key to these capabilities are the exceptional structural and electronic properties inherent to graphene. Graphene has a demonstrated mobility of 200,000 $cm^2V^{-1}s^{-1}$[15], a highly reactive surface[16], and strong coupling to nearby surfaces[17]. This allows it to significantly enhance the electrical properties of existing functional materials, such as transition metal oxides[18]. Additionally, graphene is, for its scale, one of the most mechanically robust materials known[16], allowing it to be used for the highly mobile applications necessary in the future.

As a result, we believe that using graphene-functional material heterostructures will allow us to fill the capability gaps mentioned above and allow for more accessible and wide-scale monitoring of a wide variety of important health topics.

From this, I derived determined the direction of this dissertation. We first developed a method of growing traditional functional materials, specifical manganese dioxide (MnO_2) on epitaxial graphene-silicon carbide structures. We then tested the enhancement of the gas sensing abilities of MnO_2 utilizing this heterostructure, especially in response to the VOC discussed above. This would allow for more widespread detection of these dangerous gases and more accurate real-time monitoring. In this proposal, we have focused on the growth of manganese dioxide (MnO_2) in its planar crystallographic phase, due to its ability to have a highly variable interlayer spacing. However, the principles of this growth can be applied to a wide range of functional metal oxides including WO_3 and ZnO, to produce graphene-metal oxide heterostructures. The discussion of this growth and characterization is in chapters 3-5 of this document.

We then moved on to develop a graphene biosensor based on the existing ELISA technique but enhanced by the superior properties of epitaxial graphene on silicon carbide. Including its compatibility with traditional fabrication and simple resistometric implementations [12]. Our initial results, indicated the ability to detect singular binding events with this sensor, causing us to investigate the mechanism of this response. As well as extending it beyond the SARS-COV-2 using the ELISA method to detect viruses, bacteria, and other pathogens. This portion of the dissertation is be discussed in detail in Chapters 7.

In this dissertation we have demonstrated the ability to grow consistent 50 nm thin films of epitaxially oriented layered MnO_2, with a surface roughness of 2 nm. These films have also been confirmed to be layered via mechanical exfoliation, with the production of 20 to 6 layers flakes after transfer. In addition, we have managed to transform these films via intercalation with alkali and alkaline metals (Na, K, Li, and Ca) as well as heat treatment producing Na-MnO_2, K-MnO_2, Mn_2O_3, and Mn_3O_4 without significant damage to the underlying graphene. We have also demonstrated low noise gas detection using the MnO_2 – QEG heterostructure, including a novel two-part response demonstrating gas sieving.

In addition, we have produced graphene biological sensors based on the traditional enzyme-linked immunosorbent assay, with a previously unseen limit of detection of 1 $agmL^{-1}$, three orders of magnitude lower than previously reported[12], with a <30s response time. I determined this ultra-low detection to be a strain-based effect due to the unique properties of epitaxial graphene, and have demonstrated the extension of this system to the peptide-protease system. This biological system had previously never had an electrical sensing mechanism and provided significantly more flexibility in targeting biological systems, making it a key area for research moving forward.

During my dissertation, I demonstrated the first electrochemical synthesis of MnO_2 on graphene as well as the first synthesis method of natively water-stabilized birnessite. I then used this heterostructure as a molecular sieve gas sensor, demonstrating the capability of graphene TMO heterostructures to reduce the limitations of pure TMO sensors. In addition, I developed a mechanistic description of the ultra-sensitive graphene ELISA sensor, discovering the lattice strain effect. I also expanded the initial ELISA design to both alternate antibody base ELISA and alternate biological molecules, using protease and peptides. On the basis of these discoveries, I seek a Doctorate in Philosophy in Electrical Engineering, and that work is described in this dissertation.

Chapter 2: Graphene

Section 2.1: Carbon Materials

Group IV materials, such as silicon and germanium, have long been the backbone of modern electronic systems. The first transistor was fabricated out of germanium[19], and after advances in surface science[20] silicon became the primary transistor material up to the modern day. A key property enabling these materials' semiconducting behavior is their tetrahedral crystal structure[21], which is not predicted by a naïve reading of their valence band orbitals. To account for this, we need to consider electron orbital hybridization, wherein the s and p orbitals in the valence band mix to form sp orbitals[22]. In lower period group IV elements silicon and germanium, this hybridization takes the form sp^3, where all s and p orbitals (p_x, p_y, and p_z) are mixed to form 4 orbitals of equal potential, which enables their tetrahedral crystal structure. Carbon, by contrast, exhibits three potential orbital hybridizations sp, sp^2, and $sp^{3,}$ which are exhibited in cyclocarbons[23], graphitic carbons[24], and diamond-like carbons[24], respectively.

These hybridizations exhibit vastly different properties that can be taken advantage of in various applications. Sp^3 carbons, or diamond-like carbons, are the hardest known materials [25], with excellent thermal conductivity and an excellent insulator (10^{16} Ω cm). Sp^2 carbons known as graphitic, see wide use in a variety of applications, from medicine, where activated charcoal is used to treat poisoning [26], to every day, where it is used in writing implements around the world. Even compounds previously only theorized to be synthesizable, sp hybridized carbons have been isolated in cyclocarbons, which demonstrated our continuing efforts to understand and harness carbon-based materials. To continued development of carbon-based materials may redifine what we already know about materials, as it did when we discovered the first two dimensional material graphene.

In the early 2000s, it was well understood that freestanding two-dimensional materials could not exist, and crystalline order could not be maintained at the monolayer limit [27]. Monolayer materials had been synthesized but only in growth processes on top of existing lattice-matched 3D materials [28]. This knowledge was upended when freestanding graphene was first isolated in 2004, demonstrating the possibility of 2D crystalline materials [10]. Since then, a vast array of two-dimensional materials have been isolated, including hexagonal boron nitride, a variety of transition metal dichalcogenides, and black phosphorous have been synthesized. Despite this proliferation of 2D materials, graphene remains of much interest due to its favorable physical properties and a wide array of applications.

Graphene has been demonstrated for use in biosensing [29], energy storage [30], and photodetection [31] among a vast array of alternate use cases. It has even been used to produce transistors [11] for next-generation electronics, which would pave the way to revolutionize modern computing. In addition, graphene can serve to enhance other materials, including transition metal oxides [32], transition metal dichalcogenides [18], and quantum dots [31]. It is this flexibility and versatility that continues to spur research into graphene 18 years on from discovery, and it is in part what motivated our use of this material in the remainder of this proposal.

Section 2.2: Graphene Structural and Electrical Properties

The electronic and structural properties of single-layer hexagonal symmetry sp^2 carbons have been studied extensively on the molecular level, as carbon rings (eg. Benzene) are the backbone of many organic systems. A key property of these systems is the delocalization of the electrons in the p_z orbital of the carbon atoms. These delocalized electrons are referred to as the π network, and from this aromaticity, is derived[33, 34]. The formation of this network is due to the hexagonal symmetry of the ring, as each carbon atom is equidistant to 2 nearest neighbors with which π bonds can form. Traditionally this degeneracy would be relaxed by structural deformation. However, the energy to distort the sp^2 σ bonds (17.1 kcal/mol) is significantly higher than that required to delocalize the system (11.8 kcal/mol), favoring the formation of the network [34]. The sensitivity of this network to distortion from functionalization, as seen by the high variation of aromaticity in organic compounds, further reinforces the importance of symmetry in the formation of the π network[33].

Graphene as a macroscale crystal of single-layer hexagonally symmetric sp^2 carbons has a similar delocalized π network, from which it gains many of its unique electronic properties. The macroscale nature of this system allows us to treat the system with traditional electronic and crystallographic methods, specifically band theory [35]. To analyze this system, we need to analyze the 2-dimensional Brillouin zone which has vertices at the K points. These K points segregate into two energetically distinct sets of points (K and K') due to the distinction between A and B sites in the crystal lattice. We can then derive a simple closed-form expression for the dispersion relation (equ. 1) of the π network over the Brillouin zone to determine the band structure. To do this we utilize the tight-binding model while neglecting the contribution of non-π electrons and non-nearest neighbors' which provides the closed-form solution.

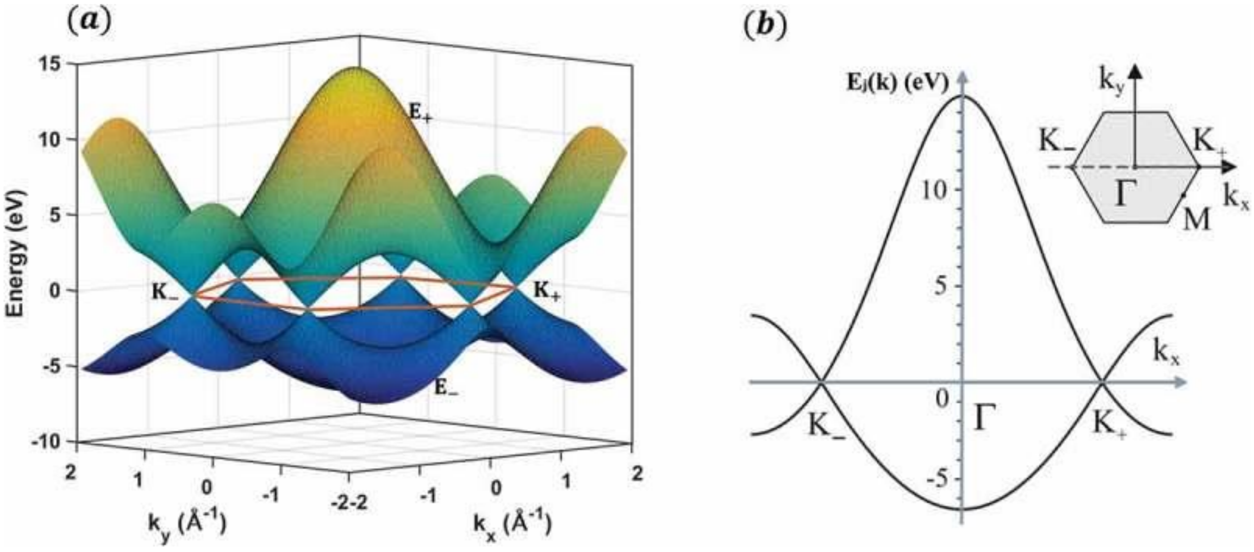

Figure 2-1 (a) Band structure of graphene calculated with a tight-binding. (b) Cross-section through the band structure, where the energy bands are plotted as a function of k_x along the line $k_y = 0$. Reproduced from [36]

$$E(k) = \pm\gamma_0\left[1 + 4\cos^2\left(\frac{1}{2}ak_x\right) + 4\cos\frac{\sqrt{3}k_x a}{2}\cos\frac{k_y a}{2}\right]^{\frac{1}{2}} \tag{1}$$

Where γ_0 is the transfer integral between nearest neighbors (~2.8eV), a is the atomic spacing of nearest neighbors (0.246 nm), and the $\pm$ differentiates between the (-) bonding $\bar{\pi}$ and (+) antibonding π^* bands [35]. A mapping of this dispersion over the Brillouin zone reveals that at the vertices (K and K') the bands overlap and become degenerate, which is termed the Dirac point. As a result, these regions dominate the electrical properties of the graphene system, and other effects can be excluded from the analysis.

A consequence of the dispersion relation is that near the Dirac point, the energy varies linearly with the wavevector, yielding the "Dirac Cone" band structure. As the electronic effective mass of a crystal is related to the dispersion relation by equation 2, the effective mass of electrons in graphene is ~ 0 [35]. This leads the theoretical carrier mobility in graphene to be on the order of $10^6 \frac{cm}{Vs}$ [37]. A caveat of this ultra-low effective mass is that it is only observable at the Dirac point, and will vary significantly with doping [38] and functionalization [39], which makes the realization of the theoretical carrier mobility of graphene nontrivial.

$$m^* \propto \frac{d^2E(k)}{dk^2} \tag{2}$$

This tight binding analysis provides good agreement with graphene operating undoped in a vacuum, however, as a two-dimensional material graphene is highly surface sensitive. As a consequence, substrates modulate graphene’s properties significantly. For example, SiO_2, the most commonly used transfer substrate, induces a native hole doping of 5×10^{12} due to physisorbed oxygen adatoms[40], as well as significant phonon scattering[41], which limit the mobility of these graphene structures to $10^5 \frac{cm}{Vs}$ [41]. An additional challenge of these structures is the necessity of transfer, which introduces structural defects in the graphene due to folding and wrinkling, which further limits the available mobility of graphene devices[40]. Unsupported or “Freestanding” graphene devices exhibit significantly enhanced mobilities, with reported mobilities in excess of $2 \times 10^6 \frac{cm}{Vs}$ [15], however, these devices require the physical placement of graphene ribbons on metal posts and are, therefore, not practical for electrical devices. The hole doping effect from placement on SiO_2 also demonstrates the ability of graphene to be chemically functionalized by non-covalent interactions. These interactions do not induce a significant defect density on the underlying graphene surface ($< 5 \times 10^{11} \frac{defects}{cm^2}$), and are fully reversible [40], which indicates they can be used to template the growth of materials on the graphene substrate [42]. The potential of this templating, in combination with electrochemical techniques, is what underlies the growth of manganese dioxide later in this work.

The stacking of graphene layers also produces significant changes to their electrical and chemical properties, as the material transitions to highly ordered pyrolytic graphite. Of particular interest is bilayer graphene where two graphene layers have been stacked on top of one another. The two most common forms of bilayer graphene are Bernal stacked (AB), wherein one graphene layer is laterally offset from the other by 1 unit cell, and AA stacked graphene with no lateral offset [43]. These two stacking orders exhibit significantly different electrical properties, with AA stacked bilayer graphene having a metallic character, and a Dirac cone band structure[43], and AB stacked bilayer graphene having a semiconducting character with a tunable bandgap of between 0-450 meV [44]. More recently "magic angle" (1.1°) stacked graphene bilayers have been found to have a superconducting transition [45]. Beyond stacking, order graphene's properties can also be modulated by additional structural changes, including patterning [46], edge termination [47], and edge passivation [48], which make it an excellent tunable substrate for electronic devices.

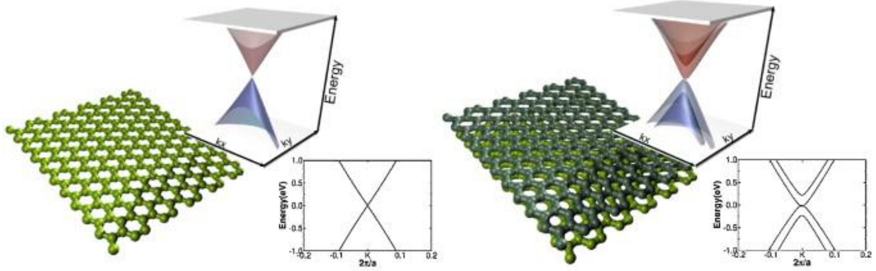

(a) Graphene

(b) Bi-layer Graphene

(c) Few Layer Graphene

(d) Graphite

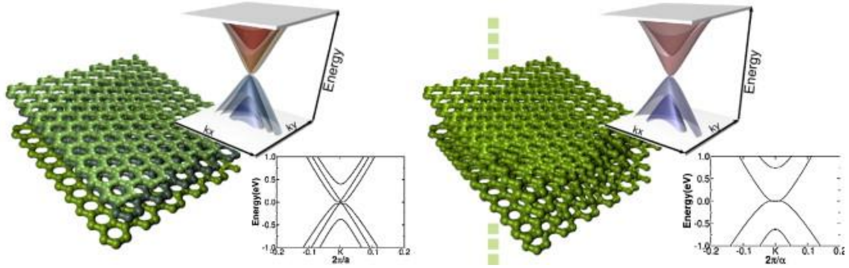

Figure 2-2: Low energy DFT 3D band structure and its projection on kx close to k point K (π/a[2/3, 0.0 0.0]) for (a) graphene, (b) bilayer graphene, (c) trilayer graphene and (d) graphite. Reproduced from [49].*

Section 2.3: Graphene Synthesis

The production of large-scale electronics-quality graphene has been the subject of significant research since the initial synthesis of the material by mechanical exfoliation in

2004[10]. The traditional mechanical exfoliation method uses commercial adhesives, traditionally scotch tape, to peel off atomically thin layers from a layered bulk substrate[50], which for graphene is highly oriented pyrolytic graphite. This method has since been applied, with great success, to the production of many 2D materials, including MoS_2, WSe_2, and WS_2[50]. However, mechanical exfoliation has many limitations that make it unsuitable for use outside of the laboratory setting, including small grain sizes[51] (<100 μm), inconsistent layer numbers[51], and high process variability[51]. More complex methods of mechanical exfoliation have been utilized, including ball milling, solution exfoliation, and ultrasonication. Still, they suffer from significant sp^3 defect density and low crystallinity and are, therefore, also not suitable for the construction of large-scale electronic devices[52].

Two primary methods have been found to produce suitably large-scale, low-defect density graphene. Metal-catalyzed chemical vapor deposition[53], typically onto a copper or nickel foil, and epitaxial growth on SiC via selective sublimation of Si from the 6H-SiC polytype[54]. In chemical vapor deposition growth, the decomposition reaction (eq. 3) of hydrocarbon gases in the presence of a catalytic metal surface at elevated temperature (~1000°C) is utilized to provide reactive carbon to the growth substrate[53, 55].

$$\mathrm{CH_x + M \rightarrow CH_{x-1} + M + H} \qquad (3)$$

These carbons then subsume into the metal surface based on the metal's carbon solubility at the growth temperature, during cooling the carbon then precipitates on the surface to form graphitic structures[53, 55]. Among the metal catalysts, Cu has seen the majority of the experimental work, as its carbon solubility is very low, causing the decomposed carbon atoms to remain at the surface. This causes them to grow a self-terminating single layer of graphene, which prevents additional growth by inhibiting the decomposition reaction in the chamber. Using this method monolayer graphene sheets with grain sizes on the order of 1 mm[56] have been successfully synthesized. Once synthesized, CVD graphene can then be transferred onto any arbitrary planar substrate with limited defecting[57], primarily in the form of graphene wrinkling[57] and functionalization[53]. As a result, CVD graphene has been the primary form of graphene used for electrical devices. However, the polycrystallinity of the film[58], as well as the coupling effects between transferred graphene and its substrate[40] inhibit the use of these materials in macroscale and ultra-high sensitivity applications, like biosensing.

Of particular interest in this work is the growth of epitaxial graphene on silicon carbide, which can produce nominally single crystal wafer scale bilayer graphene[59]. These structures also exhibit excellent electrical properties after intercalation, with room temperature mobilities greater than 3000 cm^2/Vs[54]. The principle idea of this growth method is to take advantage of the hexagonal symmetry of 6H-SiC, as well as the significantly higher sublimation speed of silicon at elevated temperatures to selectively sublimate out silicon atoms, leaving behind a carbon layer that can form graphene[60]. The general process for growth from the silicon face is as follows: initially slightly off-axis (~0.05°) 6H-SiC is placed in a hot-walled reactor and hydrogen etched at elevated temperature (1570-1600°C)[60]. This serves to remove surface damage and defects and reveals (0001) terraces and $(11\bar{2}0)$ step edges, which will serve as the primary growth sites for the epitaxial graphene[61-63]. The SiC is then exposed to an Ar ambient at this elevated temperature, to selectively sublimate silicon out of the step edges, producing multi-layer graphene structures, with layer count depending on growth duration. The Carbon face $(000\bar{1})$ can be used but in a similar process, but the resulting graphene has poor crystallinity and high defect density, and therefore is not targeted in the literature[61-63].

The bottom-most carbon layer of the as-grown epitaxial graphene on the (0001) face is covalently bonded to the silicon carbide surface due to dangling bonds with a $(6\sqrt{3} \text{ x } \sqrt{3})$ R30° structure[63]. This buffer layer induces large n-type doping into the grown graphene layers [64]. It also contains a significant amount of localized states and strongly couples the surface phonons of the silicon carbide to the graphene layers, significantly reducing the mobility of the EG – SiC structure[63]. To release this layer and remove these effects, the silicon carbide dangling bonds can be passivated via hydrogen intercalation, which promotes the buffer layer into an additional graphene layer and causes it to be "quasi-freestanding" [65]. This gives the graphene all the advantages of a freestanding layer, high mobility, and limited substrate effects while also having the advantages of the silicon carbide substrate. This makes the quasi-freestanding epitaxial graphene silicon carbide structure (QEG) uniquely advantageous among graphene structures for large-scale and sensitive device design, as proposed in this work. As such, it is what we utilized for the remainder of the work.

An Aixtron/Epigress VP508 horizontal hot-wall reactor was used to grow the QEG used in this work. Initially, the semi-insulating 6H-SiC wafer is etched during the temperature ramp to 1570 °C in 5 slm of high purity H_2 at 200mbar. This is then switched to 100mbar of high purity Ar at 1580 °C for twenty minutes, which synthesizes monolayer graphene. The reactor is then cooled to 1050 °C in Ar and switched to 80 slm of H_2 at 900mbar for an hour to intercalate the structure and release the buffer layer, forming bilayer QEG.

Section 2.4: Graphene-Modulated Functional Materials

Recent advances in materials development have generated a vast number of functional materials and structures with advantageous properties in the areas of energy storage [66], sensing [67], and catalysis [32], among others. Despite this, many of these materials have poor electrical or structural properties that inhibit their use in devices. For example, colloidal quantum dots (CQD) can act as highly tunable photodetectors with high quantum efficiency and low production costs [14, 31]. However, these devices suffer from poor response and response times in part due to the very low mobilities of photocarriers in quantum dots [14, 31]. To overcome this challenge, heterostructures have been formed between graphene and CQDs, which utilize the graphene as a conduction layer for the excited photocarriers, and these heterostructures have significantly improved the performance of these devices [14, 31].

Similarly, heterostructures have been formed between graphene and transition metal oxides (TMOs), and transition metal dichalcogenides (TMDs). Which seeks to couple the advantageous properties of both materials for use in electrical devices. Transition metal oxides in a particular couple very strongly with graphene layers, due to the large electronegativity difference between oxygen (3.44 eV) and carbon (2.55eV) atoms [32]. This induces significant hole doping in the graphene layers and can modulate both the band structure and the fermi level of the TMO [32]. Despite the magnitude of the coupling, this non-covalent functionalization of the graphene does not inhibit the normal function of the π network and, therefore maintains the favorable electrical properties of the graphene[68]. For this reason, graphene transition metal oxide heterostructures have been found to enhance the properties of MnO_2, TiO_2, and ZnO, among others, which motivated parts of this work[32].

Section 2.5: Graphene Biosensors

In addition to its use as an enhancement to functional materials, the high sensitivity of the graphene surface has been utilized to produce a wide variety of highly sensitive biosensors. However, a key challenge of all graphene sensors is their low selectivity [13], which can generate a high false positive rate. This is particularly problematic in the biological context, wherein false positives can lead to expensive treatment and a misallocation of resources. To prevent this, graphene can be functionalized with specific biomarkers [29, 69, 70], which allows for the selective detection of diseases. These functionalized graphene sheets can then be analyzed either optically or electrically to detect the desired disease [71].

The most common optical graphene biosensors are those based on the modulation of surface plasmon resonances with the binding of a target antigen. The central idea is that functionalized graphene ribbons have a native graphene plasmon resonance frequency [54] and that the binding of the analyte with the target will produce a shift in this resonance [72]. This has been successfully demonstrated in the literature and has low limits of detection on the order of 100pM. However, the challenge of these optical devices, is that the extraction of electrical information from surface plasmons is not trivial, and the need for laser excitations limits their ability to be used as a point of care [54]. Another common optical biosensor relies on surface-enhanced Raman spectroscopy, which suffers from similar issues in terms of required equipment, limiting the usability of these sensors [71].

Due to these equipment requirements, electrical biosensing is more desirable for point-of-care diagnostics. To produce these sensors the functionalized graphene is assembled into graphene field effect transistor (GFET) devices that can transduce the concentration of an analyte via changes in the electrical properties of GFET. These sensors have been demonstrated to be highly sensitive, with sensitivities up to 1 fg/ml [71]. However, significant challenges remain in the production and use of these graphene biosensors. Graphene can be readily and robustly functionalized, but stable non-covalent functionalization remains challenging [73]. As the high sensitivity and favorable electrical properties of graphene rely on the sp^2 order of the graphene, this means that non-covalent functionalization is required to produce high-quality electrical biosensors. In addition, resistometric biosensors [69] have poor demonstrated responsivity and high noise, requiring the production of complex gated or solution-gated GFET devices [29, 70], which are challenging to produce and use in a clinical context. This set of challenges leaves a gap in the biosensing space for higher-quality electrical biosensors without requiring complex solution-gated FETs, which is another motivation behind this work.

Chapter 3: Growth and Transformation of Manganese Dioxide on Epitaxial Graphene Silicon Carbide

Section 3.1 Transition Metal Properties

Transition metal-based materials, molecules centered on metals with partially filled d orbitals [74], exhibit a wide variety of tunable properties, including magnetism [75], redox activity [76], and non-linear optical response [77]. This has made these materials the subject of extensive research over the past century. Additionally, the presence of layered crystalline phases in these materials has made them excellent candidates for the production of low-dimensional and two-dimensional materials [18]. As a result, transition metal dichalcogenides have become the most explored two-dimensional materials after graphene [18]. In addition to transition metal dichalcogenides, other transition metal complexes have been explored, including transition metal oxides, which will be the focus of the remainder of this chapter.

Key to the variable properties of transition metal materials is the complex physics of d orbitals and d orbital bonding [74, 78-82]. D orbitals, which appear in the third electron shell, are highly screened from the nucleus by the other same shell electrons. This can be seen clearly in phosphorous wherein the energy of electrons in the 3d orbital are at least 0.5 eV above that of the 4p orbital and 1 eV above the 4s orbital [83]. This leads to the d orbitals being significantly larger and more diffuse than lower-order orbitals and enables their more complex electron interactions by allowing for stronger electron-electron interaction [84]. Additionally, the manner in which d orbitals affect bonding and the formation of transition metal complexes is non-trivial, as seen by the contentious debate around the formation of SF_6 [85]. It is in part for this reason that transition metal materials have commanded such extensive research in the literature, in addition to their capabilities as powerful functional materials.

Section 3.2: Transition Metal Oxide Overview

Among the transition metal complexes of interest, transition metal oxides are of particular interest due to their high redox activity [86, 87]. A key factor in this redox activity is the hybridization of the O 2p and Metal d orbitals, which can form an accessible delocalized electron system similar to the π network seen in graphene [88]. In addition, due to their accessible d orbitals, transition metal oxides exhibit Jahn-Teller distortion, wherein degeneracy in the d orbital electron energies leads to structural distortion in the crystal structure, enhancing the chemical-physical coupling of these materials [89].

These materials also exhibit a wide variety of crystalline polymorphs due to their octahedral and tetrahedral symmetry, as well as multiple accessible valence states [90]. Among these are several layered oxides (MnO_2, VO_2, ZnO, as well as ABO_3 perovskites) that have traditionally been used in energy storage applications[91]. They have also been the targets for transformation to 2D layered transition metal dichalcogenides as more exotic transition metals have been targeted [92].

As a result of all these factors, transition metal oxides have seen significant use throughout human history in energy storage [93], gas sensing [94], and catalysis [95], and continue to see significant research interest from the community, even as more exotic materials rise to the forefront.

Section 3.3: Transition Metal Oxide Gas Sensing

A key application that transition metal oxides target is gas sensing due to their high redox activity. These sensors have been used to detect both the more common redox active gasses, eg. NO_2 and NH_3[76, 94, 96], as well as volatile organic compounds (VOCs) like benzene[76]. These devices have managed to detect gasses down to the ppt level [97]. However, the operation of these sensors has been limited by the low inherent conductivity of these metal oxides, requiring elevated temperatures in order to operate effectively [9, 76, 98]. This limits their operability outside of a controlled environment and availability to the public.

To overcome these challenges, heterostructures have been formed between transition metal oxides and graphene. The purpose of this is to enhance the conductivity of the transition metal oxides by allowing the conduction path of the sensor to be the graphene[42, 76, 94, 96] and reducing their operation temperature. In addition, nanostructuring of the oxides, in order to improve active surface area and decrease conduction path length, has also been attempted to improve the operability of these sensors[42, 76, 94, 97].

As a result of these efforts, room temperature gas sensors produced from transition metal oxides have managed to detect gasses on the order of 1ppb with response/recovery times on the order of 20 minutes, which is a significant improvement over previous results[42, 76, 94, 97]. As a result, we have targeted the creation of transition metal oxide graphene heterostructures as one of the main efforts in our attempt to provide improved environmental monitoring on the easily transportable epitaxial graphene platform.

Section 3.4 Growth of Manganese Dioxide on Epitaxial Graphene-Silicon Carbide Substrates

As discussed previously (see C. 3) traditional functional materials have significant limitations in their deployment. Transition metal oxides, for example, require elevated temperatures and complex nanostructures to produce the best results in energy storage[99], catalysis [100], and environmental sensing [9]. To overcome this, we sought to produce heterostructures with epitaxial graphene to enhance the operating properties of the transition metal oxides and expand the operation range of these functional materials [9].

The transition metal oxide family that we elected to focus on in producing this heterostructure was manganese oxides (MnO_x) due to their wide variety of stable oxygen stoichiometries (MnO_2, Mn_2O_3, Mn_3O_4, and MnO) with highly tunable crystal structures ($\alpha, \beta, \gamma, \delta, \epsilon \ldots - MnO_2$, $\alpha, \beta - Mn_2O_3$) [6]. In addition, these materials have seen significant interest and have been successfully utilized in catalysis [101] and energy storage [102-104] and have demonstrated novel magnetic properties in the low dimensional limit[105]. As catalysts, these MnO_x structures are comparable to noble metal catalysts, e.g., T_{100} = 240ºC for toluene reduction vs. T_{100} = 230ºC for platinum-based catalytic systems [95, 101]. In energy storage MnO_x, materials are a primary contender for cathodes in next-generation multivalent battery systems (Zn/Zn^{+2}, Al/Al^{+3})[102, 103]. However, the low electrical conductivity (10^{-5}-10^{-6} S) of MnO_x compounds[106, 107], significantly reduces the speed of the surface redox reactions used to drive catalysis and energy storage. For this reason, heterostructures formed with high-quality graphene are desirable.

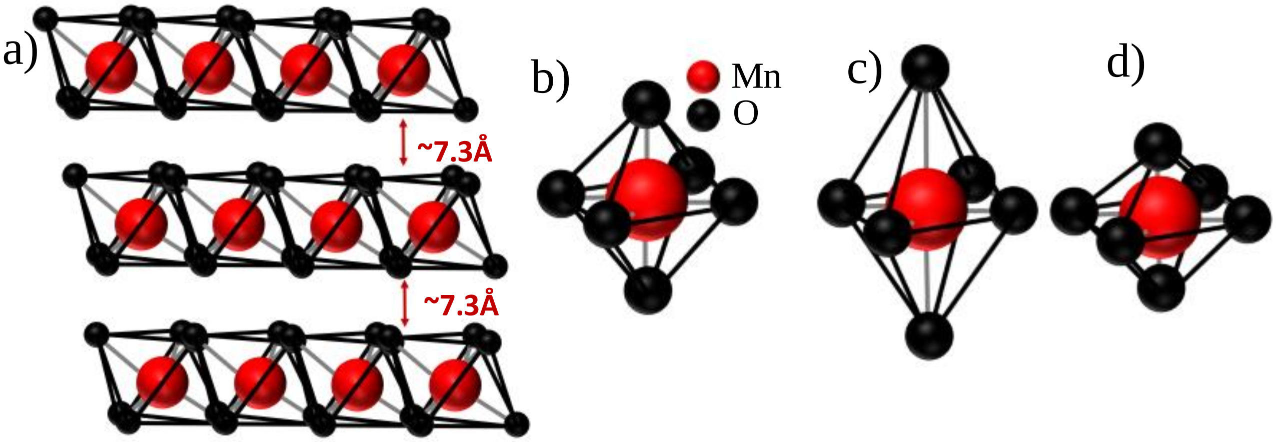

Figure 3-1: (a)Ideal Layered Structure of Layered Manganese Dioxide (the Birnessite or δ phase)[108].(b) The MnO_6 Octahedra which can undergo strong Jahn-Teller distortion either via (c) elongation or (d) compression. This allows for strong structural control and physical chemical coupling, improving the reactive properties of the structure[89].

Section 3.5 Growth of Manganese Dioxide on EG/SiC Substrates

A wide variety of methods have been demonstrated to grow MnO_x on graphene. Manganese dioxide, the most widely studied MnO_x compound, has been successfully synthesized via hydrothermal [93], solvothermal [109], microwave-assisted [110], and co-precipitation [111] methods. These methods, however, rely on modified Hummer's methods to produce MnOx-graphene heterostructures. These methods, however, rely on modified Hummer's methods to produce MnO_x-graphene heterostructures. Modified Hummer's methods produce graphene oxide and reduced graphene oxide via the reaction of permanganate salts (e.g., $KMnO_4$) with graphite [93]. This significantly reduces the conductivity of the resulting heterostructure as reduced graphene oxide has carrier mobilities and conductivities 2-3 orders of magnitude lower than pristine graphene[112]. These methods also rely on harsh oxidizers, raising significant environmental concerns, and are incompatible with the large crystal size, high-quality graphene that has been produced through both sublimation of silicon carbide [54] and CVD deposition on copper[113]. To create the final solid heterostructure precipitate, these methods also require a long high-temperature step (~12 h, >500ºC) [93] which makes them impractical for large-scale synthesis.

To overcome this limitation, we explored an alternative method to grow MnO_2 on graphene, electrochemical synthesis. Previous work has demonstrated that EG can be functionalized electrochemically with O^- groups, which, unlike H^+ functionalization, is independent of surface defects[114]. Based on this, we believed that by utilizing these O^- groups as nucleation sites, we could deposit MnO_2 on pristine epitaxial graphene consistently and with good control over crystalline structure. We used a three-electrode electrochemical cell with a QEG working electrode (grown in a process discussed in chapter 2), a Pt counter electrode, and an Ag/AgCl reference electrode. Manganese acetate (MnAC, Sigma Aldrich, 98% purity) solutions were used as the electrodeposition electrolyte solution with concentrations from 100 mM to 2.5 mM. The MnAC solution was mixed immediately before the reaction to avoid oxidation, as indicated by the precipitation of brown MnO_2 particles in the solution. δ-MnO_2 was deposited using a three-step reaction controlled by a potentiostat (Gamry 3000) at the redox potentials. Redox potentials are determined by cyclic voltammetry(CV, Figure 3-2.a), where potentials are cycled for five cycles with a -2.5 V to 2.5 V potential window and a scan rate of 10 mV/s. According to CV, the oxidation potential was found to be 2.1 V, which was then lowered to 1.858 V for reaction to reduce the risk of graphene oxidation. The reduction potential of MnAC on QEG was determined to be -0.4 V. The potential for each step was 1.858 V, -0.4 V, and 1.858 V vs. Ag/AgCl, with growth times from 920s to 0.5s (Figure 3-2.b).

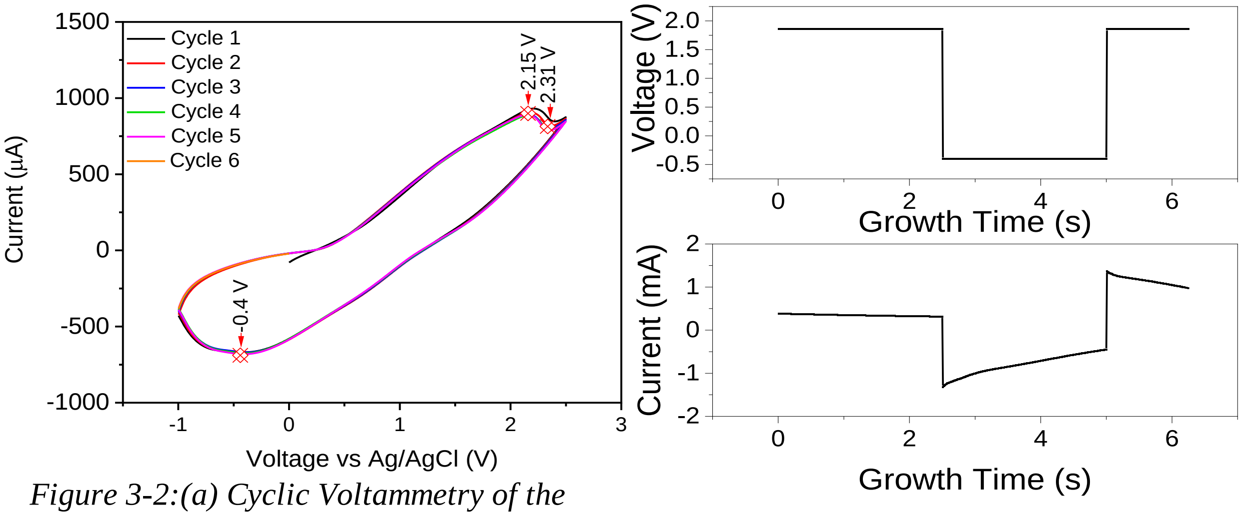

Figure 3-2:(a) Cyclic Voltammetry of the QEG-MnAC-Pt system, example three pulse electrodeposition voltage (b) and current (c) curves. In the Cyclic Voltammetry Curve, we can see one reduction potential (-0.4V), and two oxidation potentials (2.15 V and 2.31V) from which we chose our deposition potentials.

Following electrodeposition, a semi-transparent brown film formed on the QEG surface with large grain sizes (>100 μm) and distances between grains, from grain boundary to grain boundary (~1 μm), penetrating to and revealing the underlying QEG substrate. To observe how varying growth conditions affect the quality and thickness of the deposited δ-MnO_2, the first pulse duration, third pulse duration, solution molarity, and total growth duration were varied to determine optimal growth conditions, which are discussed in detail in section 5-2.

To confirm the formation of δ-MnO_2 on the QEG substrate, the materials were characterized by a combination of Raman spectroscopy, XPS, AFM, and SEM. These techniques allow us to probe both the material quality and the surface characteristics of the resulting films, which allows us to determine the optimal growth conditions to produce high-quality δ-MnO_2.

Raman spectroscopy allowed us to confirm the formation of δ-MnO_2 as it has a distinct Raman spectrum from other materials and MnO_2 polymorphs [66]. Group theory calculations predict nine active Raman bands in δ-MnO_2 ($3A_g+6B_g$). The most intense of these bands have been reported at 500-510 cm^{-1}, 575-585 $cm^{-1,}$ and 620-650cm^{-1} [66, 108, 115]. These modes have generally been assigned to the Mn-O-Mn deformation mode, the Mn-O-Mn stretching mode in the basal plane, and the Mn-O-Mn stretching mode of the characteristic octahedra, respectively [116]. Additional low-intensity peaks at 710-730 cm^{-1}, 610-630 cm^{-1}, and 390-410 cm^{-1} have been reported in the literature but have no physical assignment at this point. α-MnO_2 or 2x2 tunnel phase has a similar Raman spectrum, but clear differences appear in the low IR region where α-MnO_2 has a strong band at 180cm^{-1}, related to its tunnel structure [66]. By contrast, δ-MnO_2 has a low-intensity band at 120-130cm^{-1} related to the vibration of interlayer H_2O molecules. To collect the Raman spectra of our material, we utilized a Horiba LABRAM ARAMIS system using a 532nm excitation source with a spot power of 14.7 µW. After the spectra were captured, they were then processed by subtracting a known QEG background and fitted using pure Lorentzian line shapes. In these collected Raman spectra (Figure 3-3), three characteristic Raman peaks at 501 cm^{-1}, 576 cm^{-1}, and 652 cm^{-1}, as well as a weak band at 120 $cm^{-1,}$ were observed. This indicates that δ-MnO_2 on QEG was formed. Also visible in the Raman spectra was a weak peak at 617 cm^{-1}, attributed to defect phases in the MnO$_x$ structure [108], which was utilized to track material quality with changing growth conditions. The Raman spectra also indicated that the epitaxial graphene was undamaged as there was no formation of a visible D peak, and the 2D peak FWHM remained at 66 cm^{-1}, indicating the maintenance of the bilayer character of the epitaxial graphene film [54].

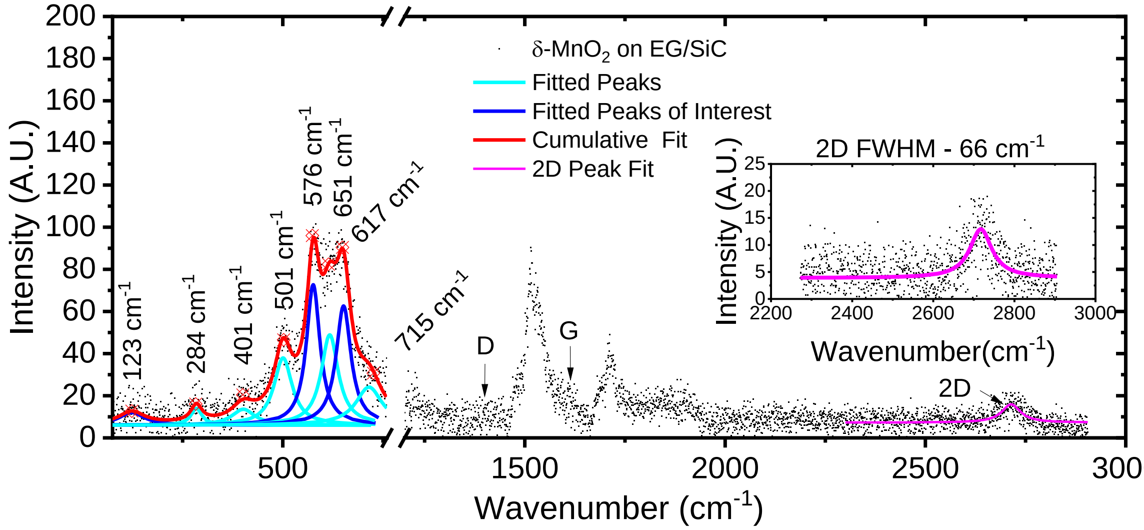

Figure 3-3. Raman spectra of δ-MnO$_2$ on QEG substrates. Visible in the spectrum are the characteristic peaks at 651 cm^{-1}, 576 cm^{-1}, 501 cm^{-1}, and 123 cm^{-1}, which indicate the formation of δ-MnO$_2$. A weak peak is also observed a 617 cm^{-1} which is associated with defected MnO$_x$ materials, which we tracked to determine the material quality of the resulting films

To further verify the formation and quality of the as-grown δ-MnO$_2$, XPS was used due to its high sensitivity to elemental composition, as a simple linear relationship has been found between the 3s peak splitting and the formal oxidation state of manganese[117]. To collect this XPS data, a Kratos Axis 165 X-ray photoelectron spectrometer operating in hybrid mode using monochromatized Al Kα radiation (ħω=1486.7 eV) was used, at an anode power of 280 W and a base pressure of 5×10^{-8} torr. The survey spectra and high-resolution spectra were collected at pass energies of 160 eV and 40eV, respectively. The high-resolution spectra were then deconvoluted using 30 percent Lorentzian Gaussian-Lorentzian line shapes and a Shirley background for fitting. In the survey scan of our as-grown δ-MnO$_2$, the only significant elements found were Mn, O, Si, and C, consistent with water-stabilized birnessite, as opposed to K or Na type birnessite (Figure 3-4.a). Additionally, our observed Mn 3s spectra exhibited a peak splitting of 5eV, indicating a formal oxidation state of +3.33 (Figure 3-4.b). Using this in combination with the collected Raman spectra, the optimal growth conditions for high-quality thin films were determined.

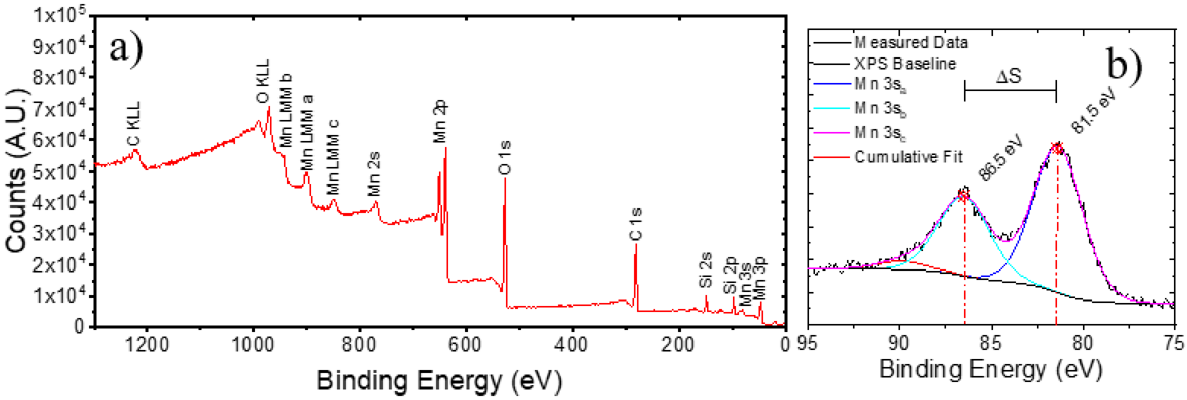

Figure 3-4. XPS (a) survey spectra, (b) 3s region spectra of δ-MnO_2 *on QEG substrates. Observed here is a 5eV separation between the Mn 3s peaks, which using the linear relation between splitting and formal oxidation state (8.965-1.126ΔS) indicates a formal oxidation state of +3.33, as well as a lack of alkali metal ions indicating a high defect density water, stabilized birnessite*

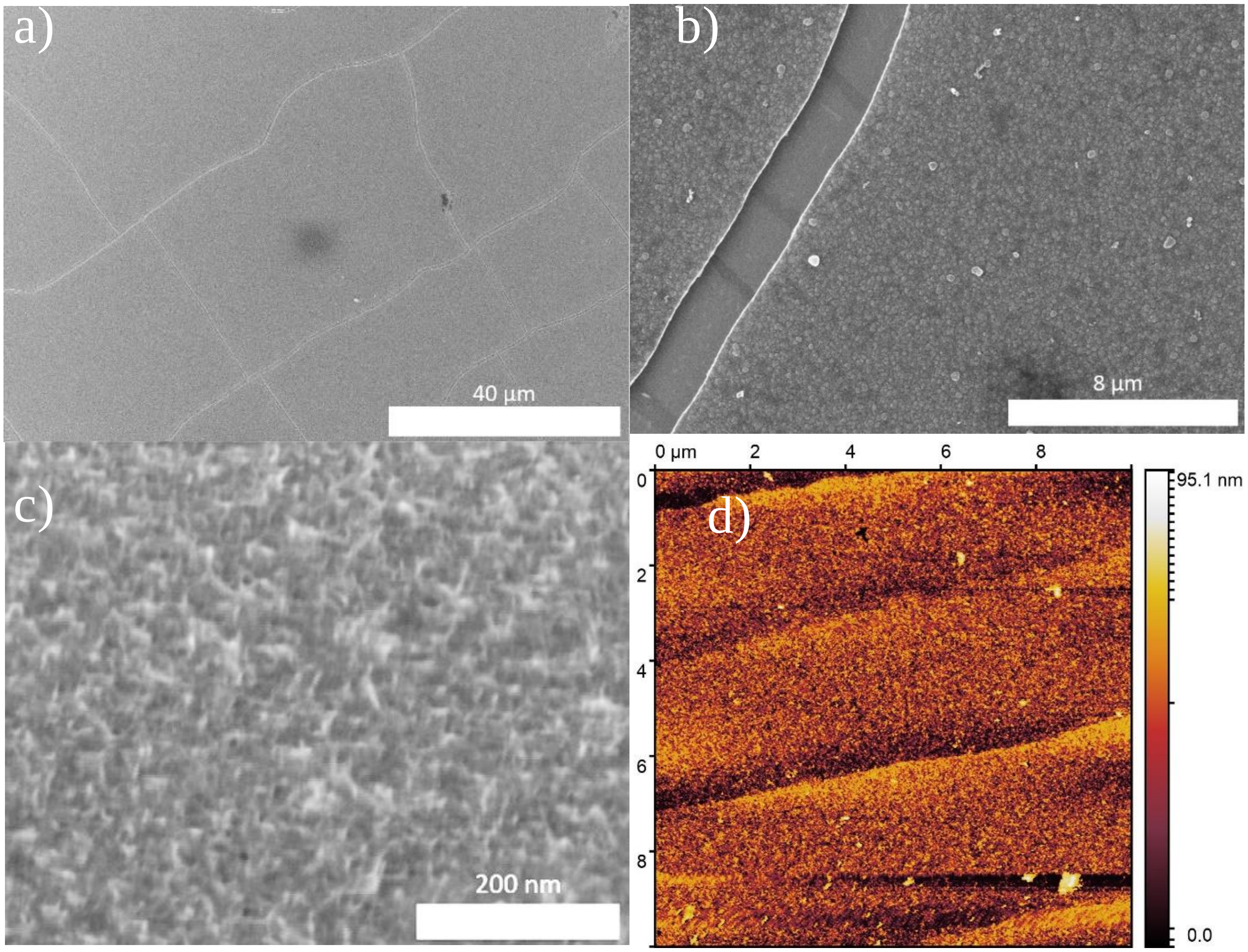

Figure 3-5. SEM (a-c) and AFM (d) images of δ-MnO_2 on QEG. The SEM images were taken at (a) 1Kx and (b) 5Kx and (c) 80Kx. They indicate the surface is made up of rectangular microplatelets greater than 40 µm by 40 µm. the higher magnification image reveals that these cracks are perpendicular to the graphene step edges, and the surface is made up of nanofibrous particles. AFM imaging indicated the surface was quite smooth, with a surface roughness (Ra) of ~2.5nm.

To characterize the surface morphology of the resulting thin films, a combination of SEM and AFM was used to obtain surface morphology, roughness, and approximate thickness of the deposited thin films. SEM analysis of the film revealed that the film is made of rectangular microplatelets with sizes of approximately 50 µm x 30 µm (Figure 3-5.a). The long axis of these rectangular microplatelets was generally perpendicular to the SiC step edges (Figure 3-5.b). This indicates that the formation of these platelets was related to a lattice strain between the δ-MnO_2

and SiC. This is consistent with the known lattice mismatch between 6H-SiC and δ-MnO_2, which share a hexagonal crystal structure with lattice constants a = 3.08 Å [116] and a = 2.84 Å [118], respectively. This is further corroborated by the fact that these cracks do not form immediately but form during the drying procedure. Higher magnification SEM images indicated that the surface of these microplatelets is made up of randomly oriented nanofibers, with widths of approximately 10nm. As active surface area is a key predictor of transition metal oxide performance, this nanofibrous surface is highly desirable in the formation of MnO_2- QEG heterostructures (Figure 3-5.c). AFM imaging of the heterostructures confirmed that they were formed into microplatelets made up of nanofibrous nanoparticles. In addition, they indicated that these films were approximately 50nm thick, or ~26 layers of δ-MnO_2 manganese dioxide, and had a surface roughness of 2.5nm in the optimal growth condition(Figure 3-5.d).

Section 3.6 Optimization of Manganese Dioxide Growth Conditions

Electrochemical synthesis of materials is very sensitive to relatively minor changes in growth conditions, which allows us to control and tune the deposited heterostructure by varying these conditions. Using this method, the aim was to find the optimal growth procedure to produce high-quality thin films, which are considered to be the thinnest, lowest roughness film possible with a relatively high defect density [119]. The high defect density is desirable as it improves the reactivity of the resulting films, and the low thickness improves charge transfer to the underlying graphene sheet. To achieve this, we varied the pulse durations and the solution molarity in several series, which are described below in Table 3.1.

Table 3.1 Growth Variables for the Electrochemical Synthesis of MnO_2 on QEG

Variable Swept	First Pulse Duration (s)	Second Pulse Duration (s)	Third Pulse Duration (s)	Total Duration (s)	Solution Molarity (mM)
Third Pulse Duration	600	20	300 to 20	920 to 620	100
First Pulse Duration	600 to 20	20	0	620 to 40	100
Solution Molarity	20	20	0	40	100 to 5
Total Duration (Ratios Constant)	15 to 0.5	15 to 0.5	7.5 to 0.25	37.5 to 0.5	20
Solution Molarity	0.5	0.5	0.25	1.25	20 to 2.5

To observe the change in material quality with varying growth conditions, the change in the ratio between the 575-585 cm^{-1} peak, which is related to basal plane phonon modes in the layers (V_1), and the peak at 610-620 cm^{-1}, related to MnO_x defects in the structure (V_b) was tracked. This gives insights into the structural order in relation to the defect quantity in the material. The variation of Mn formal valence to confirm these observations, which were well-correlated to the change in the V_1/V_b ratio, indicating the veracity of this method. was also followed. The surface thickness and roughness were also monitored to improve material quality.

First, the third pulse duration was varied, with decreasing third pulse duration resulting in increases in the V_1/V_b ratio as well as increases in the formal valence. This indicates that shorter third pulses improve material quality. However, upon removing the third pulse entirety, both metrics decrease (Figure 3-6.a), indicating that a short, nonzero third pulse is desirable for good growth. It was also found that for third pulse durations longer than the 60s, a thick black “crust” layer formed on the surface. Upon reducing the third pulse time to 60s, the entire film delaminated during the growth (Figure 3-6.b), implying that the crust layer may have been formed by the delaminated film adhering to new growth on the surface. We also observed that these films had a thickness greater than 10 um, which we found undesirable for gas sensing via molecular sieving.

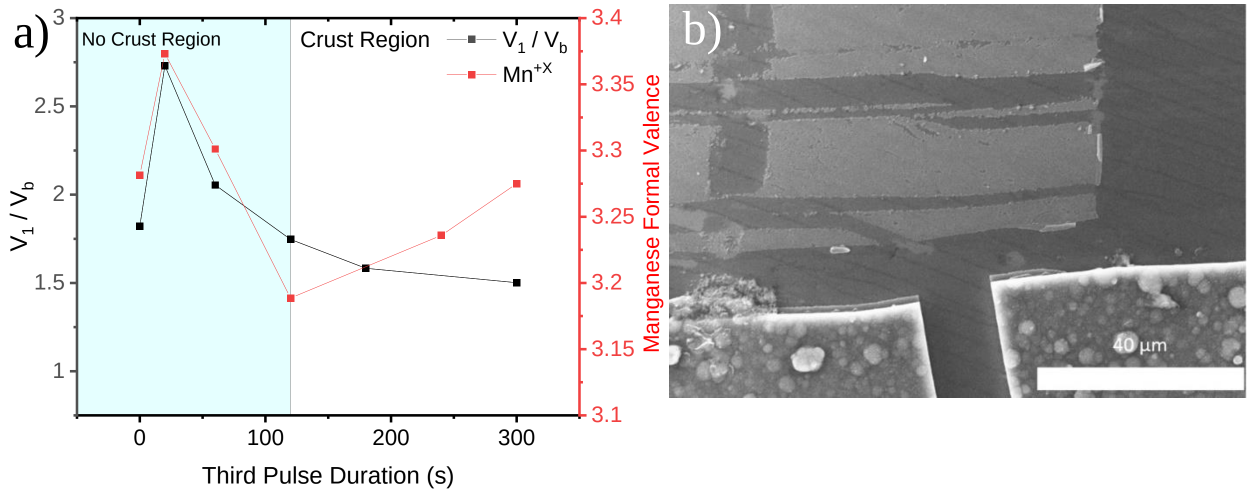

Figure 3-6: (a) Graph of the variation in the ratio between the Basal plane Raman peak at 575 cm-1 (V1) and the potential defect peak at 610 cm-1 (Vb) and the variation in manganese formal valence from the Mn 3s peak splitting with third pulse duration, with a first and second pulse duration of 600 s and 20 s respectively. (b) SEM image was taken at a third pulse duration of 60 s, showcasing significant delamination of the film at this duration. From this data, we observed that during long third pulses, the quality of the material is reduced, and there is the formation of an upper "crust" type layer with poor adhesion, after reduction of the third pulse duration under we see a significant increase in formal valence and Raman ratio, as well as the suppression of the "crust layer" formation.

No strong correlation between the first pulse duration and film quality was observed when a third pulse was omitted. The variation of Raman ratios and formal valence indicated that its effect on material quality was inconsistent (Figure 3-7). However, a reduced first pulse duration was very well correlated (R^2=0.92) with film thickness and film roughness, with a decrease in thickness from 1200nm to 100nm at the lowest duration (Figure 3-7). As a result, a first pulse duration of 20s was selected for growth optimization.

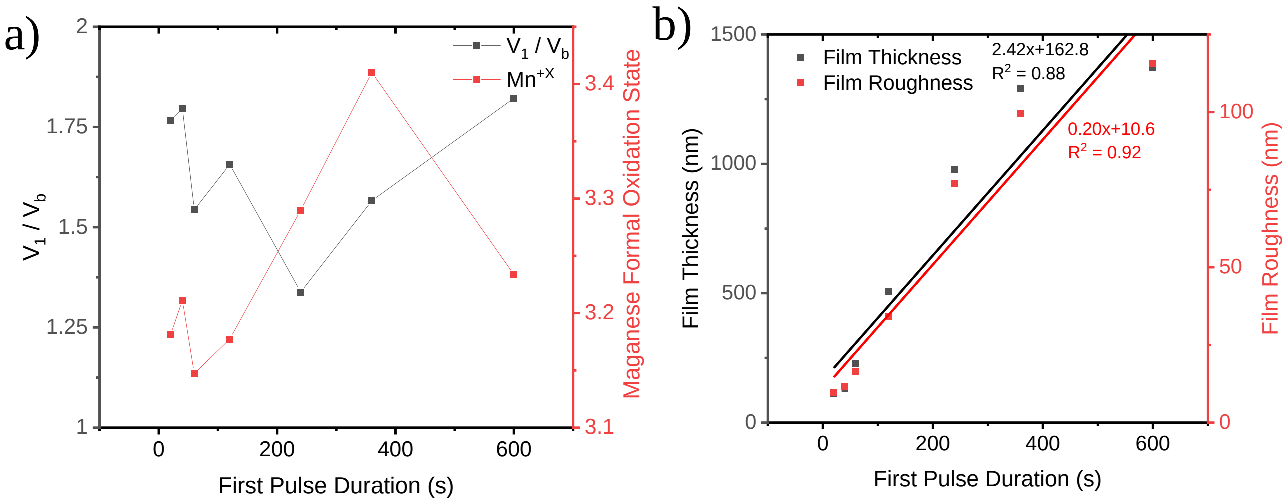

Figure 3-7: (a) Graph of the variation in the ratio between the Basal plane Raman peak at 575 cm^{-1} (V_1) and the potential defect peak at 610 cm^{-1} (V_b) and the variation in manganese formal valence from the Mn 3s peak splitting with first pulse duration, with a second and third pulse of 20 s and 0 s respectively. (b) Thickness and surface roughness information extracted from AFM images for varying first pulse duration. From this data, we observed that first pulse duration does not have a consistent effect on film quality, but decreasing first pulse duration leads to decreased film thickness. This thickness reaches 100 nm before saturating, with a duration of 20s.

To reduce the film thickness further, the solution molarity was decreased. Reducing the solution molarity decreased the Raman ratio and formal valence until the film began to break up into islands at concentrations below 20 mM, which led us to select 20 mM as the optimal solution molarity for high-quality films (Figure 3-8.a). Similar to the first pulse duration, the film thickness is highly correlated (R^2=0.96) with solution molarity, reducing from 100nm to 50nm with a reduction from 100mM to 20mM (Figure 3-8.b). In addition, as can be seen by the surface roughness, the films degrade significantly at concentrations below 20mM.

After these optimizations, the third pulse was reintroduced to improve film quality, and then the total duration of growth was varied, maintaining a pulse duration ratio of 1:1:0.5 in an attempt to reduce film thickness. The addition of the third pulse increased film thickness and manganese formal valence. Upon reducing the total duration, the V_1/ V_b ratio and formal valence increased, indicating improved material quality until 1.25s growth, after which the increases began to saturate (Figure 3-8.c). The thickness and surface roughness followed a similar trend to the solution molarity, with the reduced duration being highly correlated with thickness and roughness reduction, with the final film saturating at a thickness of 50nm, approximately 26 layers of δ-MnO_2, and roughness of ~2.5nm.

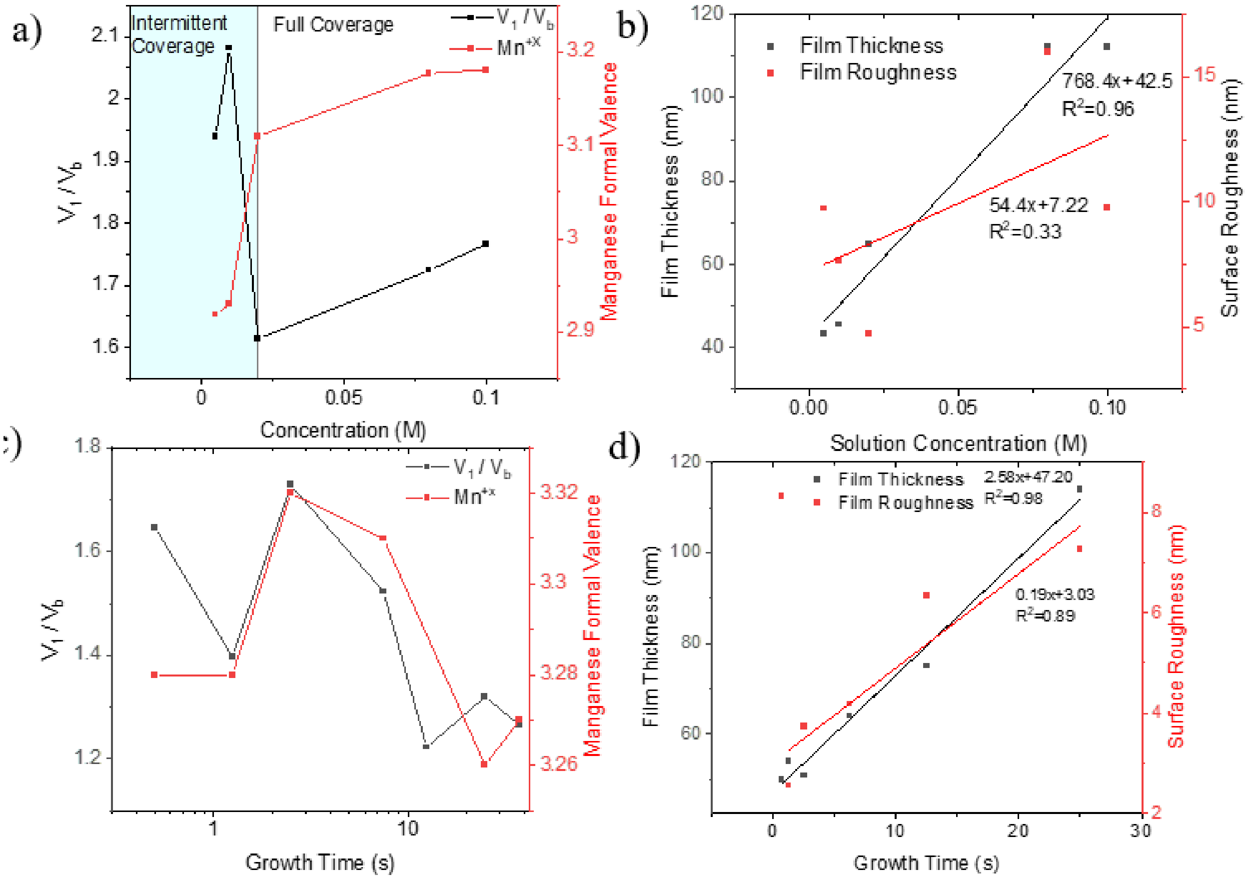

Figure 3-8: (a),(c) Graph of the variation in the ratio between the Basal plane Raman peak at 575 cm^{-1} (V_1) and the potential defect peak at 610 cm^{-1} (V_b) and the variation in manganese formal valence from the Mn 3s peak splitting with solution molarity (a), and total growth time (c). (b)(d) Thickness and surface roughness information extracted from AFM images vs solution molarity (b), and total growth time (d). From this information, we can see that reducing concentration leads to a minor reduction of film quality until the dissolution of the film below 20 mM but decreasing first pule duration leads to decreased film thickness. This caused us to conclude that 20 mM is the optimal concentration for growth. With a reduction in growth time, we see a general increase in material quality, that saturates at 1.25s, which we selected to be the optimal growth time

Based on these results, growth with pulse durations of 500 ms, 500 ms, and 250 ms and solution molarity of 20mM resulted in the highest quality films, with δ-MnO_2 films ~55nm thick and 3.33 formal valence, indicating the formation of a very thin film of δ-MnO_2 with high defect density and no stabilizing cations.

Section 3.7 Investigation of the MnO_2 EG/SiC Growth Dynamics

As the thickness of the films was reduced below 50nm, the film degraded, initially gaining a significant number of pinholes and then disparate islands. While this limited the final growth thickness, it allowed us to observe parts of the growth mechanism by reducing the solution molarity. As a result, from our optimal growth process, we reduced solution molarity and observed the surface via AFM and SEM. As the solution molarity was reduced to 5mM, significant pinhole defects formed in the film, most dense on the SiC terraces and least dense on the step edges of the material (Figure 3-9.a). As the molarity was reduced further to 2.5mM, a film was no longer formed, but a large number of 50 nm islands, which were densest on the SiC step edges, of MnO_2 were deposited on the surface. This indicated that the primary growth mode of the film was the deposition of 50 nm islands that then grew outwards and merged to form the film (Figure 3-9.b). This is consistent with the previous SEM images showing clear nanoparticles on the film's surface. SEM images confirmed this growth mechanism and corroborated that island nucleation was favored along the step edges. The growth was nearly a contiguous film on the step edges and growing into the terraces (Figure 3-9.c). This indicated that the presence of dangling bonds enhances the electrochemical deposition, as the favorable nucleation sites are the step edges, which have a higher incidence of dangling bonds than the terraces.[12].

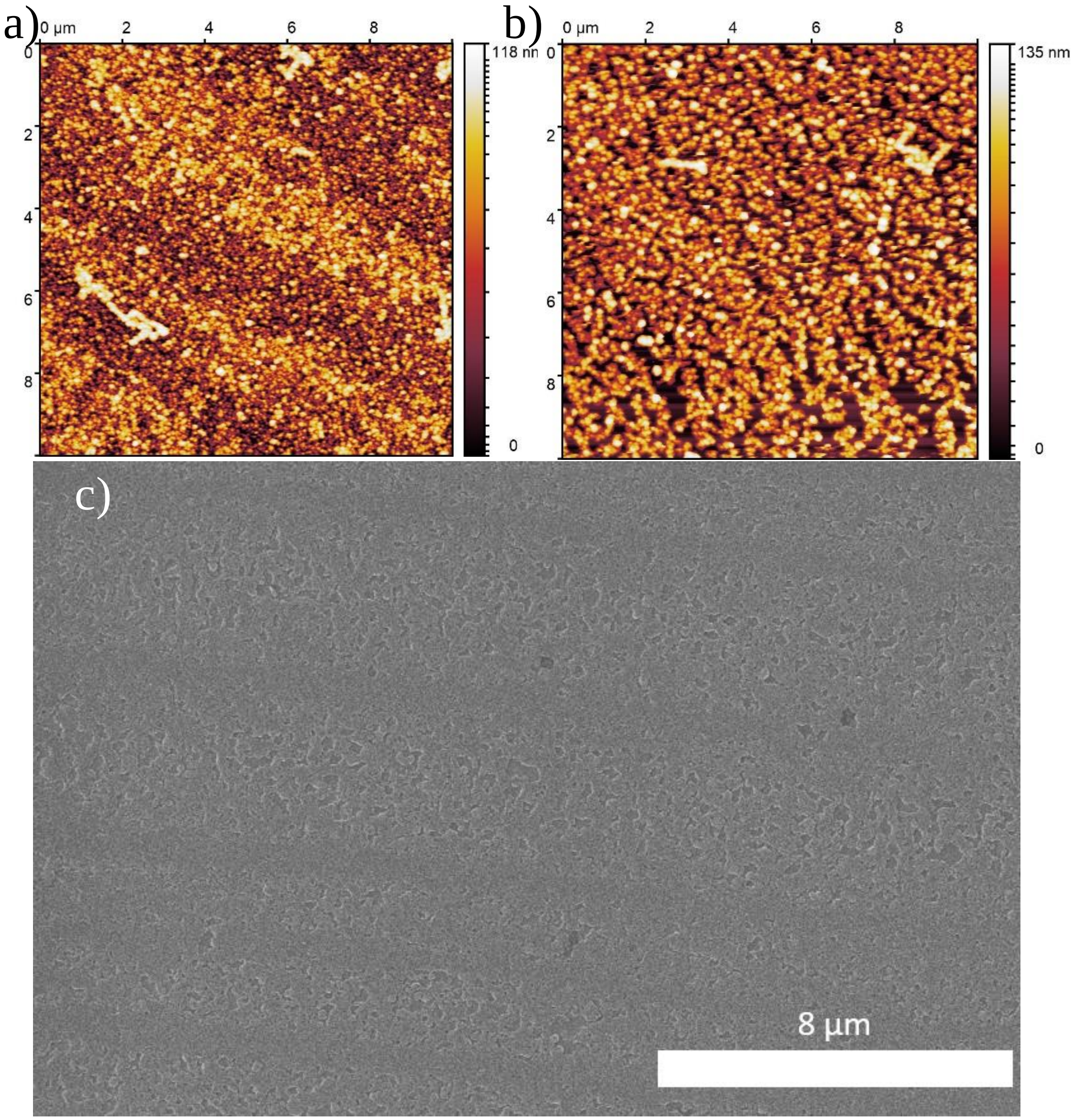

Figure 3-9. AFM +Height images of deposition with (a) 5mM (c) 2.5mM MnAc and (c) SE3M image of deposition with 5mM MnAc. It can be seen that as the solution molarity is reduced to 2.5mM, the film becomes individual islands with a thickness of ~50nm. At 5mM, a film can still be seen, but it is dominated by pinhole defects. This is confirmed in the SEM, as is the favored nucleation site of the graphene step edges

Additionally, the nanofibrous surface of the δ-MnO$_2$ surface, as was observed in the SEM, raises questions about whether the formed material is layered as expected or similar to other nanoflowers and nano-urchin structures reported in the literature in other materials. To probe this XPS can be utilized as it is surface sensitive and can determine the manganese formal valence via the Mn 3s, as well as provide insight into oxygen bond terminations and defects via the O1s region of the spectra. This can then be combined with angle-resolved methods to observe variations in defects between the bulk and the surface by observing the variation in Mn 3s and O1s spectra at glancing and normal incidence to the surface. To examine this, we used an unoptimized thin film, but the similarity in morphology indicates the result should be similar to the optimized growth. At normal incidence, the Mn 3s peak splitting was found to be 5.15eV (Figure 3-10.a), yielding an Mn formal valence of 3.16 in bulk. When taken at glancing incidence, the Mn 3s peak splitting was found to be 5.26eV(Figure 3-10.c), yielding an Mn formal valence of 3.04 in the surface, indicating that the surface contains a significantly higher $Mn^{+2/+3}$ defect density than the bulk of the film. An analysis of the O1s spectra corroborates this. At both normal and glancing incidence, the O1s spectra contain three components: the Mn-O-Mn bond at 529.9eV, the Mn-O-H bond at 531.4eV, and the H-O-H bond at 532.8eV, which is consistent with water stabilized δ-MnO_2 [87]. However, the contribution of the three components varies significantly between glancing and normal incidence. At normal incidence, the Mn-O-H contributes 37.8% of the total O1s spectral area, while at glancing incidence, it contributes 46.1% of the O1s spectral area. This indicates that the surface contains a significantly higher number of $Mn^{+2/+3}$ defects, consistent with the Mn 3s analysis and that many of these defects are terminated in hydroxyl groups (Figure 3-10. b,d). Due to the material surface's highly defected and hydroxylated nature, we would expect the surface reactivity to be enhanced, which is desirable for most manganese applications.

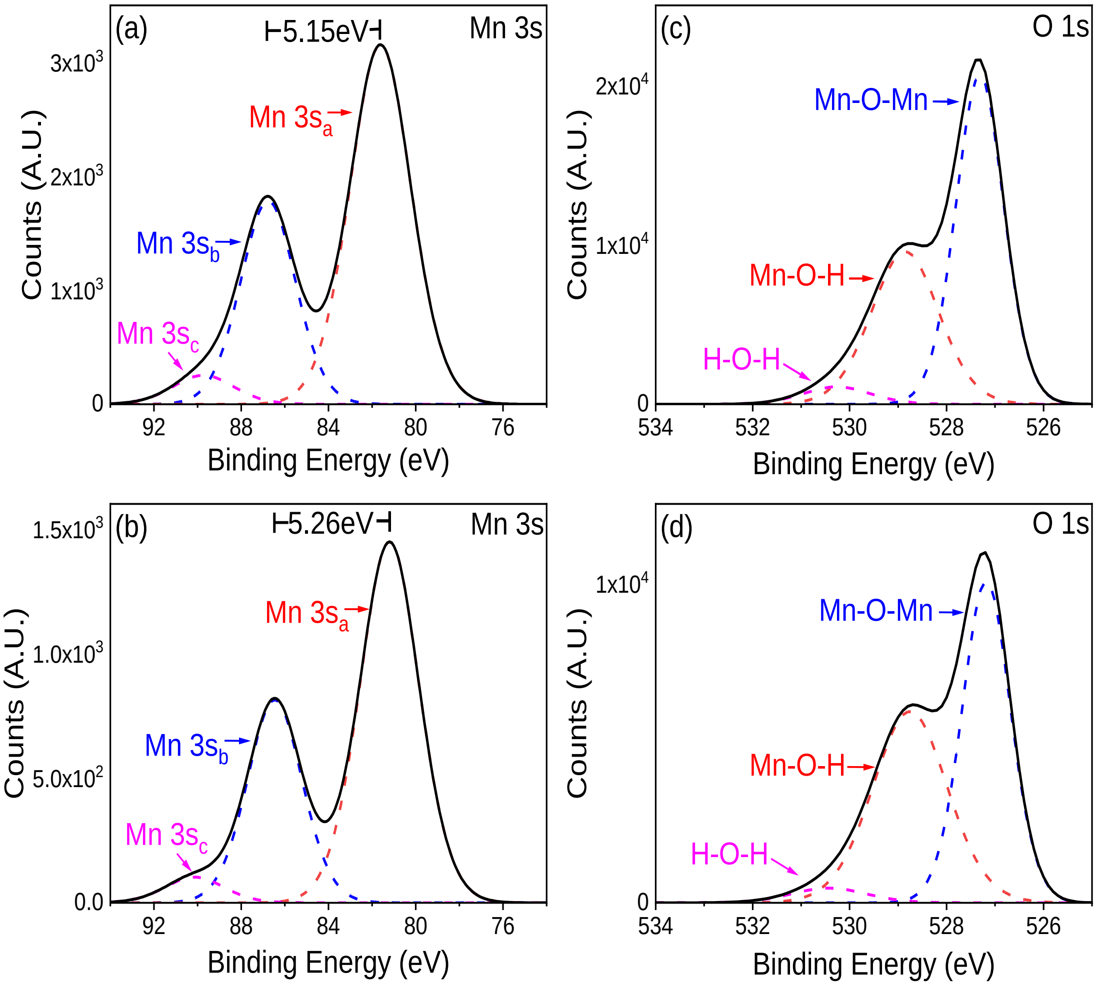

Figure 3-10. Angle-Resolved XPS of δ-MnO_2 of the (a,b) Mn 3s and (c,d) O1s at (a,c) 0° and (b,d) 70° from normal incidence. The increase in Mn 3s peak splitting and Mn-O-H contribution to the O1s spectra at higher angles indicates that the surface has a higher defect density and a larger number of hydroxylated Mn^{+3} sites.

The nanofibrous surface also brings into question whether the growth was epitaxially planar or more randomly oriented, similar to a nanoflower-like structure. To investigate this, we conducted mechanical exfoliation of the optimized film onto SiO_2 substrates, as epitaxial layered materials can be readily thinned by transfer with a simple adhesive (i.e., scotch tape) [50]. Transfer of optimized films led to a mixture of blue-white flakes and blue transparent flakes. AFM analysis of these exfoliated films revealed that the transparent exfoliated flakes had a surface roughness of less than 1nm (Figure 3-11.a), and the thinnest observed flake was ~5nm after (Figure 3-11.b), while the phase image indicated that these flakes were generally uniform

(Figure 3-11.c). This indicates that the δ-MnO_2 growth was epitaxial and planar, as this exfoliation behavior is similar to other epitaxial layered materials such as transition metal dichalcogenides[50]. This is in agreement with the XPS data, which indicates that despite the nanofibrous surface, the growth is generally planar and epitaxial.

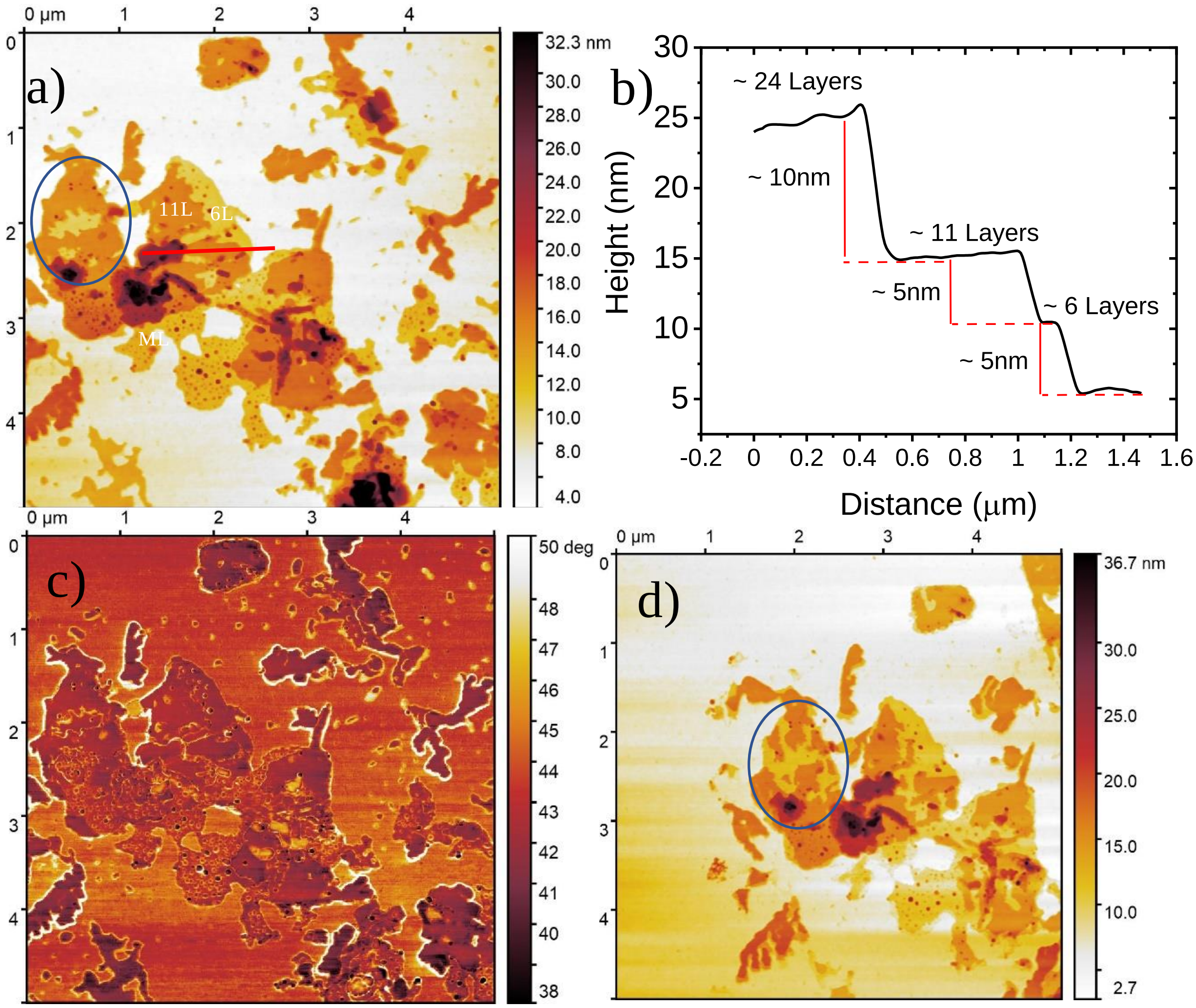

Figure 3-11. AFM (a,d) height and (c) phase images of mechanically exfoliated δ-MnO_2 on SiO_2. The height images indicate that a large number of unordered flakes were transferred from the EG/SiC substrate. These flakes are shown to have layer thicknesses spanning from approximately 6 layers to over 30 layers at the thickest point, which can be seen from the extracted profile (b). The general flatness of these flakes confirms their epitaxially layered nature. The phase image shows three distinct phases. A high phase is associated with adhesive residue from the transfer, the substrate phase, and the phase of the transferred material. That the transferred material has a distinct and consistent phase from the adhesive indicates we are seeing transferred δ-MnO_2. The presence of particulates on the surface of the flakes does raise

concerns, however, continued scans of the same region indicate that the flake layers are very fragile and damaged by the AFM process, as demonstrated by the reduction in size of the 11

Section 3.8 Gas Sensing Performance of Manganese Dioxide/EG/SiC Heterostructures

One of the key applications of transition metal oxides is gas sensing, which is often hampered by the high required operating temperature of transition metal oxide sensors, as we have discussed previously[9]. Using graphene to enhance the conductivity is one of the pathways to improving the accessibility and functionality of these sensors. One of the aims of the project is to use these as grown transition metal oxide graphene heterostructures to produce gas sensors. In addition, Manganese dioxide has the advantage of tunable interlayer spacing, which we can utilize to screen the kinetic diameter of incoming molecules to selectively sense different gases[108].

To test the viability of this heterostructure as a gas sensor, we first fabricated a simple 4-contact design on the as-grown δ-MnO_2 on EG on n^+ 6H-SiC using Ti/Au (30/120nmm) electrodes deposited by e-beam evaporation (Figure 3-12). This gas sensor was then tested in an atmosphere with an RH of 55.2% at room temperature by applying a constant 100 mV potential across the contacts while measuring output current to determine the gas response. The sensor was tested under 5 ppm NO_2, 5 ppm NH_3, 35 ppm IPA, and 85 ppm CH_3OH flown separately. NO_2 and NH_3 were selected as MnO_2 has previously displayed responsivity to nitrogen-based gases [94, 96].IPA and CH_3OH were selected to determine the selectivity of the sensor against volatile organic compounds (VOCs), as well as the effect of the graphene

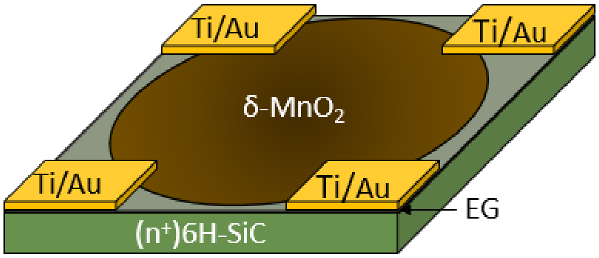

Figure 3-12: . Schematic of the gas sensor fabricated from the δ-MnO2/EG/SiC heterostructure.

surface on gas responsivity [76]. The response of the gas sensor was evaluated using Equation 3.1.

$$\frac{I_{On} - I_{Off}}{I_{Off}} \tag{3.1}$$

Where I_{On} is the current under gas exposure, and I_{Off} is the resting current. We also determined the response/recovery time was measured using 90% of the average “ON” current and 10% of the average “ON” current as thresholds, respectively. The gas sensor displayed no response when exposed to either IPA or CH_3OH. This is unlike the high resistance changes observed in graphene-based sensors [16], which indicates that graphene does not act as the sensing element in the heterostructure, and has improved selectivity over bare graphene[76].

However, when the sensor was exposed to 5ppm NO_2 and 5ppm NH_3 the gas sensor displayed a positive responsivity of 0.26% and 0.22% respectively with a response recovery time of 3.1s/1.5s to NH_3 and 2.3s/6.6s to NO_2 (Figure 3-13). While this magnitude of response is quite small, the SNR of the response is greater than 15 dB for both gasses, allowing it to be easily differentiated from the noise in the sensor. Significant concerns are both the positive response to both gases and a sizable drift during testing, which may indicate that the large response SNR is due to the relative humidity of the testing gasses as opposed to a selective response to the gas. Moving forward with the project, we aim

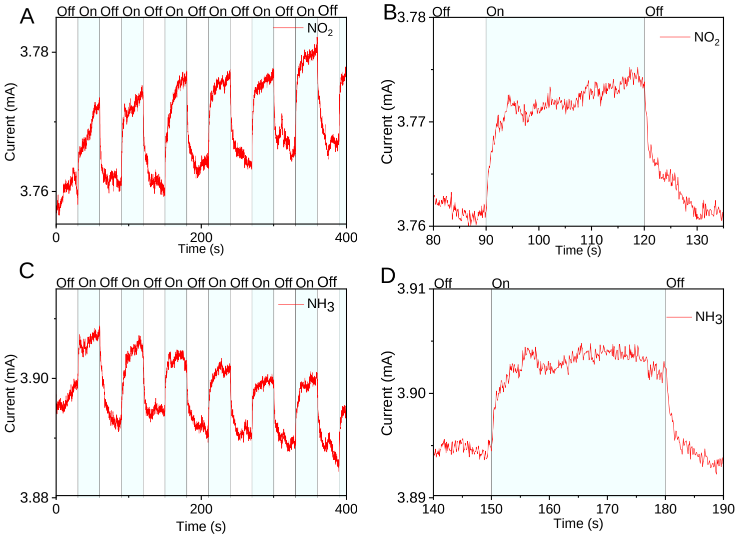

Figure 3-13: . Sensor Response to A, B. 5ppm NO_2, C, D. 5ppm NH_3. The sensors exhibit a fast response to both gasses, however, the NH_3 response appears much more stable than the NO_2 response. Additionally, both sensors exhibit minor instability over the 6 cycles displayed here.

to determine if this is the case and the effect that patterning and intercalation have on this gas response.

A key component of this gas response is the formation of a junction between the epitaxial graphene and the δ-MnO_2, due to a work function mismatch between the two materials. To evaluate this, we utilized Kelvin force probe microscopy (KPFM) on the heterostructure, which determines the work function of the materials via a capacitive effect [120]. The KPFM indicated that the manganese dioxide exhibited a p-type doping effect on the QEG, driving its work function from 4.8eV [64] to 4.95 eV (Figure 3-14. a-b). It also indicated that a 300 meV potential barrier was formed between the MnO_2 and the QEG, with the MnO_2 work function being 5.25eV. The small size of this potential barrier allows for high-speed charge transfer between the graphene and the MnO_2 and, therefore, improves reaction kinetics in the resulting heterostructure [42]. As charge transfer drives most MnO_x applications, we believe this is desirable for future device applications. It is important to note that this experiment was done on semi-insulating 6H-SiC as opposed to N^+ 6H-SiC and QEG as opposed to EG. Therefore, to draw more conclusions about the previous gas sensing results, we need to run additional experiments on EG-n^+ 6H-SiC to determine that potential barrier, which should be much greater than what is seen here. This set of further experiments will be discussed in greater detail in Chapter 8 in future work.

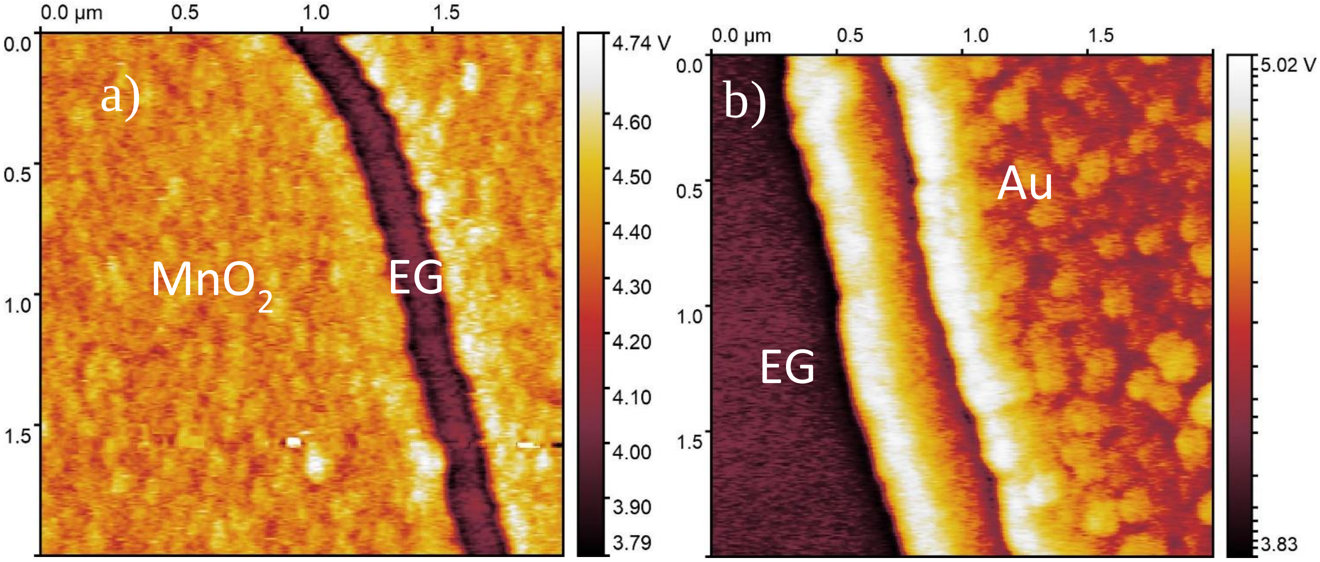

Figure 3-14: Kelvin probe force microscopy images of the (a) MnO$_2$/EG junction and the (b) EG/Au junction. In (b) there is a visible 150 meV barrier between the EG and the Au (Φ=5.1eV) and in (a) there is a 300 meV barrier between MnO$_2$ and EG. This indicates p-type doping from the MnO$_2$ as the EG has a modified work function of 4.95eV and the MnO$_2$ has a work function of 5.25eV

Chapter 4: Heat-Driven Decomposition of Manganese Dioxide on Pristine EG/SiC

Manganese Dioxide is the most widely studied of the Manganese oxide compounds due to its significant tunability in both crystallographic structure and reactivity, but alternate forms of manganese oxide remain of interest due to their variable magnetic properties as they approach the nanometer limit[105, 121].

α-Mn_2O_3 has well-known antiferromagnetic properties when produced as a nanostructured material, with a Neél temperature of approximately 80K [121]. $Mn_3O_{4,}$ by contrast exhibits ferromagnetic properties when produced as a nanostructured material with a Curie temperature of approximately 40K[105]. While these temperatures are low, with the ferromagnetic transition of Mn_3O_4 occurring below liquid nitrogen temperatures, they provided the basis for additional study. In addition, the effect of heterostructures of these materials with pristine graphene on their magnetic properties is to our knowledge completely unexplored, due to the oxidizing nature of the growth of manganese oxide compounds as discussed in chapter 5. We therefore aimed to use our existing films of δ-MnO_2 and decompose them into lower oxidation state compounds via annealing, to examine the effect of the EG-MnO_z on their magnetic properties.

The literature indicates that δ-MnO_2 will readily reduce to a lower oxidation state of manganese oxide under mild annealing conditions (~500°C) [122]. This transformation is also tunable by varying the oxygen content of the annealing environment, with low oxygen content increasing the reducing effect of the annealing process[122]. As the oxygen intercalation temperature of QEG on SiC is ~ 600°C in air [123], the transformation of as-deposited δ-MnO_2 to Mn_2O_3 and Mn_3O_4 can be achieved without deintercalation of the underlying epitaxial graphene surface or replacing hydrogen intercalations with oxygen. To confirm this transformation with our films, we annealed the as-deposited δ-MnO_2 in air for two hours, under temperatures from 50°C-

500°C, to observe the transformation to Mn_2O_3. We then annealed as-deposited δ-MnO_2 in Ar for two hours at 500°C to observe the transformation of the film to Mn_3O_4.

Section 4.1 Crystallographic Characterization of the Heat based Decomposition of Manganese Dioxide on EG/SiC

We then utilized Raman spectroscopy to observe the transformation of the material from δ-MnO_2 to Mn_2O_3 and Mn_3O_4, as the Raman spectra of each MnO_x compound are very distinct [116, 120]. Raman also allows us to determine the integrity of the underlying QEG, as its Raman spectra are strongly related to its structural order and material quality [54]. This makes Raman a powerful tool for analyzing these annealing processes.

During the initial anneals in air, significant changes in the Raman spectra were observed. For annealing temperatures under 100 °C, the characteristic δ-MnO_2 was maintained with limited changes in the V_1/V_b ratio. However, as the temperature was increased beyond this to 200°C, the Raman spectrum of the films degrades into a combination of various MnO_x compounds (Figure 4-1.a). This is seen by the enhancement of the peak at 611 cm^{-1} and its shift to 630, which is consistent with the formation of γ-Mn_2O_3, a heating-based decomposition product in the Raman spectrum [116]. As the temperature is further increased from 200°C to 400°C, the film changes significantly, with the Raman spectrum reforming sharp peaks, indicating the partial recrystallization of the film (Figure 4-1.b). After the annealing temperature is increased further to 500°C, the film recrystallizes completely, containing only sharp peaks, indicating the formation of a lower oxidation state manganese product. In this Raman spectrum between 100-750 cm^{-1}, we observed 4 strong bands, located at 200 cm^{-1}, 319 cm^{-1}, 650 cm^{-1}, and 705c m^{-1}. This is consistent with the formation of bixbyite or α-Mn_2O_3 in the film [124] (Figure 4-2.a). The lack of broad weak bands in these regions indicates that the amorphous MnO_x compounds have been fully transformed to α-Mn_2O_3 producing a high-quality film. At 500°C, the region between 1200-3000 cm^{-1} was analyzed to determine if the transformation from MnO_2 to Mn_2O_3 had damaged the graphene. In this region, a low-intensity D-peak was observed, with a D/G ratio of 0.07, indicating that the annealing process had generated a small amount of damage to the structure. However, the 2D peak maintained a FWHM of ~67 cm^{-1}, indicating the bilayer character of the film and, therefore, its hydrogen-intercalated quasi-freestanding nature maintained during the annealing process [54].

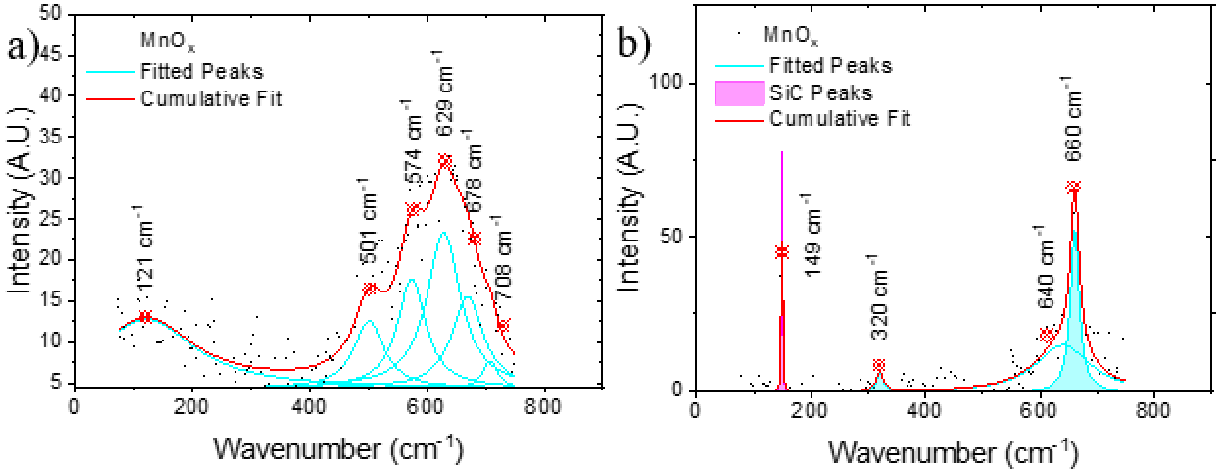

Figure 4-1: Raman spectra of δ-MnO_2 annealed in air at 200 °C (a) and 400 °C (b). It can be seen that the major peaks of δ-MnO_2 begin to degrade when annealed at 200 °C, with their intensities relative to the anomalous peak at 629 cm^{-1} being significantly reduced. This causes the spectrum to appear very broad, indicating the breakdown of the structure. After annealing to 400 °C we can see the return of sharp peaks at 660 cm^{-1} and 320 cm^{-1}, indicating some recrystallization, however, the broad peak at 640 cm^{-1} has a significant amount of remaining amorphous material

Following a 2-hour anneal in Ar at 500°C, significant changes in the Raman spectra were also observed, indicating a transformation of the δ-MnO_2 into Mn_3O_4. This was evidenced by the appearance of strong Raman bands at 660 cm^{-1}, 374 cm^{-1}, and 320 cm^{-1}, consistent with Mn_3O_4, and the removal of all other peaks from the spectra [116] (Figure 5-12.b) Additional analysis of the graphene, in the region from 1200 to 3000 cm^{-1}, indicated its quality was maintained as no D-peak was observed and the FWHM of the 2D peak was 60cm^{-1}[54]. This confirms that the process did not damage the underlying graphene substrate and demonstrates the growth of thin films of δ-MnO_2, α-Mn_2O_3, and Mn_3O_4 on EG/SiC without damaging the underlying graphene substrate.

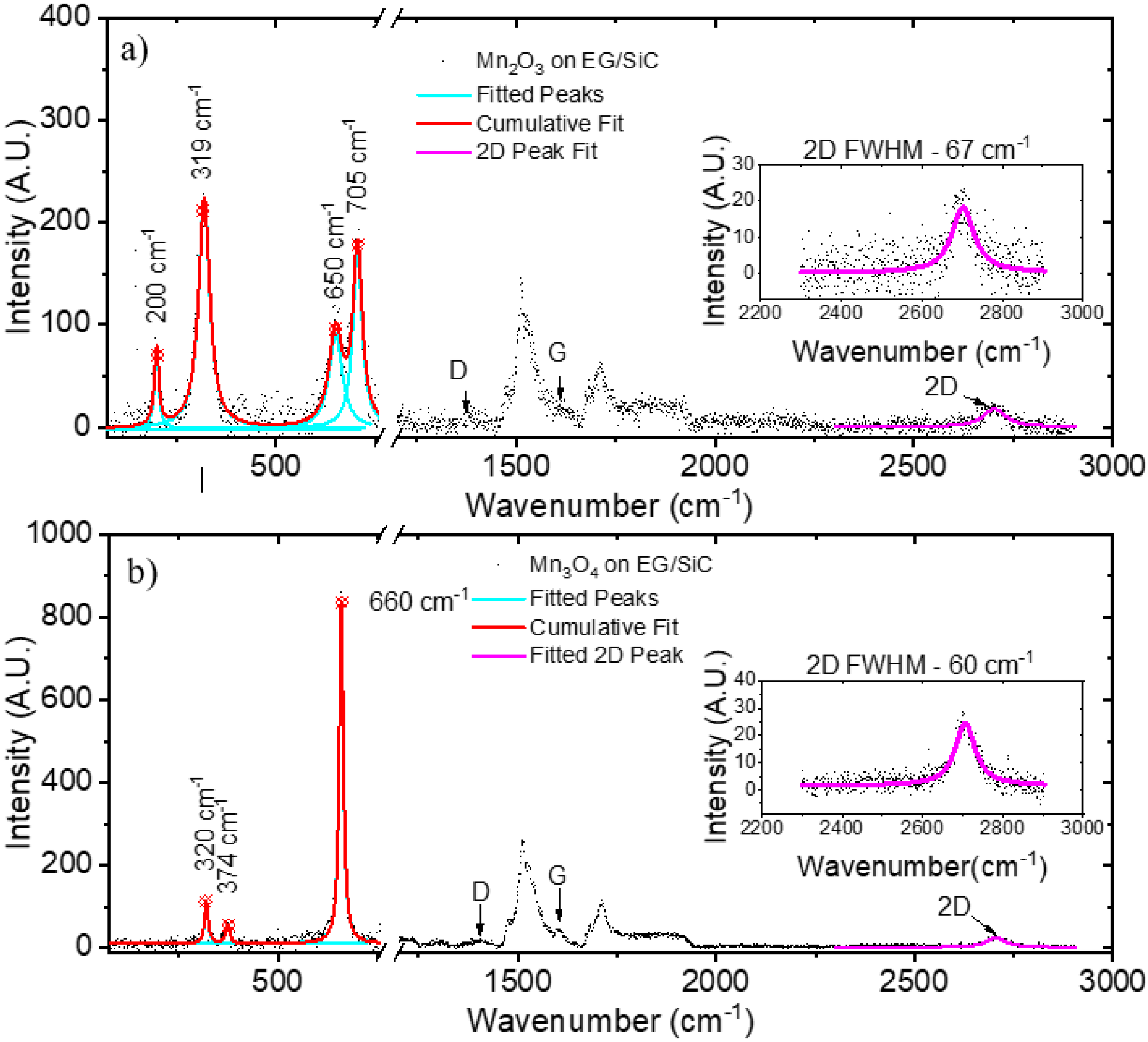

Figure 4-2. Raman Spectra (a) Mn_2O_3, (b)Mn_3O_4 on QEG. After annealing, in air (a) the appearance of peaks at 200 cm^{-1}, 319 cm^{-1}, 650 cm^{-1}, and 705^{-1}cm indicates the formation of α-Mn_2O_3. After annealing in Ar (b) the appearance of peaks at 660 cm^{-1}, 374 cm^{-1}, and 320 cm^{-1} indicates the formation of spinel Mn_3O_4. Upon examination of the high wavenumber region of all three spectra, the lack of a D peak forming between 1250 cm^{-1} and 1400 cm^{-1} indicates that the process did not defect the underlying graphene. Additionally, the maintenance of the 2D FWHM at ~60cm^{-1} indicates the bilayer character of the QEG is maintained through the growth process.

Section 4.2: Changes in Surface Morphology during decomposition of MnO_2 on EG/SiC

The surface morphology of the film changed with annealing in air. As the surface was annealed at low temperature (50°C-100°C), nanoplates replaced the nanofibers originally observed on the surface (Figure 4-3.a). These platelets were generally perpendicular to the surface, and we believe that they are a result of the nanofibers merging as the surface is annealed. As the temperature increases beyond 100°C, the nanoplatelets change with their size increasing and their angle relative to the surface becoming shallower (Figure 4-3.b). This trend continues with increasing temperature (Figure 4-3.c).

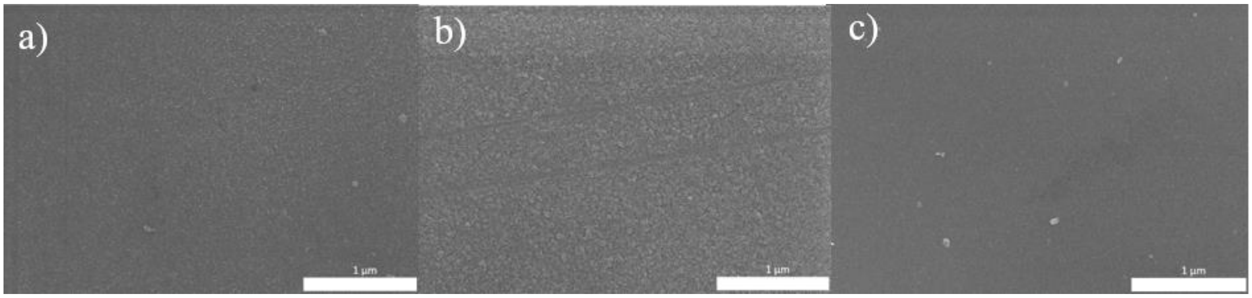

Figure 4-3: SEM images at 30kx magnification of δ-MnO_2 after annealing for 2 hours in air at (a) 100 °C, (b) 200 °C, and (c) 400 °C. After annealing at 100 °C the nanofibers previously seen on the surface, congeal into nanoflakes, which are generally perpendicular to the surface. As the temperature is increased the angle of these flakes relative to the surface decreases, and they become more parallel. This is consistent with the morphology seen after full transformation to Mn_2O_3, where the surface is made up of parallel flakes with gaps in between.

When the temperature is increased to 500°C, a significant change in the surface morphology was observed, which accompanies the crystallization to Mn_2O_3. At this temperature, the surface becomes nanoporous, with pores approximately 10nm in diameter (Figure 4-4.a). We believe this is a continuation of the previous process, with the nanoplatelets merging to form a porous film. Significant morphology changes were also observed by SEM accompanying the transformation to Mn_3O_4. After the transformation, the surface became made up of nanocubes, connected by rough nanowalls, with cube sizes on the order of 100nm (Figure 4-4.b). AFM imaging of the heterostructures was also taken to confirm the change in surface morphology observed in the SEM images. These images indicated the transformation significantly increased the surface roughness, with values of 6.5nm and 18.9nm for $Mn_2O_3$and Mn_3O_4, respectively, which is consistent with the surface morphology changes observed in the SEM (Figure 4-4.c-d). An approximately 30% thickness reduction with the transformation from δ-MnO_2 to Mn_2O_3 was also observed. This observation is consistent with the transformation from the epitaxial layered δ-MnO_2 with a z-direction lattice constant of $c_{\delta-MnO_2}$= 14.61 Å to α-Mn_2O_3 with a z-direction lattice constant $a_{Mn_2O_3}$=9.41Å predicting a 35% thickness reduction if the δ-MnO_2 is epitaxial and layered [116]. This thickness reduction was also observed after transformation to Mn_3O_4, which is similarly consistent with the expected reduction in the z-direction lattice constant from $c_{\delta-MnO_2}$= 14.61 Å to $a_{Mn_3O_4} = 9.81$ predicting a thickness reduction of 33%. This further corroborates our previous conclusion that despite the nanofibrous surface of the film, it is generally epitaxial and planar, which is what we had desired.

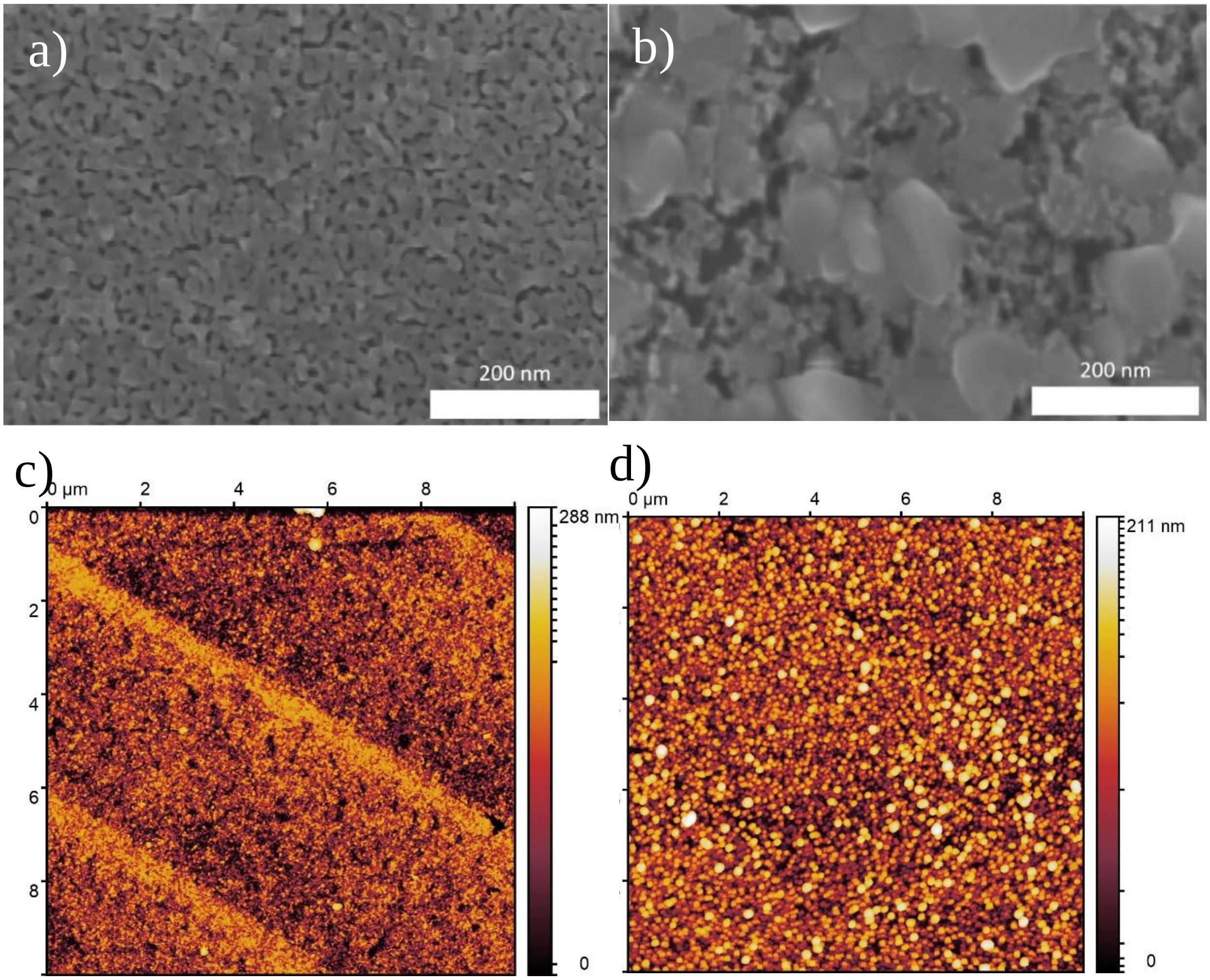

Figure 4-4: SEM(a-b) taken at 80Kx magnification and AFM (c-d) images of (a,c) Mn_2O_3, and (b,d)Mn_3O_4. The initial nanofibrous appearance of the δ-MnO_2 (Figure 4-2) is transformed to a nonporous structure (b) after annealing in air, which is confirmed by the increased surface roughness in the AFM (c). After annealing in argon the δ-MnO_2 is transformed into large nanocubes connected by nanowalls (b), which is an unexpected morphology. In addition, the AFM for Mn_3O_4 no longer has a clear image of the SiC step edges, which could be due to significant increases in the surface roughness

Chapter 5: Transformation of Water-Stabilized Manganese Birnessite to Alkali Metal Birnessite via Intercalation

Water-stabilized birnessite has significant interest due to its inherently green synthesis [125] and lack of interlayer chemical contaminants. However, a large number of applications for manganese dioxide birnessite, including catalysis [101] and energy storage [102-104] depend on the intercalation of different ions into the interlayer of the birnessite crystal. Additionally, the interlayer spacing of the material is highly tunable with interlayer cation size and electropositivity [102, 108], which can significantly affect the chemical interactions of the structure.

The ability to alter the interlayer spacing with intercalation also allows for the control of the transit of gas molecules into the interlayer structure via the kinetic diameter of the molecule in question. This would potentially allow for the tunning of the δ-MnO_2 structure to detect gases from the environment. This was a key phenomenon I hoped to explore via this intercalation testing. To take advantage of this, it is necessary to determine if the intercalation of various ions into the structure is possible and the efficiency of this process. To evaluate this, I attempted to intercalate alkali metal cations into the structure, as they are commonly presented in the literature [115].

Section 5.1 Transformation of Water-Stabilized Manganese Birnessite to Alkali Metal Birnessite via Single Pulse Intercalation

Of the alkali metal ions available, we elected to use sodium in the form of a 1M sodium chloride salt solution, as Na-MnO_2 has a highly distinct Raman spectrum from H-MnO_2, unlike K-MnO_2 which is more commonly seen in the literature[115], and the high conductivity of NaCl was seen as conducive to successful intercalation[126]. To perform the intercalation, we initially elected to do a constant voltage pulse at the reduction potential of the NaCl-MnO_2-EG system, which was determined by cyclic voltammetry in a three-electrode cell with similar electrodes to those described in section 3.1, to be -0.14 V (Figure 5-1) on our optimally grown δ-MnO_2-QEG heterostructures, with a nominal initial thickness of 50 nm.

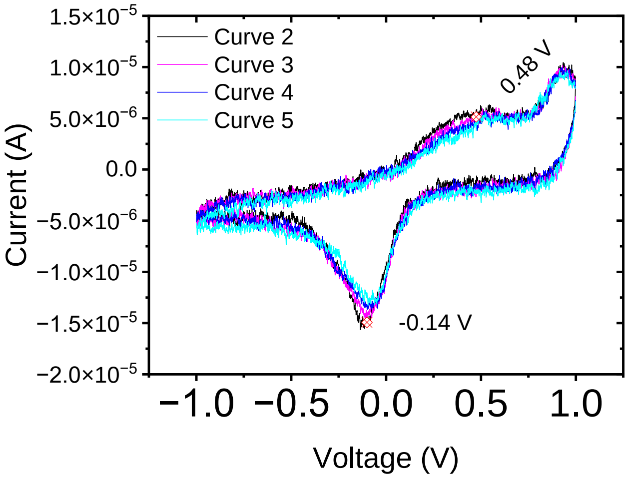

Figure 5-1: Cyclic voltammetry of 1M NaCl solution with a Ag/AgCl reference electrode, a MnO_2/EG working electrode and a Pt counter electrode. It can clearly be seen that there is a strong reduction potential at -0.14V, indicative of Na intercalation into the structure

After intercalation, we conducted a combination of Raman spectroscopy and optical microscopy of the sample to determine the efficacy and efficiency of the intercalation process. The initial sample had large microplatelets, hundreds of microns long, with cracks perpendicular to the step edges (Figure 5-2.a). After intercalation, the sample had a spiderweb pattern, with thin multicolored strands between large dark blue regions and no remaining cracks (Figure 5-2.b). Analysis of the Raman spectra of these regions indicated that the multicolored regions were Na-MnO_2, as indicated by the blue shift of the peak at 575 cm^{-1} to 580cm^{-1} and the redshift of the 650cm^{-1} peak to 633cm^{-1}[108, 115]. In addition, the intensity of the 633cm^{-1} peak in these regions was significantly suppressed compared to the 580cm^{-1} peak, which is associated with damping of the MnO_6 octahedral stretching mode due to interactions with the charged interlayer ions[108, 115], confirming the intercalation of Na^+(Figure 5-2.c). However, the large blue regions were shown to be H-MnO_2, of a reduced crystalline order due to the reduction of the 575cm^{-1} and 650cm^{-1} peak intensities compared to the defect peak at 610cm^{-1}(Figure 5-2.d). This analysis of the optical images indicates that the intercalation efficiency of this method is ~20%, which is too low for many applications.

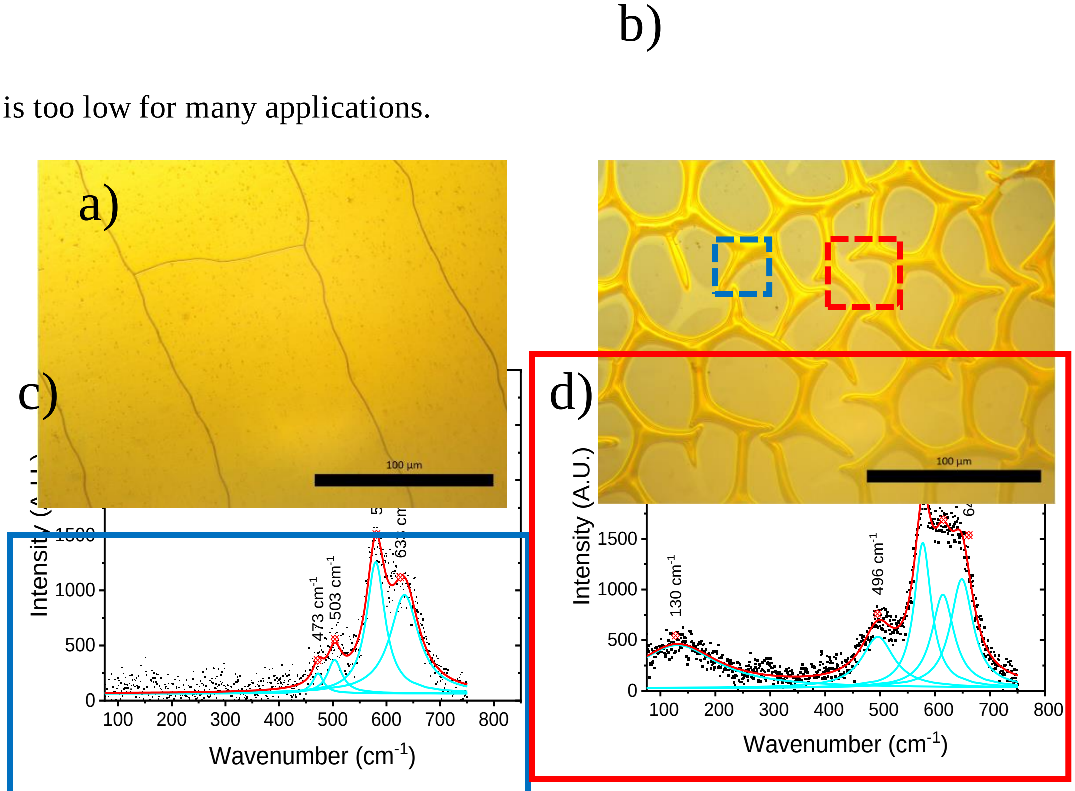

Figure 5-2: (a,b) Optical images (a) before and (b) after intercalation with NaCl. (c,d) Raman spectra of the (c) multicolored and (d) blue regions of the intercalated MnO_2 structure. The shifts of the 650cm^{-1} and 575cm^{-1} peaks indicate that part of the material has intercalated, but the low amount of multicolored regions indicates that this efficiency is poor.

Section 5.2 Investigation of Ionic Transport in Water-Stabilized Manganese Birnessite via Cycled Potassium Loading

The poor efficiency of single-pulse intercalation caused us to conclude that intercalation via cycling would have higher efficiencies. However, the literature indicated that this method was dependent upon the structural and ionic transport properties of the birnessite[104, 115, 127], which are unknown for our QEG-MnO_2 heterostructure. To investigate these properties, we ran cyclic voltammetry using 2M KNO_3 at cycle rates of 100 mVs^{-1} to 5 mVs^{-1} with a potential window of -0.1 V to 1V for 1000 cycles. KNO_3 was selected as the intercalation salt, as K-type birnessite is more commonly presented in the literature, and K has seen more cycling experiments due to the growing interest in potassium ion batteries[104, 128, 129]. The potential window was selected such that no redox peaks were present to prevent irreversible side reactions, while the variation in cycle rate allowed us to use Dunn’s method [130] to extract the reactive and diffusive contributions to capacitance and better understand ionic transport in the system. Dunn’s method takes advantage of the relationship in Equation 5.1.

$$i = k_1 v + k_2 v^{\frac{1}{2}} \tag{5.1}$$

$$\frac{i}{v^{\frac{1}{2}}} = k_1 v^{\frac{1}{2}} + k_2 \tag{5.2}$$

Where *i* is the current, k_1 is the reactive contribution to capacitance, and k_2 is the diffusive contribution to capacitance [130].

Following this experiment, we observed an interesting phenomenon in the capacity of the films with respect to cycle number (Figure 5-3.b). At 100 $mVs^{-1,}$ we observed the expected capacity decay, an initial decrease in total capacity followed by a stabilization, which is commonly seen in battery [103] and supercapacitor cathodes [131]. However, as the sweep speed was decreased, a sharp reduction was seen initially, followed by a significant recovery of the capacitance. The sharpness of this capacity reduction appeared to be correlated with the sweep speed, with lower sweep speeds leading to sharper capacity reduction and recovery curves.

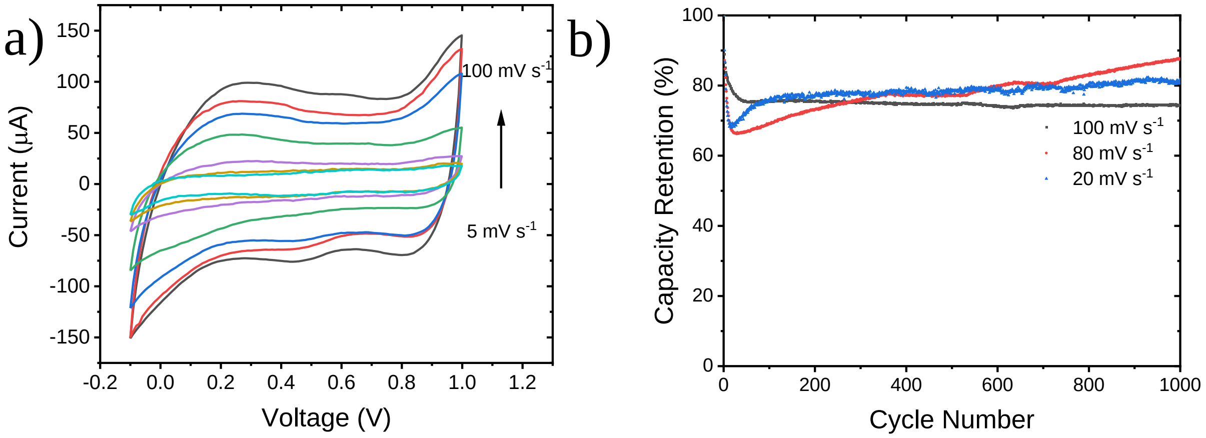

Figure 5-3: (a) Cyclic Voltammetry curves at sweep speeds of 100 mVs^{-1} to 5 mVs^{-1}. (b) Capacity retention of the 100 mVs^{-1}, 80 mVs^{-1}, 20 mVs^{-1} curves over 100 cycles. It can be seen in the capacity retention that lower scan speeds lead to a significantly sharper initial capacity reduction followed by a significant recovery.

We then conducted a Dunn analysis of the intercalation process at cycle 200, as this was far enough past the initial capacity reduction to describe the intercalation kinetics, as opposed to initial nonreversible reactions. To do this, Eq. 5.2 was used at each point of the CV curve from 0V to 0.9V to calculate the contributions to the current and then integrated over this region to find the total reactive and diffusive contributions to capacitance (Figure 5.4). We excluded the first and last 0.1 V of the curve as the Dunn model breaks down in these regions due to the sharpness of the curve, leading to non-physical results.

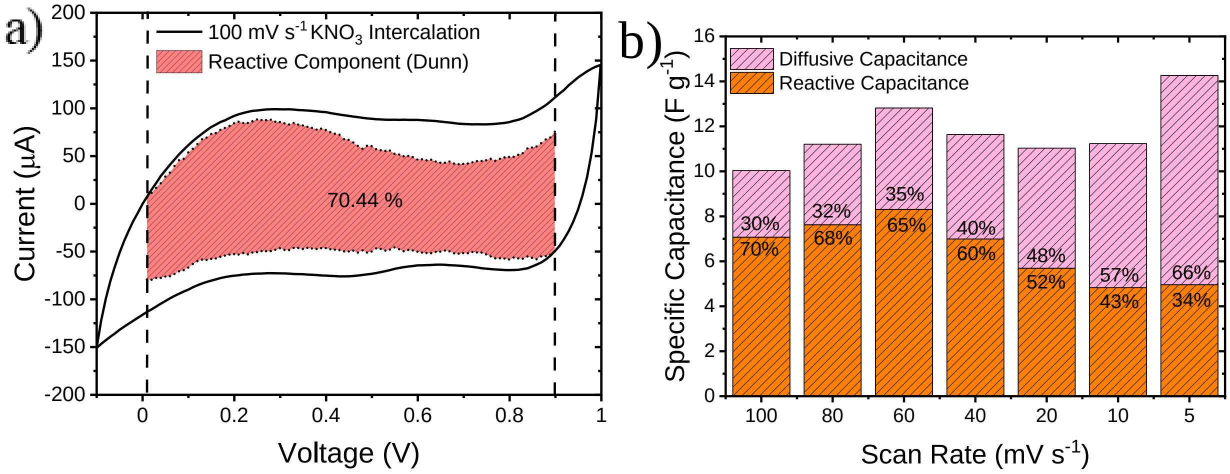

Figure 5-4: (a) Example Dunn Capacitance analysis of 100 mVs^{-1}(b) Calculated specific capacitance and contribution from diffusive and reactive capacitance elements by sweep speed. At sweep speeds below 40 mVs^{-1}, diffusive capacitance dominates, with the highest contribution at 5 mVs^{-1}

From this data, we concluded that to get the best intercalation results, we should conduct scans at 5 mVs^{-1} as this speed had the highest diffusive contribution at 66% of the specific capacitance. We also concluded that we should cycle 20 times to exhaust the initial reactions seen previously (Figure 5-3.b) and allow for improved intercalation of the films.

Section 5.3 Transformation of Water-Stabilized Manganese Birnessite to Sodium Birnessite via Cycled Intercalation

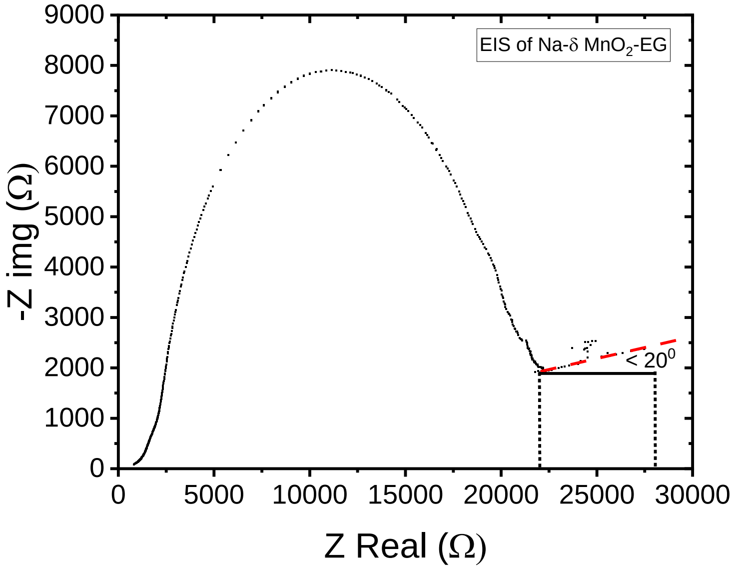

Figure 5-5: EIS of $NaNO_3$-MnO_2/EG-Pt System. Important to note here is the low angle of the diffusion resistance component of the EIS, indicating a strong rate limiting our intercalation process.

Following this, we changed intercalation salts to $NaNO_3$, as previously used in the literature, and has Na-type birnessite more readily identifiable Raman spectra than K-type birnessite. To further understand the intercalation process, I then conducted electrochemical impedance spectroscopy of the $NaNO_3$-MnO_2/EG-Pt system to better understand the dynamics of the intercalation. The resulting Nyquist plot had two distinct components (Figure 5-5): a semi-circular component related to solution resistance [132] and a shallow slope linear region. This linear region is associated with diffusion resistance in the electrode and is expected to have a 45° angle to the Z-Real axis[132]. Reductions of this angle indicate a significant diffusion rate limiting the reaction[132]. This suggested that the planar nature of the film and its high area coverage significantly reduced the intercalation efficiency of the film.

The sample was characterized after EIS, to provide initial indications of the cycling intercalation. The optical images revealed a similar spider web pattern to what was observed in the single pulse intercalation, with multicolored regions between dark blue or black regions. However, the multicolored regions are significantly larger after cycling, and portions of the film delaminated, which may have improved intercalation efficiency (Figure 5-6.a). Analysis of the Raman spectra indicates we have reversed the single pulse intercalation distribution, with the dark circular regions being intercalated, as indicated by the blue shift of the 575cm^{-1} peak and the redshift and suppression of the 650cm^{-1} peak (Figure 5 4.b). While the multi-colored region has become very poorly ordered, with some Na-intercalation as indicated by the higher noise loss of the lower wavenumber peaks in the Raman spectra (Figure 5-6.c). Additionally, optical analysis indicates that the efficiency improved to 35%, indicating cycling is a superior method of intercalation

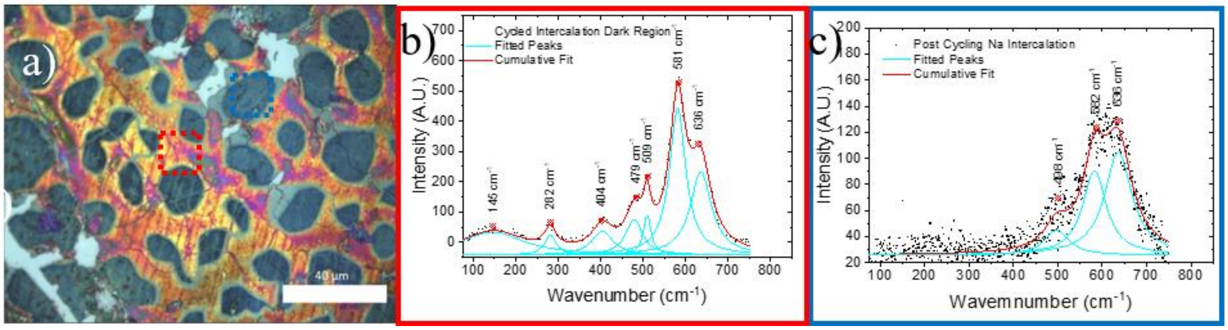

Figure 5-6: (a) Optical Image of MnO_2/QEG after EIS with $NaNO_3$.(b,c) Raman spectra of (b) dark circles, and (c) multicolored regions of the film. Important to note that in contrast to the previous intercalation method, the intercalated regions are the circular dark regions, and the non-intercalated regions are the multicolored regions, indicating that with cycling we get ions stuck in the structure, as opposed to being unable to penetrate.

With this information, we concluded that the optimal way to get efficient intercalation would be to introduce gaps into the film to allow for ions to more easily transit into the structure and reduce the rate-limiting of having ions transit through a primarily planar film with very small cracks. To do this, we took advantage of the fact that manganese dioxide does not deposit on bare silicon carbide to prepattern ribbons into the structure, and we used those gaps to improve the intercalation. The initial ribbons set was 100um wide, separated by 10um across the entire structure. This was then intercalated by cycling 1M $NaNO_3$ with cyclic voltammetry for 20 cycles at a low scan rate of 5 mV/s from -0.5 to 0.5 V, with the window selected to avoid irreversible redox reactions and the other parameters selected based on section 5.2.

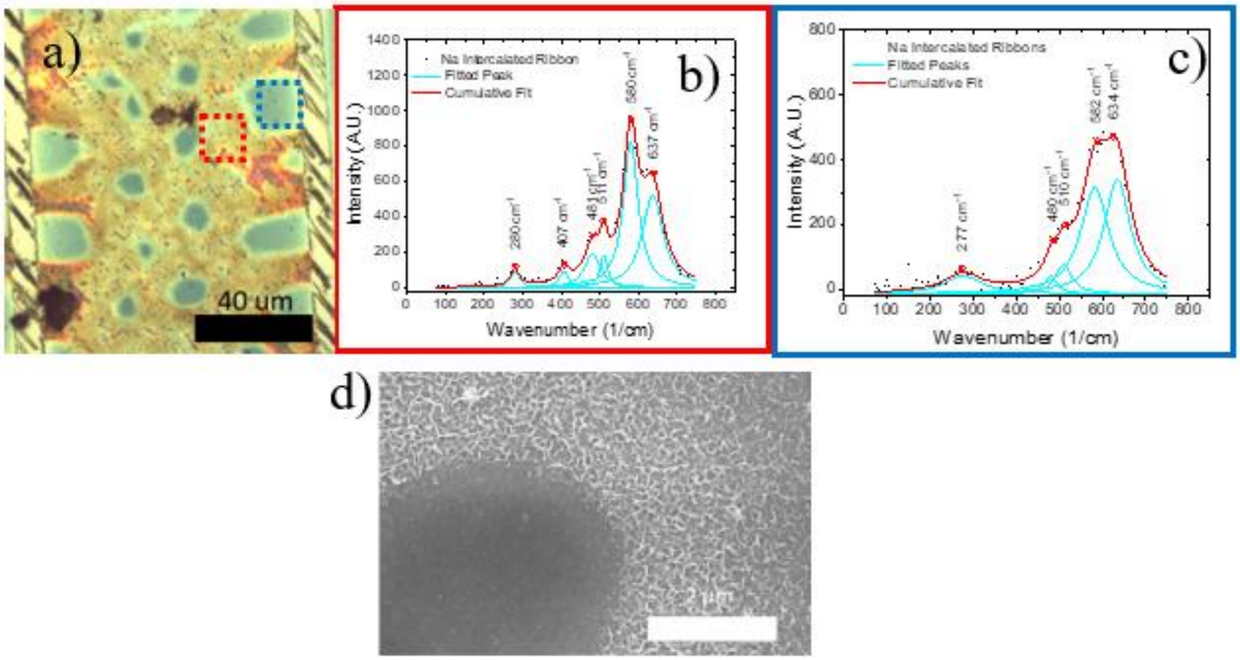

Figure 5-7: (a) Optical Image, (b-c) Raman spectra, and (d) SEM Image of Na^+ intercalated microribbons. Interesting to note that despite the differing colors, both regions successfully intercalated, and the edges of the blue regions have very interesting structural characteristics in the form of nanowalls.

Following intercalation, the structure was analyzed using optical and scanning electron microscopy as well as Raman spectroscopy to determine the effectiveness of the intercalation and its impact on the structure. The optical images indicated that there were two regions, similar to previous attempts, light blue circles in a brown sheet (Figure 5-7.a). Raman spectroscopy of these regions, however indicated that both had been successfully intercalated with sodium, as seen by the peak shift of the 650cm^{-1} peak and the 575cm^{-1} peak, as well as the formation of a doublet in the 500cm^{-1} peak [115] (Figure 5-7 b-c). In addition, though the blue regions have less strong peaks than the other regions, they still have very clear and distinguishable Raman peaks, indicating far better ordering than simply cycling. SEM of these regions also revealed a very interesting structural feature, which is that these regions are surrounded by nanowalls on the surface of the film(Figure 5-7 d.).

Section 5.4 Transformation of Water-Stabilized Manganese Birnessite to Alkali and Alkaline Birnessite via Cycled Intercalation

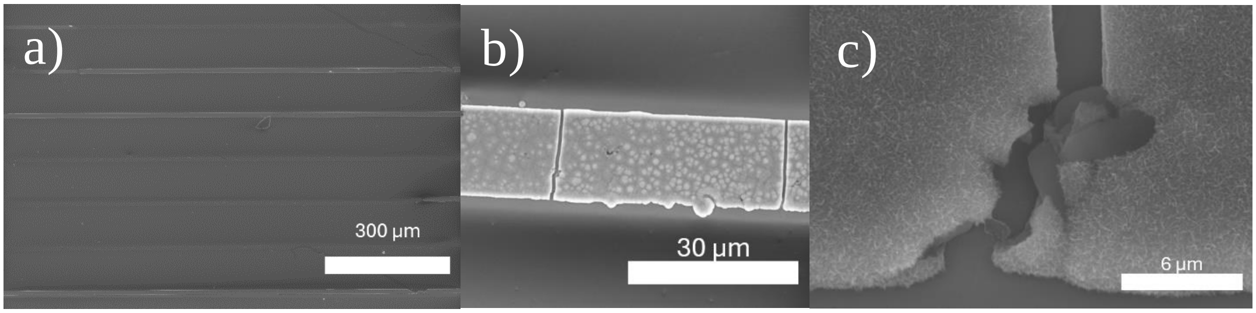

Figure 5-8: (a)100 x magnification SEM image of patterned MnO_2 microribbons. (b) 1Kx magnification SEM of 20 µm ribbon. (c)20Kx magnification SEM of a crack in a ribbon. The laminar surface under the ribbons can be seen, as well as the risk of delamination of the thin ribbons with the patterning

Following the successful intercalation of sodium into the birnessite, a wide range of alkali (Li$^+$, Na$^+$, and K$^+$) and alkaline (Ca$^+$) ions were intercalated into the birnessite structure. To prevent the growth of MnO_2 on the step edges (Figure 5-7.a) we changed the patterned design to ribbons from 100 µm to 20 µm separated by 100 µm (Figure 5-8.a), which successfully prevented the formation of these structures. However, the smaller ribbons suffered significant delamination due to lower surface area coverage. We also observed in the 20 µm ribbons the formation of cracks only approximately perpendicular to the ribbon direction (Figure 5-8.b), as opposed to perpendicular to the step edge, as seen previously (Figure 5-2.a). These cracks also revealed the laminar surface of the MnO_2 underneath the nanofibrous surface. This confirms the observations made in Chapter 3 that we were achieving laminar growth in our films.

To confirm the successful intercalation of the ions into the manganese birnessite, we conducted XPS of the intercalated films to observe the inclusion of the desired ions into the structure and the change in Mn 3s formal valence. To take this XPS data, we utilized a Kratos Supra$^+$ X-ray photoelectron spectrometer operating in small spot mode using monochromatized Al Kα radiation (ħω=1486.7 eV), at an anode power of 280 W and a base pressure of 5×10^{-9} torr. The high-resolution spectra were collected at pass energies of 20eV and then deconvoluted using 30 percent Lorentzian Gaussian-Lorentzian line shapes and a Shirley background for fitting. Following the intercalation of sodium (Figure 5-9.a-b) we observed the presence of a Na 1s peak at 1072.0 eV, which lies above that of metallic Na at 1071.4 eV [133], but below that of α-$NaMnO_2$ at 1072.2 eV [134]. This indicates that Na^+ has intercalated into the structure, but it is interacting with it less strongly than in the 2x2 tunnel, which is expected. We also observe an Mn 3s peak splitting of 5.06 eV, demonstrating a formal valence of +3.27, which indicates a stoichiometry of $Na_{0.73}MnO_2$. Similarly, when intercalating potassium(Figure 5-9.c-d), we observe a K $2p_{1/2}$ positioned at 293.7 eV, which is similar to that of K_2O[135], indicating the formation of expected K-O bonds from intercalation. It is important to note that this K peak is hidden in the C KLL auger peak and the CF_3 from etching and, therefore, may not be fully representative. We also observe an Mn 3s peak splitting of 5.62, indicating a formal valence of 2.62, which is lower than expected, potentially due to surface damage or UHV reduction. Finally, we also observed in the XPS post-Ca intercalation (Figure 5-9.e-f) the appearance of a Ca $2p_{1/2}$ peak at 347.8 eV after intercalation, similar to that of $Ca(OH)_2$ [136], indicating the intercalation of ionic Ca^{+} as well as a Mn 3s peak splitting of 4.62, indicating a formal valence of +3.74. This implies a stoichiometry of $Ca_{0.13}MnO_2$ after intercalation. The XPS of Li after intercalation was not possible due to the overlap of the Li 1s and the Mn 3p. However, the confirmation of Na, K, and Ca intercalation allows us to confirm the capability to intercalate both alkali and alkaline metals.

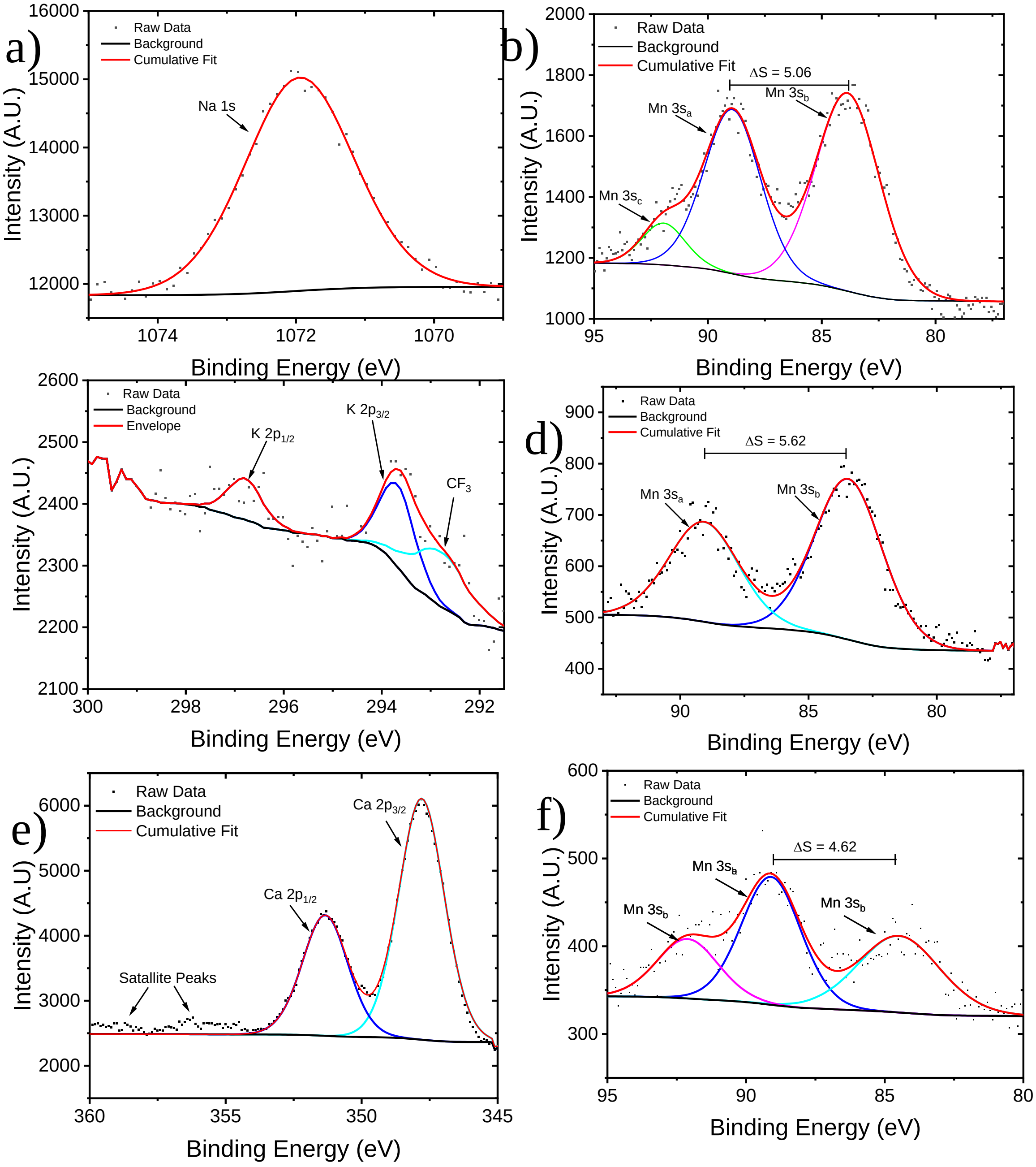

Figure 5-9: (a)Na 1s (c) K 2p (e) Ca 2p and (b,d,f) Mn 3s high-resolution XPS spectra after (a,b) Na, (c,d) K, and (e,f) Ca intercalation. The clear presence of ionic peaks for each intercalant indicates successful intercalation of the ions into the birnessite structure.

The parameters for the intercalation are described in the table below.

Table 5.1. Intercalation Parameters

Intercalant	Solution Salt	Potential Window	Scan Rate
Lithium	1M $LiNO_3$	-0.5 V to 0.5 V	5 mVs^{-1}
Potassium	1M KNO_3	-0.1 V to 1 V	5 mVs^{-1}
Sodium	1M $NaNO_3$	-0.5 V to 0.5 V	5 mVs^{-1}
Calcium	1M $Ca(NO_3)_2$	-1 V to 1 V	5 mVs^{-1}

Section 5.5 Gas Sensing Results from MnO_2 Microribbon Structures

Following successful intercalation, initial tests were done on non-intercalated microribbons gas sensing capabilities to use as a comparison for future gas sensing measurements against intercalated ribbons. To do this, these devices were exposed to 5 ppm NH_3 and NO_2 with a variable humidity N_2 background to observe the effect of water on the sensor performance.

The response of these sensors (Figure 8) shows a similar enhancement in response/recovery (τ_{res}/ τ_{rec}) as other TMO-graphene heterostructures at room temperature, with a reduction of τ_{res}/τ_{rec} to the order of 1000-2000s, 1498.7 ± 49.4s/1485 ± 43s for 5ppm NO_2 (Figure 8.a), and 867.3 ± 161.1s/945.5 ± 110.5s for 5ppm NH_3 (Figure 8.b) in dry N_2[76]. In addition, it also shows exceptional SNR, with a 40.7 ± 2.1 dB response to NO_2, and a 46.8 ± 0.9 dB response to NH_3, as noise is a significant limiting factor on LOD and the ability of response to be amplified, indicating that despite the relatively low responsivity of the sensors (1.94 ± 0.23 % to NH_3 and -0.97 ± 0.20 % to NO_2) they can be amplified to generate a much higher signal using relatively simple circuity[137].

The effect of humidity on the system, however, was not similar to what would be expected in transition metal oxide sensors[76, 138, 139]. Traditionally, water acts as a competitor for the active sites on TMO gas sensors, which reduces the responsivity and limits the other sensing characteristics of TMO and TMO heterostructure sensors. But in these devices, the presence of water improved responsivity and τ_{res}/τ_{rec} time for NO_2 to -3.76 ± 0.33 % and 1368.7 ± 66.7s/418.3 ± 300.7s respectively, as well as making the response far more stable. In addition, on the NH_3 response, a secondary response of the opposite sign was observed in the presence of water, with a τ_{res}/τ_{rec} of 66.4 ± 41.7s/7.5 ± .03s, and a responsivity of -0.26 ± 0.03%, which we have not seen described in the literature.

An explanation for this response can be found in the structure of water-stabilized birnessite. In this material, two layers of defected and negatively charged MnO_{2-x} are compensated for and kept stable by polar H_2O and Mn^{+2} ions in the interlayer[140]. In this structure, NO_2, which will be reduced to NO_2^- cannot enter the interlayer, as it would destabilize the structure and can only react with the surface. This causes our traditional P-type redox gas sensing response. However, in the presence of high atmospheric water content, the ability of H_2O to screen ionic molecules allows for it to enter the interlayer region, significantly enhancing the response[141]. This also provides an explanation for why the τ_{rec} reduces to $\frac{1}{3}$ that of a dry environment, as the unstable NO_2^- in the interlayer is removed significantly faster than traditional redox recovery. The ability of water to facilitate interlayer intercalation is also implicated in the secondary response in NH_3. In both 0% and 100% RH tests, the NH_3 τ_{res}/τ_{rec} and responsivity are similar, changing to 585.8 ± 213s/1088.9 ± 89.4s and 1.45 ± 0.2 %. However, in the presence of high atmospheric water, there is a secondary response of opposite polarity (R_1). This is explained by the fact that NH_3, which oxidizes to NH_3^+ in the sensor, can readily intercalate into the negatively charged interlayer without the assistance of water. However, in an excess water environment, it can also force out excess water molecules, taking their place in stabilizing the structure, before the traditional redox activity takes over. This helps to provide evidence of intercalation response in the sensors, and a path forward on intercalation-based gas sensing on molecular size and charge.

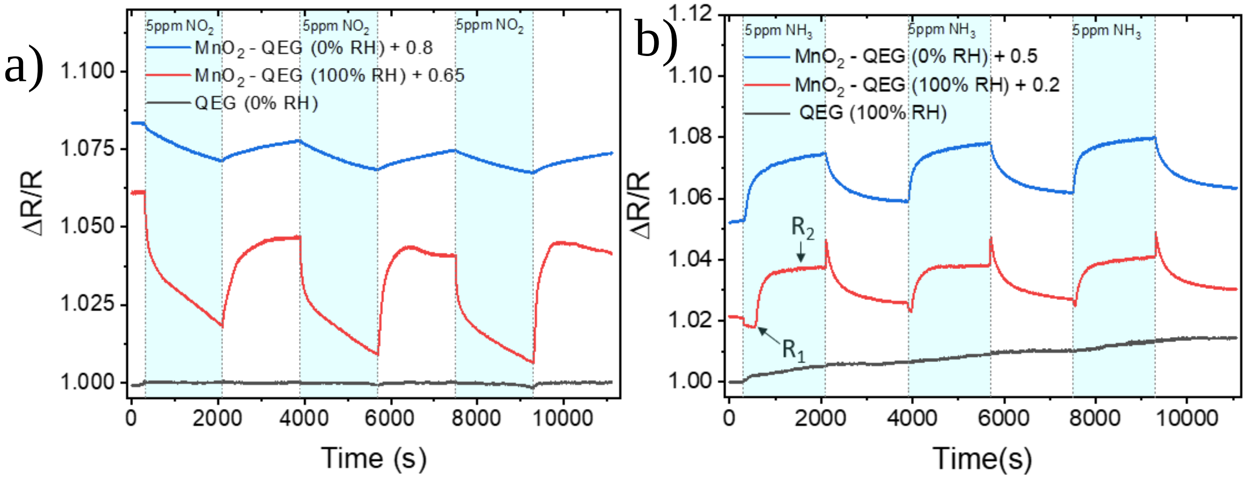

Figure 5-10: Gas sensing response of 100 µm wide ribbons of δ-MnO_2*-QEG and bare QEG to (a)* NO_2 *and (b)* NH_3 *at variable dilution humidities. In both responses, it can be seen that the* MnO_2 *offers significant enhancement over the bare graphene and that the presence of water significantly improves both the response/recovery times and responsivity of the δ-*MnO_2 *heterostructures. Additionally in the* NH_3 *test two distinct responses are observed in the presence of water (*R_1 *and* R_2*), indicating it allows for an intercalation effect in the sensor response.*

Chapter 6: Graphene-Based Biological Sensors

SARS-CoV 2, the virus responsible for COVID-19, a worldwide pandemic originating in late 2019, underscored the threat that a wide range of infectious diseases continues to pose despite the significant advances in modern medicine. One of the key factors in combating the pandemic was the availability of accurate and widespread testing for the virus[2, 3], as early treatment would significantly limit the spread and severity of any given COVID-19 infection[3, 142]. Despite this, testing for COVID-19, especially early in the pandemic, was often limited and haphazard[143]. This was, in part, due to limitations to the biological sensing capabilities, which we, with this work, are attempting to address[144].

There were two commonly used methods to detect COVID-19 infection in the general population. The gold standard for testing is polymerase chain reaction (PCR) tests, which require a lab environment and involve the multiplication and measurement of viral RNA. This process could take approximately 2-3 days to return a diagnosis to a patient (to be discussed further in C 4.1) [144]. The alternate tests, which were generally referred to as "Rapid-Tests" (RT) used enzyme-linked immunosorbent assays (ELISA) with a variety of transduction methods to detect the virus in a non-laboratory (to be discussed further in C 4.2). Despite this significantly greater availability and lower operation requirements, it had a much higher false negative chance and a worse limit of detection[144]. As a result, RTs were significantly less accurate and often were not accepted as valid. This limited the usability of RTs outside of initial diagnostics, despite the much greater accessibility and lower cost of these methods, hindering the ability of governments to control the spread of the virus.

Overcoming the limitations of these techniques has been the subject of significant research interest, with nanomaterial enhanced sensing, e.g. graphene conduction channels, being an attractive candidate due to improved electrical characteristics[71] and high active surface area[71], significantly lower facilities requirements[145]. A more detailed discussion of this will take place later in this chapter (C 6.3)

Section 6.1: Overview of PCR testing

PCR was originally discovered in the 1980s by Mullis et al. [146, 147]. Previously to produce large amounts of DNA the oligonucleotides, the amino acids that build DNA molecules, had to be produced de novo, meaning manually from simple organic structures. These produced oligonucleotides then had to be forcibly constructed into the desired DNA molecule, again by hand. This process was both complex and had significant room for error, limiting the ability of even experienced scientists to produce large quantities of DNA, it also could not target unknown DNA or easily test for the presence of DNA [146]. PCR by contrast, uses a controlled reaction between a DNA template and constructed primer molecules to produce potentially infinite amounts of DNA for any arbitrary sequence. The PCR process is as follows. Initially, the target DNA, and a primer, a molecule that specifically binds to a set of oligonucleotides, are added to the solution. This solution is then heated to denature the DNA molecule to approximately 95 °C, before cooling briefly to allow for hybridization between the primer and the DNA strands. It is then cooled further to approximately 30 °C where a polymerase is added, which serves to add new base pairs onto primed DNA strands, which has effectively doubled the target DNA. This process can then be repeated a potentially infinite number of times to arbitrarily increase the amount of DNA. This allowed for a massive expansion in DNA research[146, 147].

This process takes advantage of several key aspects of the DNA molecule. DNA is symmetric, but each strand has an opposite orientation, with one being 5’-3’ and one being 3’-5’[148]. This allows the process to continue infinitely as protease construction is directional. In addition, while the process was initially made for DNA, it can be relatively trivially adjusted to replicated RNA, as is found in viruses, and can even synthesize new DNA by adding new base pairs into the primer [146]. As a result, this technique is incredibly useful for the detection of pathogens. As if the pathogens' genetics have been sequenced, a sample can be put through the PCR process to amplify the amount of target material to a detectable level. This has led to it being the gold standard of viral detection, as it was for the COVID-19 pandemic[148, 149].

To detect viral RNA using this technique, typically after amplification, the target RNA strand is bound with a fluorophore, a molecule that releases light when reacted with the RNA. This can be used to quickly determine if a piece of viral RNA was present, indicating infection accurately and quickly[148]. Despite this, there are limitations to this technique, mainly that while significantly simpler than older methods of DNA or RNA amplification, it still requires complex precursors and a laboratory environment [148, 149]. This limitation becomes more significant in a pandemic environment, wherein laboratory capability is taxed, slowing the testing process, and limiting the turnaround time. In contrast, RT testing can be conducted by a nonexpert user, at home using a sensor slightly larger than a cell phone[150]. Additionally, these tests can be produced quickly and cheaply, allowing for deployment to far more people than PCR could analyze [151]. It is for this reason that less reliable RT tests were developed using the ELISA method, which would provide a much wider section of the population results on their viral status.

Section 6.2: Overview of ELISA testing

The rapid tests that became commonly available during the COVID-19 pandemic were based upon an alternate biological sensing system, that of enzyme-linked immunosorbent assays (ELISA) [144]. Antibody-antigen reactions have long been known to be a viable way to detect biological pathogens; however, finding a transduction method for these reactions was quite challenging. In the early 1960s, the radioimmunoassay was developed, which allowed for the detection of pathogens by monitoring the reaction between target antibodies and radioactively labeled antigens[152]. However, significant concerns were raised about the safety and scalability of a radioactive diagnostic tool. Consequently, in the late 1960s, enzyme-linked immunosorbent assays were developed [153], which relied on detecting an enzyme-bonded antibody with an immobilized antigen. In its simplest form, a target antigen is immobilized on a plate and then washed in generic animal serum to remove any unbound sites. Following this, a solution of enzyme-conjugated antibodies is added and incubated for a brief period (15 mins – 120 mins)[154]. The plate is then washed, and the substrate solution, which is typically a compound that changes color (colorimetric) or releases photons (fluorometric) in the presence of the conjugated enzyme, allowing for transduction of the system[155]. While this type of ELISA system, termed "direct" is common, it has significant downsides, with a low sensitivity and expensive reagents[154]. To counteract this, alternative ELISA systems have been developed, the "indirect", the "sandwich", and the "competitive" [154].

In indirect ELISA, the initial process remains the same as in direct ELISA. The change however occurs with the target antibody. In the indirect method, the target antibody is not conjugated with the detection enzyme. Instead, a different antibody that will bind with the target is conjugated with the detection enzyme. This is then added after the antibody-antigen binding to attach to the target antibody and provide transduction [154]. This significantly decreases the cost and complexity of the testing, as producing an antibody that will bind to many other antibodies is quite simple, and this removes the need to produce an enzyme conjugation reaction for every target antibody-antigen pair [154]. However, the wide reactivity of the detection antibody leads to a large risk of cross-reactivity and reduced selectivity.

In sandwich ELISA, a capture antibody, as opposed to the target antigen, is bound to the surface of the plate. The target antigen is then coated onto the plate, where it is captured by the applied antibody. After this step, the procedure of the initial ELISA is followed, with the target antibody and detection antibody being coated onto the surface in sequence before transduction. This technique provides the most sensitive of any ELISA method, but the range of use is limited by the need for multivalent antigens with multiple valid antibodies (1 capture, 1 target) [154]. The final type of ELISA is a competition ELISA, which is quite similar to a direct ELISA. In this system the target antibody solution, which may or may not contain the antibody, is mixed with a solution of enzyme-conjugated antibodies that act on the same antigen[154]. The key here is that the reactivity of the conjugated antibody is lower than the target, such that if the target is present, it will not react, hence the competition.

Utilizing these methods, a significant amount of antibody-antigen pairs can be analyzed. However, qualitatively, these tests can very quickly determine if an antibody or antigen pair is present, but quantitatively, the limitations of optical detection become apparent [155, 156]. A highly sensitive optical detector can only be used on a single ELISA sample at a time, limiting the throughput of the technique. Additionally, the range of potential signals limits the usability of the most sensitive optical detectors, as they may be damaged by a high concentration result. This limits the LOD of many ELISA techniques to the nanomolar range[156], which is not suitable for the detection of many biomarkers, such as those associated with cancer.

Section 6.3: Nanomaterial Enhanced ELISA

To overcome these challenges nanomaterial enhancements have been proposed to both enhance the sensitivity and LOD of ELISA-based sensors as well as improve accessibility of these techniques. The initial nanostructure additions were based on noble metal nanoparticles, specifically Au nanoparticles[155, 157]. The mechanism of this enhancement is multifaceted, utilizing both the reactive and optical properties of Au. The first Au nanoparticle-enhanced ELISA used the ease of binding antibodies to Au surfaces to effectively multiply the number of florescent enzymes available for detection with a single binding[157]. This allowed for a LOD of approximately 10 ag mL^{-1}, which was 10^{-8} g mL^{-1} lower than that of traditional fluorescent ELISAs. Other methods utilized the inherent plasmonic properties of Au to generate sizable color changes with limited reactions. For example, Nam et al. utilized the release of cysteine to trigger the aggregation of Au nanoparticles in solution and a resulting color change from red to blue based on the plasmonic resonance in the nanoparticles [158].

In addition to these nanoparticle strategies, thin films of have also been used as a replacement for traditional enzymes in colorimetric detection[159]. Taking advantage of the fact that some metal compounds undergo significant color change during redox reactions, such as manganese oxide, which Peng et al. utilized to detect a wide variety of biomarkers using traditional ELISA techniques[160]. However, despite this, the limitations of traditional ELISA methods in terms of optical equipment remain, with high-quality optical signal transduction requiring expensive and large equipment laboratory equipment. As a result, ultra-high sensitivity and LOD ELISA systems remain limited to the research settings.

Section 6.4: Graphene-Based ELISA Systems

While optical measurement is a limitation of traditional ELISA systems, those based on the ELISA mechanism, the antigen-antibody binding, utilizing differing transduction methods, have proven fertile ground to produce high-sensitivity and low LOD sensors. The most common ELISA-derived sensor is the electrochemical sensor, which monitors the change in electrical response to the antibody-antigen binding event [161]. A wide variety of electrochemical measurements can be sensitive to this binding event and have been utilized in immunoassays, including cyclic voltammetry[162-164], electro-impedance spectroscopy[162, 164, 165], and differential pulse voltammetry[162, 164].

It is also in this field of electrochemical immunosensors that graphene has seen the most successful use, as its high conductivity can provide an excellent platform for the transduction and enhancement of electrochemical signals[162]. In these systems, biomarkers are bonded to graphene, typically antibodies, and then the reaction is measured via changes in the redox activity of the graphene biomarker surface. [162-164]. Using this methodology limits detection as low as 100 ag mL^{-1}. However, these devices are utilizing graphene oxide, as using covalent functionalization via the COOH groups on graphene oxide allows significantly more flexibility in terms of organic molecule utilized [73]. However, using graphene oxide or reduced graphene oxide significantly reduces the electrical properties of the graphene surface[112], limiting the performance of these sensors, which we seek to overcome using pristine EG on SiC.

Pristine graphene biological sensors have also been produced but they are relatively few in number[73, 150, 166]. These sensors rely on a noncovalent interaction between graphene and a crosslinker, which can bond via π-π stacking[150] or cation-π[166]. This crosslinker then binds the antibody, and the effect of the antibody-antigen binding event can be detected via changes in the graphene conductivity and doping. These devices are also universally graphene solution-gated field effect transistors, wherein the transduction mechanism is the change in the Dirac point via the binding event[73, 150, 166]. These devices have produced LODs on the order of 1fg mL^{-1} and response times on the order of 20 minutes. While these devices are exciting applications of the graphene biosensor technology, the production and use of solution-gated GFETs is quite complex and the response time is relatively slow, which limits the usability of these sensors outside of the laboratory context. In contrast, the sensor that we discuss and developed relies only on simple potentiometric measurement on a 2-contact device and produces a significant response in 30 seconds with an LOD of 1ag mL^{-1}, a significant improvement on all fronts, and this will be discussed in more detail later in this dissertation (Chapter 7)

Chapter 7: Biological Sensing Utilizing Epitaxial Graphene-Silicon Carbide Heterostructures

As discussed previously (C. 4) graphene has seen significant utilization in the production of biological sensors in recent years[73, 150, 165, 166]. However, many of these devices are designed as IGFETS, which rely on detecting changes in the Dirac voltage due to biological binding events [73, 150, 165, 166]. The complexity of such devices and the challenges of solution-based systems in general limit the extension of these sensors outside the laboratory context [167].

In addition, the most easily accessible and widely used graphene for device fabrication is that produced by CVD on copper, which is then transferred to Si or SiO_2 substrates. This graphene is strongly influenced by the substrate, with both substantial substrate-induced doping[40, 168, 169], and phonon electron coupling [17, 40] which limits the sensing capabilities of the graphene surface. Suspended freestanding graphene eliminates these limitations but presents such significant fabrication complexity as to be unfeasible [15, 170, 171]. Epitaxial graphene, with its quasi-freestanding nature, allows us to access these properties on a fully lithography-compatible substrate, which we sought to utilize to improve existing graphene biosensors and transition from a FET-based detection to a simpler resistometric system, starting with the detection of the SARS-COV-2 virus.

Section 7.1: Ultra-Sensitive Detection of COVID-19

Following the outbreak of the COVID-19 Pandemic, we attempted to create a sensor based on the epitaxial graphene surface to detect SARS-COV-2. To do this, we bound SARS-COV-2 antibodies onto the graphene surface using poly-L-lysine (PLL), which has been demonstrated as a crosslinker to graphene in the literature[12]. We then tested the device by increasing dilutions of the purified spike protein, which was diluted in DI water. We tested and detected concentrations down to 1 agmL^{-1}, three orders of magnitude lower than any other sensor demonstrated in the literature. We also tested the sensor with clinical and aerosol samples, achieving a 100% correct diagnosis rate among 12 clinical samples, and showed the ability to detect 60 copies mL^{-1} in aerosol form. Further information on this testing can be found in the paper S.Kim et al. published in Biosensors and Bioelectronics in 2022[12].

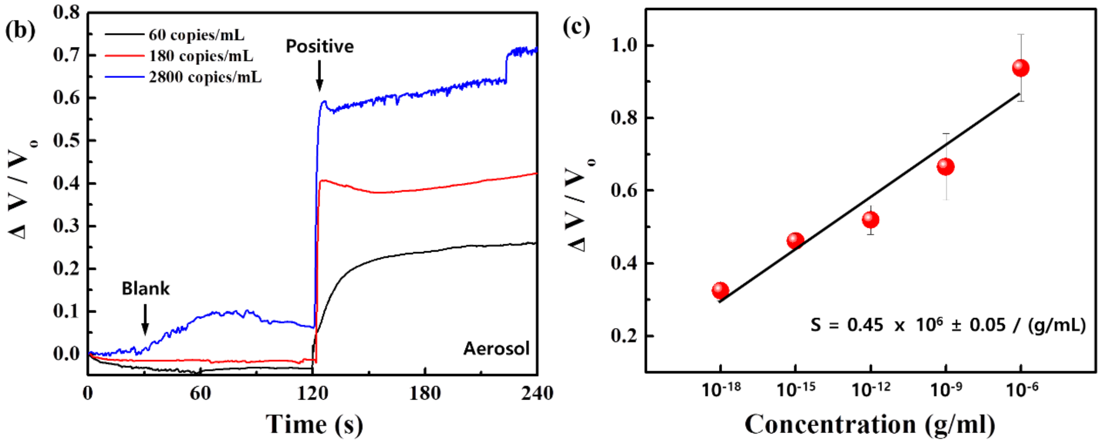

Figure 7-1 (b) Aerosol and (c) droplet response for the SARS-COV-2 Epitaxial graphene sensor to purified S2 Spike protein, showing a limit of detection of approximately 1 agmL^{-1} Reproduced from [12]

Section 7.2: Investigation of the Mechanism of Single-Binding Detection

A limit of detection of the order of 1agmL^{-1} implies the detection on the order of single binding events, which has been reported nowhere in the literature. To understand this result we need to better understand the mechanism of detection of the sensor. In the T-test of the concentration curve, we identified two regions of significance, one for concentrations above 1ngmL^{-1}[12], which we associate with normal charge transfer. In addition, the region below 1pg mL$^{-1,}$ which is the mechanism for this, is not well understood.

To better understand the causes, I undertook Raman mapping of the sensor's surface during the coating and reaction process. This is because the effect of strain and doping on graphene can be extracted from changes in the 2D and G peak positions[172]. This mapping

(Figure 7.2) indicates that the initial coating with PLL exhibits a primarily doping-based effect on the Graphene crystal with an ~80% doping contribution to the shift. The later coating steps, as well as the antibody reaction at 1 agmL^{-1}, create a purely strain-based shift, with the average peak positions moving to lower compressive strain with each step.

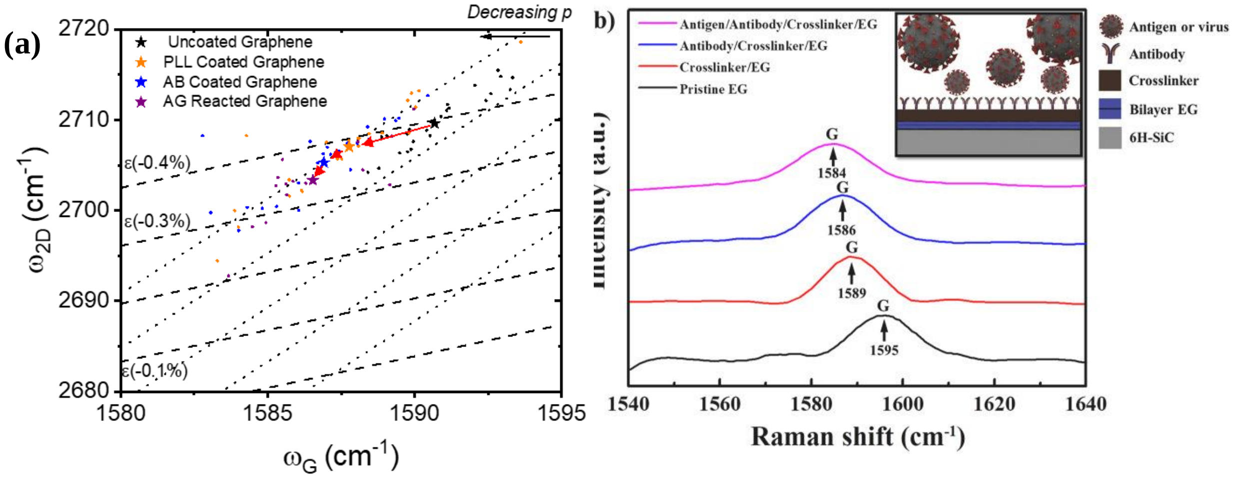

Figure 7-2 (a).2D vs G peak position tracking of 25 points across the sample surface with each step of the coating and detection process. From this, we can see the PLL step is primarily doping, and the remaining steps are almost entirely strain based.(b) Example of shift in G peak, reproduced from[12].

This Raman is consistent with a scenario wherein the PLL crosslinker creates an opposing polarization field to that produced by the Si-H bonds, which is what generates the inherent hole doping in the graphene[63]. This is due to the protonated amines of the PLL forming cation-π interaction bonds with the graphene surface[173]. This also creates a small tensile strain in the lattice, so a reduction in inherent compressive strain in this step well is observed. Later coating steps lead to small changes in strain, but the presence of significant strain changes with 1 agmL^{-1} indicates that this is causing significant changes in the graphene lattice. We believe this is due to the deprotonation of the amine groups by the antibody-antigen interaction, creating a large inhomogeneous strain, which also causes the resistance change.

To test this theory, we conducted tests on alternate substrates that would either not exhibit the competing polarization fields, Ca and Mg intercalated EG[174]. In these experiments, the Mg intercalated EG exhibited a response that was indistinguishable from the blank (Figure 7.3b), while for the Ca intercalated EG we observed a response of 1%, with a blank response of -2% (Figure 7.3a), which is 20 times less than that observed in H intercalated graphene, consistent with our previous description of the system.

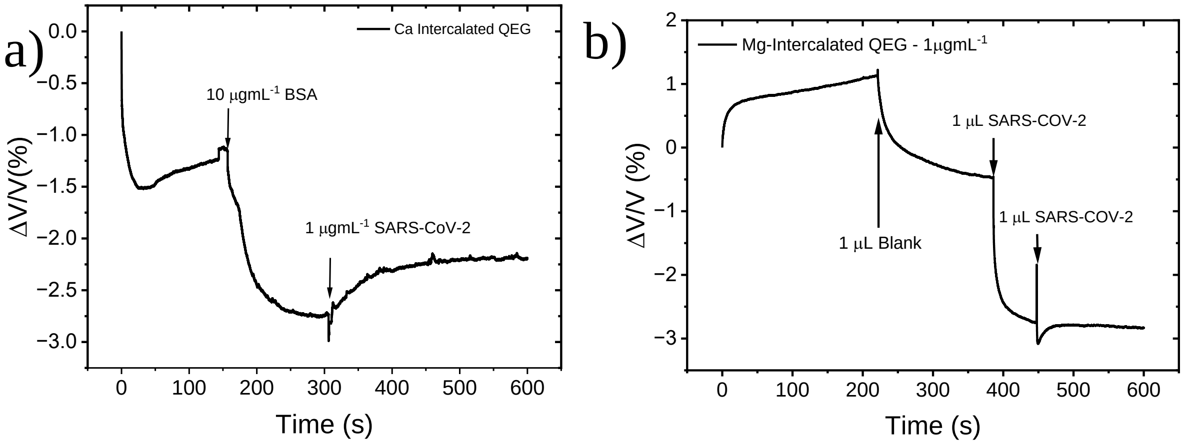

Figure 7-3: Response of (a) Ca intercalated (b) Mg intercalated QEG biosensors to 1μgmL^{-1} SARS-CoV-2 spike protein. The lack of strong response provides additional evidence for the proposed mechanism, relying on the unique characteristics of QEG

We also conducted the same experiment on CVD graphene on SiO_2, from which we got similar results, indicating that the novel properties of QEG that we identified are the primary cause for the anomalously high responsivity of the sensors.

Section 7.3: Detection of Influenza using QEG Biosensors.

Following the investigation of the detection mechanism, we elected to attempt to detect additional antibody-antigen pairs, focusing on the influenza virus. Influenza is a useful target as it has a wide variety of variants, H1N1 and H3N2, for example[175]. The available antibodies have a wide range of sensitivities and selectivity to these viruses[176], which allow us to test both the ability of the QEG biosensor to handle complex biological systems, as well as its ability to be extended to a variety of antibody-antigen interactions.

To test this, we elected to use four antibodies for H3N2 (008-10053-6c05, 2LC590005A-E02, 1417inf, and ABX17-1G03), which were tested against three strains of influenza (2017 Darwin, 2017 Kansas, and 2016 Singapore) to which they have variable responsivity, which is described in the table below.

Table 7.1. Antibody/Antigen Activity

Antibody/Variant	**Darwin**	**Kansas**	**Singapore**
008	Reactive	Reactive	Reactive
2LC	Nonreactive	Reactive	Nonreactive
1417	Reactive	Reactive	Reactive
ABX	Reactive	Reactive	Reactive

We conducted a crossreactivity test using these antibodies and antigens, testing each antibody and strain pair. From this, we found the reactivities of the sensor were quite low, on the order of 2-3%, but still significantly differentiable from the blank, which had a response of less than 0.5% (Figure 7-4.a). We also observed the expected selectivity of the 2LC antibody, which only detected the Kansas strain as expected.

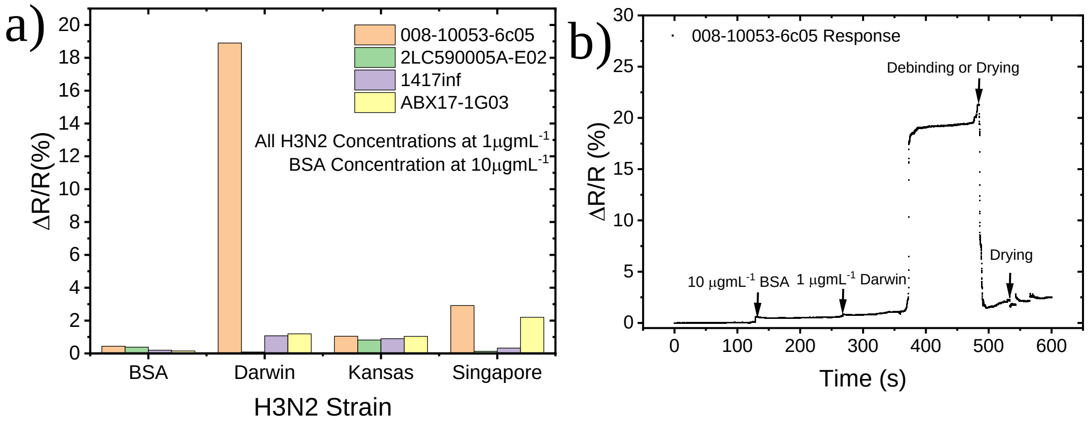

Figure 7-4. (a) Bar chart of responsivity of antibodies to H3N2 influenza strains (b) high response of 008 Antibody to Darwin strain, revealing a strong binding response, not seen in other pairs.

From this experiment we also observed a significantly higher response from the 008 antibody to the Darwin strain, exhibiting a two minute lag time to the response. This could be due to reaction kinetics leading to a slower reaction, but detecting bindings strongly. The remaining responses were quite low, which we believe to be a combination of the relatively low mobility of the QEG samples under test, as well as the use of monoclonal antibodies. Monoclonal antibodies have regular orientations and binding sites, while polyclonal antibodies contain nonoriented structures with a variety of binding locations and activities[177]. This means monoclonal antibodies are much more sensitive to coating orientation and the orientation of the antigen undertest, explaining the lower response in this case. This can be resolved potentially by applying a field to the device during coating to allow for control over the antibody orientation, but that is the beyond the scope of this dissertation.

Section 7.4: Sensitive Detection of Peptide-Protease Binding

While the ability to detect 1 agmL^{-1} of antigen protein is an incredible feat, antibody-antigen reactions present significant limitations, due to the potential for cross-reactivity of different antigen species with the target antibody[178] limiting the practical applications of such a low LOD. In addition, antibody-antigen interactions provide both a static set of available targets, a selective antibody needs to be found for any target antigen[179], and a well-developed infrastructure of existing tests as discussed in Chapter 2.

Alternative protein-based systems provide fertile ground for the extension of the epitaxial graphene biosensor, among these the peptide-protease system is of particular interest due to its ability to be tailored to the application [180] and conduct in-situ chemistry on chip. The key to this system is the protease, which is a protein that selectively binds or cuts a specific series of amino acids, and is common in all biological systems[181, 182]. This allows for the engineering of highly selective target peptides to detect diseases that do not have good antibodies for detection normally. A key challenge of these systems in traditional ELISA is limited activity, which causes the limits of detection to be quite high[183]. Using the Epitaxial Graphene biosensor device we had previously developed to detect antibody-antigen binding, we could overcome this limitation and enable the detection of a wide variety of previously inaccessible biological agents.

To test this concept, we asked our collaborators to produce a novel PLL-Antibody-Peptide system to target tobacco etch virus (TEV) protease, a low-activity, high-selectivity protease [184]. Which we would detect with our sensor. Our initial test lasted 30 minutes, with 1μL of 1μgmL^{-1} TEV protease dropped immediately at the onset (Figure 7-5). The response occurred after approximately 5 minutes and was characterized by a series of sharp spikes and drops in resistance before finishing with a 297% response after 30 minutes. The sharpness of the peaks indicated that we were detecting the binding and unbinding of the protease to the target peptide, but additional work needs to be done to confirm this. Additionally, by integrating the net current in the system (I-I$_{set}$) we found that a significant amount of charge entered the graphene from these reactions (33mC), which exceeds what we have previously seen in the antibody-antigen system.

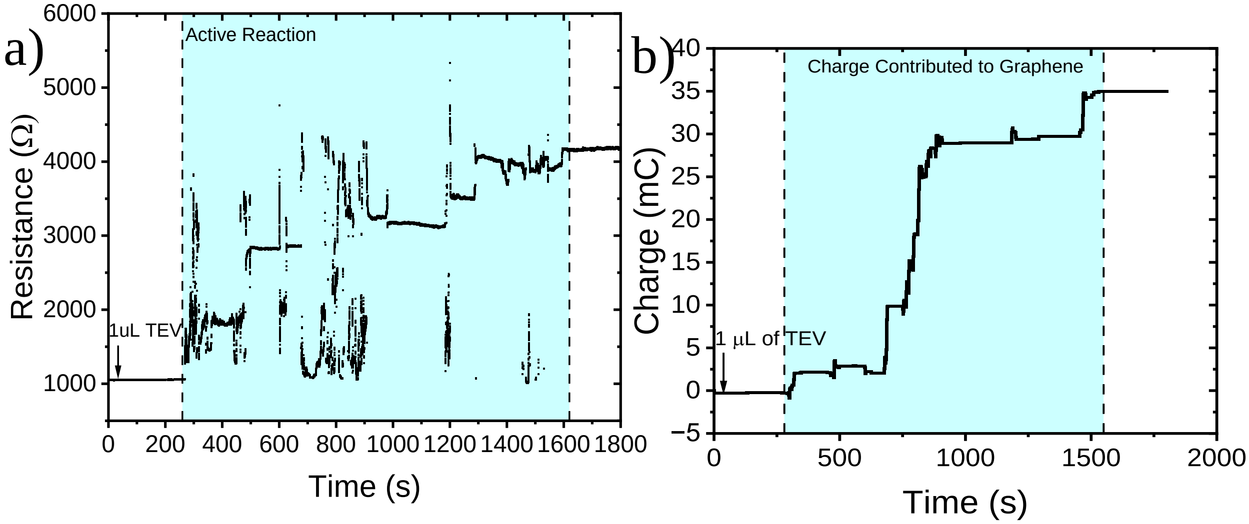

Figure 7-5: (a) Resistance (B) Net Charge over time from the TEV- Graphene biosensor. As can be seen, there is a significant amount of very sharp changes I the resistance, before a stabilization at approximately 300% of the initial resistance, as well as a significant charge transfer into the system

To further investigate this phenomenon, we tested the system with Cathepsin L(CATL) , a much higher activity and lower selectivity protease[185], which should react with the IGG linker. This test responded very similarly to our previous antibody-antigen system (Figure 7.5) with a resistance change of approximately 40% to 1 μgmL^{-1}. This confirmed that our earlier results with TEV were not anomalous and that the peptide significantly enhanced signal over a generic protease.

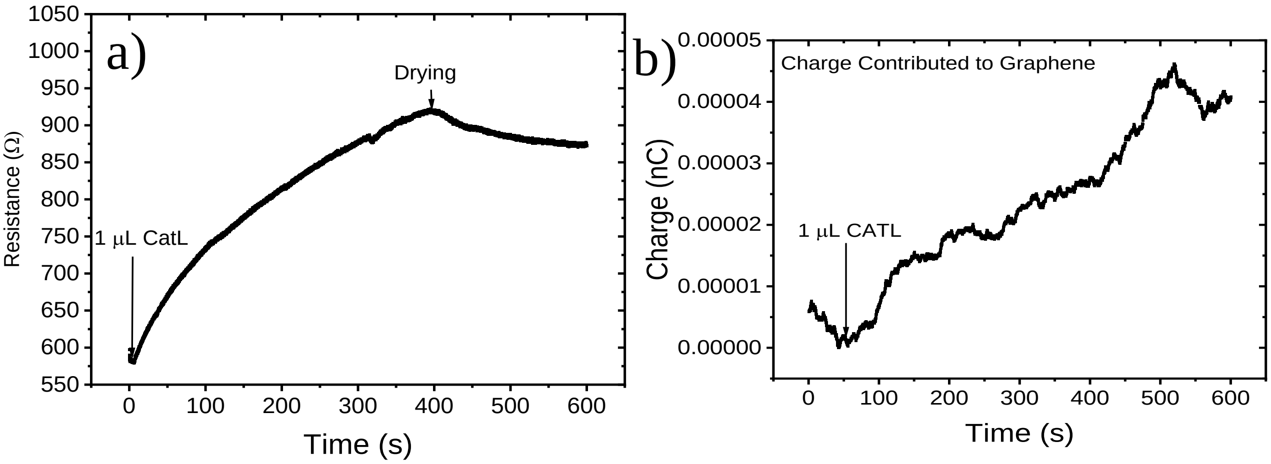

Figure 7-6: (a) Resistance (b) Net Charge versus time of the CATL detection with the PLL-IGG-TEV sensors. This shows that there still is a significant and sharp response to the low selectivity protease, similar to the antibody-antigen reactions, but it is significantly smaller than that for the target protease

We also tested both TEV and CATL, as well as a generic bovine serum on non-functionalized graphene and the PLL-IGG system to determine the effect of both the peptide and full functionalization on the selectivity and sensitivity of the system, which is summarized in Figure 7-7 This indicated to us that the functionalization process provided a massive enhancement to both selectivity and sensitivity and provided a proof of concept for the protease-peptide system moving forwards

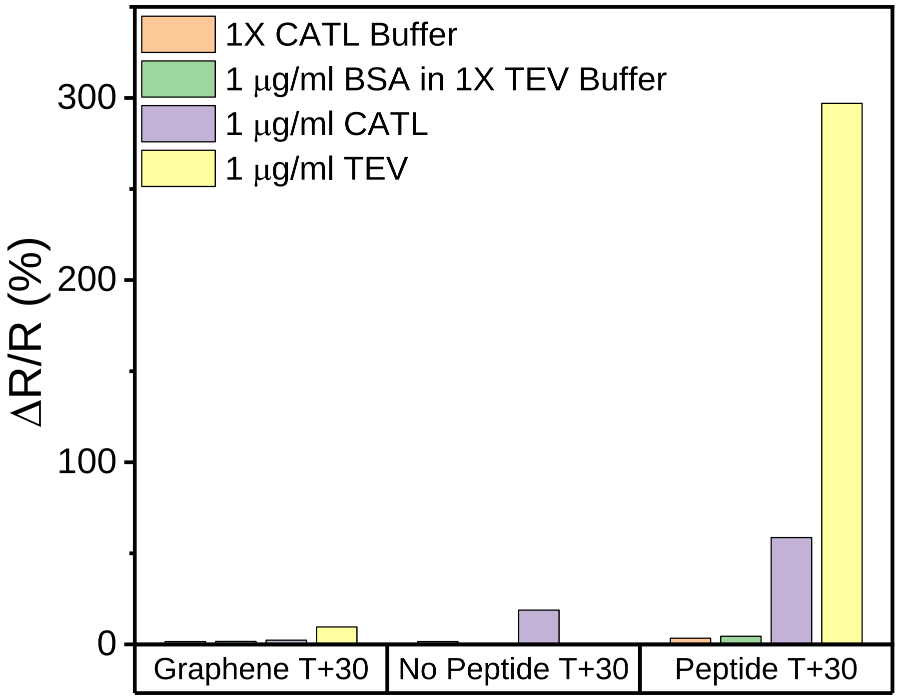

Figure 7-7: Response after 30 minutes of the CATL, TEV, BSA, and buffer solutions on fully functionalized, IGG-PLL functionalized, and non-functionalized graphene. Showing a significant enhancement in sensitivity with functionalization, and high selectivity in the final sensor design.

Chapter 8: Conclusion

The research presented in this dissertation has been focused on the use of graphene to enhance the capabilities of existing functional materials to produce high-sensitivity biological and chemical sensors. In this work, I reviewed previous work on graphene's electrical and structural capabilities and its use as a heterostructure material. Prior work in these areas focused on using CVD graphene, which suffers from significant reductions in its electrical characteristics, or reduced graphene oxide, which has similar challenges. As a result, I elected to use quasi-freestanding epitaxial graphene, as it maintains many of the characteristics of freestanding graphene, including its excellent strain and electrical conductivities, while being on a lithography-compatible substrate. We then used this substrate to develop multiple heterostructures with both inorganic and organic functional materials to produce both gas and biological sensors.

To produce gas sensors, I constructed an electrochemical cell to grow manganese dioxide, which has a natively layered phase, to be used as a molecular sieve sensor. The growth of manganese dioxide on epitaxial graphene was conducted using manganese acetate as a precursor in a three-pulse potentiostatic electrochemical method. Following growth, the resulting film was characterized using Raman spectroscopy, atomic force microscopy, scanning electron microscopy, and x-ray photoelectron spectroscopy. These techniques revealed the growth of a novel water-stabilized birnessite that had never previously been synthesized. These methods were then used to produce optimized 50 nm laminar films that adhered well to the graphene substrate.

Following this, I investigated the capability of intercalating ions into the interlayer of this structure using both potentiostatic and cyclic voltammetry methods. During this, I encountered challenges in ionic diffusion into the thin film, which led us to pattern the underlying graphene surface to allow for better ionic transport into the structure and improve intercalation. Following this patterning, Raman spectroscopy and XPS revealed the successful 100% intercalation of both alkali (Li, Na, K) and alkaline (Ca) ions into the interlayer, allowing for the potential of a tunable molecular sieve.

I also conducted initial gas sensing measurements of the pattered ribbons before intercalation, from which a novel two-part response to NH_3 in high humidity environments was observed, which was due to interlayer water impeding the transport of NH_3 into the interlayer, demonstrating the sieving potential of this structure. This, along with the confirmed intercalation of the structure, opens the potential to produce this tunable gas sieve sensor in the future.

We also produced highly sensitive biological sensors using poly-l-lysine as a crosslinker and antibodies as the reactive element. These sensors were initially constructed to detect SARS-CoV-2, to which they demonstrated a limit of detection of 1 $agmL^{-1}$, better than the PCR test. To account for this incredible sensitivity, I investigated the structural and electrical properties of the sensor using Raman, XPS, and AFM. From this, I determined the ultra-high sensitivity was due to a large-scale strain response enabled by the innate doping, crystallinity, and quasi-freestanding nature of QEG. I then confirmed this finding by conducting tests on alternative epitaxial graphene and CVD graphene intercalations, which worked as I anticipated.

Finally, I expanded the scope of the biological sensor to both other antibody-antigen pairs in the form of influenza, as well as protease peptide bindings, which had the potential to allow for engineered biosensors for a wider variety of diseases. Both of these projects demonstrated the capabilities of epitaxial graphene to significantly improve existing functional materials and provide novel solutions to many environmental and public health challenges.

References

[1] A. F. Franchini, F. Auxilia, P. M. Galimberti, M. A. Piga, S. Castaldi, and A. Porro, "COVID 19 and Spanish flu pandemics: All it changes, nothing changes," *Acta Bio Medica: Atenei Parmensis,* vol. 91, no. 2, p. 245, 2020.

[2] K. Aabed and M. M. A. Lashin, "An analytical study of the factors that influence COVID-19 spread," *Saudi journal of biological sciences,* vol. 28, no. 2, pp. 1177-1195, 2021.

[3] V. Kumar, K. U. Doshi, W. H. Khan, and A. S. Rathore, "COVID-19 pandemic: mechanism, diagnosis, and treatment," *Journal of Chemical Technology & Biotechnology,* vol. 96, no. 2, pp. 299-308, 2021.

[4] B. Li *et al.*, "A comprehensive review on anthropogenic volatile organic compounds (VOCs) emission estimates in China: Comparison and outlook," *Environment International,* vol. 156, p. 106710, 2021.

[5] V. Soni, P. Singh, V. Shree, and V. Goel, "Effects of VOCs on human health," *Air pollution and control,* pp. 119-142, 2018.

[6] P. J. Boogaard, "Human biomonitoring of low-level benzene exposures," *Critical Reviews in Toxicology,* vol. 52, no. 10, pp. 799-810, 2022.

[7] Y. Nagata and N. Takeuchi, "Measurement of odor threshold by triangle odor bag method," *Odor measurement review,* vol. 118, pp. 118-127, 2003.

[8] R. Montero-Montoya, R. López-Vargas, and O. Arellano-Aguilar, "Volatile organic compounds in air: sources, distribution, exposure and associated illnesses in children," *Annals of global health,* vol. 84, no. 2, p. 225, 2018.

[9] L. Spinelle, M. Gerboles, G. Kok, S. Persijn, and T. Sauerwald, "Review of Portable and Low-Cost Sensors for the Ambient Air Monitoring of Benzene and Other Volatile Organic Compounds," *Sensors,* vol. 17, no. 7, 2017, doi: 10.3390/s17071520.

[10] K. S. Novoselov *et al.*, "Electric Field Effect in Atomically Thin Carbon Films," *Science,* vol. 306, no. 5696, pp. 666-669, 2004/10/22 2004, doi: 10.1126/science.1102896.

[11] F. Schwierz, "Graphene transistors," *Nature nanotechnology,* vol. 5, no. 7, pp. 487-496, 2010.

[12] S. Kim *et al.*, "Real-time ultra-sensitive detection of SARS-CoV-2 by quasi-freestanding epitaxial graphene-based biosensor," *Biosensors and Bioelectronics,* vol. 197, p. 113803, 2022.

[13] J. H. Choi, J. Lee, M. Byeon, T. E. Hong, H. Park, and C. Y. Lee, "Graphene-Based Gas Sensors with High Sensitivity and Minimal Sensor-to-Sensor Variation," *ACS Applied Nano Materials,* vol. 3, no. 3, pp. 2257-2265, 2020/03/27 2020, doi: 10.1021/acsanm.9b02378.

[14] M. K. Zhang, W. D. Liu, Y. P. Gong, Q. Liu, and Z. G. Chen, "Graphene/Quantum Dot Heterostructure Photodetectors: From Material to Performance," *Advanced Optical Materials,* p. 2201889, 2022.

[15] X. Du, I. Skachko, A. Barker, and E. Y. Andrei, "Approaching ballistic transport in suspended graphene," *Nature Nanotechnology,* vol. 3, no. 8, pp. 491-495, 2008/08/01 2008, doi: 10.1038/nnano.2008.199.

[16] X. Xu, J. Zhou, Y. Xin, G. Lubineau, Q. Ma, and L. Jiang, "Alcohol Recognition by Flexible, Transparent and Highly Sensitive Graphene-Based Thin-Film Sensors,"

Scientific Reports, vol. 7, no. 1, p. 4317, 2017/06/28 2017, doi: 10.1038/s41598-017-04636-2.

[17] S. Fratini and F. Guinea, "Substrate-limited electron dynamics in graphene," *Physical Review B*, vol. 77, no. 19, p. 195415, 2008.

[18] A. Azizi *et al.*, "Freestanding van der Waals heterostructures of graphene and transition metal dichalcogenides," *ACS nano*, vol. 9, no. 5, pp. 4882-4890, 2015.

[19] W. Shockley, "The theory of p-n junctions in semiconductors and p-n junction transistors," *The Bell System Technical Journal*, vol. 28, no. 3, pp. 435-489, 1949, doi: 10.1002/j.1538-7305.1949.tb03645.x.

[20] J. A. Morton and W. J. Pietenpol, "The Technological Impact of Transistors," *Proceedings of the IRE*, vol. 46, no. 6, pp. 955-959, 1958, doi: 10.1109/JRPROC.1958.286834.

[21] B. R. Pamplin, "A systematic method of deriving new semiconducting compounds by structural analogy," *Journal of Physics and Chemistry of Solids*, vol. 25, no. 7, pp. 675-684, 1964/07/01/ 1964, doi: https://doi.org/10.1016/0022-3697(64)90176-3.

[22] N. G. Bokii and Y. T. Struchkov, "Structural chemistry of organic compounds of the nontransition elements of group IV (Si, Ge, Sn, Pb)," *Journal of Structural Chemistry*, vol. 9, no. 4, pp. 633-667, 1968/07/01 1968, doi: 10.1007/BF00738586.

[23] K. Kaiser, L. M. Scriven, F. Schulz, P. Gawel, L. Gross, and H. L. Anderson, "An sp-hybridized molecular carbon allotrope, cyclo[18]carbon," *Science*, vol. 365, no. 6459, pp. 1299-1301, 2019/09/20 2019, doi: 10.1126/science.aay1914.

[24] E. H. L. Falcao and F. Wudl, "Carbon allotropes: beyond graphite and diamond," *Journal of Chemical Technology & Biotechnology,* https://doi.org/10.1002/jctb.1693 vol. 82, no. 6, pp. 524-531, 2007/06/01 2007, doi: https://doi.org/10.1002/jctb.1693.

[25] B. Xu and Y. Tian, "Diamond gets harder, tougher, and more deformable," *Matter and Radiation at Extremes,* vol. 5, no. 6, p. 068103, 2020/11/01 2020, doi: 10.1063/5.0029519.

[26] P. J. Neuvonen and K. T. Olkkola, "Oral activated charcoal in the treatment of intoxications," *Medical toxicology and adverse drug experience,* vol. 3, no. 1, pp. 33-58, 1988.

[27] N. D. Mermin, "Crystalline order in two dimensions," *Physical Review,* vol. 176, no. 1, p. 250, 1968.

[28] J. A. Venables, G. D. T. Spiller, and M. Hanbucken, "Nucleation and growth of thin films," *Reports on Progress in Physics,* vol. 47, no. 4, p. 399, 1984/04/01 1984, doi: 10.1088/0034-4885/47/4/002.

[29] S. Afsahi *et al.*, "Novel graphene-based biosensor for early detection of Zika virus infection," *Biosensors and Bioelectronics,* vol. 100, pp. 85-88, 2018/02/15/ 2018, doi: https://doi.org/10.1016/j.bios.2017.08.051.

[30] Q. Li, Y. Li, A. V. Fulari, G. S. Ghodake, D. Y. Kim, and G. M. Lohar, "Performance of chemically synthesized Mn3O4/rGO nanocomposite for electrochemical supercapacitor: a cost-effective high-performance electrode," *Nanotechnology,* vol. 31, no. 41, p. 415403, 2020/07/21 2020, doi: 10.1088/1361-6528/ab9f77.

[31] J. Wu, M. Gong, R. C. Schmitz, and B. Liu, "Quantum Dot/Graphene Heterostructure Nanohybrid Photodetectors," in *Quantum Dot Photodetectors*: Springer, 2021, pp. 215-248.

[32] J. Azadmanjiri, V. K. Srivastava, P. Kumar, J. Wang, and A. Yu, "Graphene-supported 2D transition metal oxide heterostructures," *Journal of Materials Chemistry A*, vol. 6, no. 28, pp. 13509-13537, 2018.

[33] J. Poater, X. Fradera, M. Duran, and M. Solà, "The Delocalization Index as an Electronic Aromaticity Criterion: Application to a Series of Planar Polycyclic Aromatic Hydrocarbons," *Chemistry – A European Journal*, https://doi.org/10.1002/chem.200390041 vol. 9, no. 2, pp. 400-406, 2003/01/20 2003, doi: https://doi.org/10.1002/chem.200390041.

[34] P. C. Hiberty, S. S. Shaik, J. M. Lefour, and G. Ohanessian, "Is the delocalized .pi. system of benzene a stable electronic system?," *The Journal of Organic Chemistry,* vol. 50, no. 23, pp. 4657-4659, 1985/11/01 1985, doi: 10.1021/jo00223a052.

[35] D. S. L. Abergel, V. Apalkov, J. Berashevich, K. Ziegler, and T. Chakraborty, "Properties of graphene: a theoretical perspective," *Advances in Physics,* vol. 59, no. 4, pp. 261-482, 2010.

[36] G. Yang, L. Li, W. B. Lee, and M. C. Ng, "Structure of graphene and its disorders: a review," *Science and Technology of Advanced Materials,* vol. 19, no. 1, pp. 613-648, 2018/12/31 2018, doi: 10.1080/14686996.2018.1494493.

[37] M.-Q. Long, L. Tang, D. Wang, L. Wang, and Z. Shuai, "Theoretical Predictions of Size-Dependent Carrier Mobility and Polarity in Graphene," *Journal of the American*

Chemical Society, vol. 131, no. 49, pp. 17728-17729, 2009/12/16 2009, doi: 10.1021/ja907528a.

[38] K. Zou, X. Hong, and J. Zhu, "Effective mass of electrons and holes in bilayer graphene: Electron-hole asymmetry and electron-electron interaction," *Physical Review B,* vol. 84, no. 8, p. 085408, 08/22/ 2011, doi: 10.1103/PhysRevB.84.085408.

[39] S. Bruzzone and G. Fiori, "Ab-initio simulations of deformation potentials and electron mobility in chemically modified graphene and two-dimensional hexagonal boron-nitride," *Applied Physics Letters,* vol. 99, no. 22, p. 222108, 2011/11/28 2011, doi: 10.1063/1.3665183.

[40] X. F. Fan, W. T. Zheng, V. Chihaia, Z. X. Shen, and J.-L. Kuo, "Interaction between graphene and the surface of SiO2," *Journal of Physics: Condensed Matter,* vol. 24, no. 30, p. 305004, 2012/06/19 2012, doi: 10.1088/0953-8984/24/30/305004.

[41] K. Nagashio, T. Yamashita, T. Nishimura, K. Kita, and A. Toriumi, "Electrical transport properties of graphene on SiO2 with specific surface structures," *Journal of Applied Physics,* vol. 110, no. 2, p. 024513, 2011/07/15 2011, doi: 10.1063/1.3611394.

[42] M. D. Pedowitz *et al.*, "Fast Selective Sensing of Nitrogen-Based Gases Utilizing δ-MnO₂-Epitaxial Graphene-Silicon Carbide Heterostructures for Room Temperature Gas Sensing," *Journal of Microelectromechanical Systems,* vol. 29, no. 5, pp. 846-852, 2020, doi: 10.1109/JMEMS.2020.3007342.

[43] X. Zhong, R. Pandey, and S. P. Karna, "Stacking dependent electronic structure and transport in bilayer graphene nanoribbons," *Carbon,* vol. 50, no. 3, pp. 784-790, 2012/03/01/ 2012, doi: https://doi.org/10.1016/j.carbon.2011.09.033.

[44] Y. Zhang *et al.*, "Direct observation of a widely tunable bandgap in bilayer graphene," *Nature*, vol. 459, no. 7248, pp. 820-823, 2009/06/01 2009, doi: 10.1038/nature08105.

[45] Y. Cao *et al.*, "Unconventional superconductivity in magic-angle graphene superlattices," *Nature*, vol. 556, no. 7699, pp. 43-50, 2018/04/01 2018, doi: 10.1038/nature26160.

[46] Y. Yang and R. Murali, "Impact of size effect on graphene nanoribbon transport," *IEEE Electron Device Letters*, vol. 31, no. 3, pp. 237-239, 2010.

[47] T. Enoki, S. Fujii, and K. Takai, "Zigzag and armchair edges in graphene," *Carbon*, vol. 50, no. 9, pp. 3141-3145, 2012/08/01/ 2012, doi: https://doi.org/10.1016/j.carbon.2011.10.004.

[48] J. Hu, S. Schiffli, A. Vallabhaneni, X. Ruan, and Y. P. Chen, "Tuning the thermal conductivity of graphene nanoribbons by edge passivation and isotope engineering: A molecular dynamics study," *Applied Physics Letters*, vol. 97, no. 13, p. 133107, 2010.

[49] M. Terrones *et al.*, "Graphene and graphite nanoribbons: Morphology, properties, synthesis, defects and applications," *Nano Today*, vol. 5, no. 4, pp. 351-372, 2010/08/01/ 2010, doi: https://doi.org/10.1016/j.nantod.2010.06.010.

[50] Y. Huang *et al.*, "Universal mechanical exfoliation of large-area 2D crystals," *Nature Communications*, vol. 11, no. 1, p. 2453, 2020/05/15 2020, doi: 10.1038/s41467-020-16266-w.

[51] L. Yuan *et al.*, "A reliable way of mechanical exfoliation of large scale two dimensional materials with high quality," *AIP Advances*, vol. 6, no. 12, p. 125201, 2016/12/01 2016, doi: 10.1063/1.4967967.

[52] M. Yi and Z. Shen, "A review on mechanical exfoliation for the scalable production of graphene," *Journal of Materials Chemistry A,* 10.1039/C5TA00252D vol. 3, no. 22, pp. 11700-11715, 2015, doi: 10.1039/C5TA00252D.

[53] Y. Zhang, L. Zhang, and C. Zhou, "Review of Chemical Vapor Deposition of Graphene and Related Applications," *Accounts of Chemical Research,* vol. 46, no. 10, pp. 2329-2339, 2013/10/15 2013, doi: 10.1021/ar300203n.

[54] K. M. Daniels *et al.*, "Narrow plasmon resonances enabled by quasi-freestanding bilayer epitaxial graphene," *2D Materials,* vol. 4, no. 2, p. 025034, 2017/02/17 2017, doi: 10.1088/2053-1583/aa5c75.

[55] B. Deng, Z. Liu, and H. Peng, "Toward Mass Production of CVD Graphene Films," *Advanced Materials,* https://doi.org/10.1002/adma.201800996 vol. 31, no. 9, p. 1800996, 2019/03/01 2019, doi: https://doi.org/10.1002/adma.201800996.

[56] V. Miseikis *et al.*, "Rapid CVD growth of millimetre-sized single crystal graphene using a cold-wall reactor," *2D Materials,* vol. 2, no. 1, p. 014006, 2015/01/20 2015, doi: 10.1088/2053-1583/2/1/014006.

[57] J. W. Suk *et al.*, "Transfer of CVD-Grown Monolayer Graphene onto Arbitrary Substrates," *ACS Nano,* vol. 5, no. 9, pp. 6916-6924, 2011/09/27 2011, doi: 10.1021/nn201207c.

[58] H. Zhang, G. Lee, C. Gong, L. Colombo, and K. Cho, "Grain Boundary Effect on Electrical Transport Properties of Graphene," *The Journal of Physical Chemistry C,* vol. 118, no. 5, pp. 2338-2343, 2014/02/06 2014, doi: 10.1021/jp411464w.

[59] S.-H. Bae *et al.*, "Unveiling the carrier transport mechanism in epitaxial graphene for forming wafer-scale, single-domain graphene," *Proceedings of the National Academy of*

Sciences, vol. 114, no. 16, pp. 4082-4086, 2017/04/18 2017, doi: 10.1073/pnas.1620176114.

[60] N. Mishra, J. Boeckl, N. Motta, and F. Iacopi, "Graphene growth on silicon carbide: A review," *physica status solidi (a),* https://doi.org/10.1002/pssa.201600091 vol. 213, no. 9, pp. 2277-2289, 2016/09/01 2016, doi: https://doi.org/10.1002/pssa.201600091.

[61] F. Varchon *et al.*, "Electronic Structure of Epitaxial Graphene Layers on SiC: Effect of the Substrate," *Physical Review Letters,* vol. 99, no. 12, p. 126805, 09/20/ 2007, doi: 10.1103/PhysRevLett.99.126805.

[62] W. Norimatsu and M. Kusunoki, "Formation process of graphene on SiC (0001)," *Physica E: Low-dimensional Systems and Nanostructures,* vol. 42, no. 4, pp. 691-694, 2010/02/01/ 2010, doi: https://doi.org/10.1016/j.physe.2009.11.151.

[63] G. R. Yazdi, T. Iakimov, and R. Yakimova, "Epitaxial Graphene on SiC: A Review of Growth and Characterization," *Crystals*, vol. 6, no. 5, doi: 10.3390/cryst6050053.

[64] S. Mammadov *et al.*, "Work function of graphene multilayers on SiC(0001)," *2D Materials,* vol. 4, no. 1, p. 015043, 2017/01/16 2017, doi: 10.1088/2053-1583/4/1/015043.

[65] C. Riedl, C. Coletti, T. Iwasaki, A. A. Zakharov, and U. Starke, "Quasi-Free-Standing Epitaxial Graphene on SiC Obtained by Hydrogen Intercalation," *Physical Review Letters,* vol. 103, no. 24, p. 246804, 12/10/ 2009, doi: 10.1103/PhysRevLett.103.246804.

[66] C. Zhu *et al.*, "Self-branched α-MnO2/δ-MnO2 heterojunction nanowires with enhanced pseudocapacitance," *Materials Horizons,* 10.1039/C6MH00556J vol. 4, no. 3, pp. 415-422, 2017, doi: 10.1039/C6MH00556J.

[67] J. Park *et al.*, "Approach to multifunctional device platform with epitaxial graphene on transition metal oxide," *Scientific Reports*, vol. 5, no. 1, p. 14374, 2015/09/23 2015, doi: 10.1038/srep14374.

[68] J. Azadmanjiri, V. K. Srivastava, P. Kumar, M. Nikzad, J. Wang, and A. Yu, "Two- and three-dimensional graphene-based hybrid composites for advanced energy storage and conversion devices," *Journal of Materials Chemistry A,* 10.1039/C7TA08748A vol. 6, no. 3, pp. 702-734, 2018, doi: 10.1039/C7TA08748A.

[69] S. Islam *et al.*, "A smart nanosensor for the detection of human immunodeficiency virus and associated cardiovascular and arthritis diseases using functionalized graphene-based transistors," *Biosensors and Bioelectronics,* vol. 126, pp. 792-799, 2019/02/01/ 2019, doi: https://doi.org/10.1016/j.bios.2018.11.041.

[70] A. Maity *et al.*, "Resonance-Frequency Modulation for Rapid, Point-of-Care Ebola-Glycoprotein Diagnosis with a Graphene-Based Field-Effect Biotransistor," *Analytical Chemistry,* vol. 90, no. 24, pp. 14230-14238, 2018/12/18 2018, doi: 10.1021/acs.analchem.8b03226.

[71] E. Vermisoglou *et al.*, "Human virus detection with graphene-based materials," *Biosensors and Bioelectronics,* vol. 166, p. 112436, 2020/10/15/ 2020, doi: https://doi.org/10.1016/j.bios.2020.112436.

[72] W. Gong *et al.*, "Experimental and theoretical investigation for surface plasmon resonance biosensor based on graphene/Au film/D-POF," *Optics Express*, vol. 27, no. 3, pp. 3483-3495, 2019/02/04 2019, doi: 10.1364/OE.27.003483.

[73] F. Walters *et al.*, "A Facile Method for the Non-Covalent Amine Functionalization of Carbon-Based Surfaces for Use in Biosensor Development," *Nanomaterials*, vol. 10, no. 9, doi: 10.3390/nano10091808.

[74] S. V. Streltsov and D. I. Khomskii, "Orbital physics in transition metal compounds: new trends," *Physics-Uspekhi,* vol. 60, no. 11, p. 1121, 2017.

[75] A. K. Bar, C. Pichon, and J.-P. Sutter, "Magnetic anisotropy in two-to eight-coordinated transition–metal complexes: Recent developments in molecular magnetism," *Coordination Chemistry Reviews,* vol. 308, pp. 346-380, 2016.

[76] N. Joshi, T. Hayasaka, Y. Liu, H. Liu, O. N. Oliveira, and L. Lin, "A review on chemiresistive room temperature gas sensors based on metal oxide nanostructures, graphene and 2D transition metal dichalcogenides," *Microchimica Acta,* vol. 185, no. 4, p. 213, 2018/03/10 2018, doi: 10.1007/s00604-018-2750-5.

[77] M. E. Lines, "Influence of d orbitals on the nonlinear optical response of transparent transition-metal oxides," *Physical Review B,* vol. 43, no. 14, p. 11978, 1991.

[78] F. M. Bickelhaupt and E. J. Baerends, "Kohn-Sham Density Functional Theory: Predicting and Understanding Chemistry," in *Reviews in Computational Chemistry*, (Reviews in Computational Chemistry, 2000, pp. 1-86.

[79] E. J. Baerends, O. V. Gritsenko, and R. van Meer, "The Kohn–Sham gap, the fundamental gap and the optical gap: the physical meaning of occupied and virtual Kohn–Sham orbital energies," *Physical Chemistry Chemical Physics,* 10.1039/C3CP52547C vol. 15, no. 39, pp. 16408-16425, 2013, doi: 10.1039/C3CP52547C.

[80] A. Paramekanti, D. D. Maharaj, and B. D. Gaulin, "Octupolar order in d-orbital Mott insulators," *Physical Review B,* vol. 101, no. 5, p. 054439, 2020.

[81] T. Hotta, "Orbital ordering phenomena in d-and f-electron systems," *Reports on Progress in Physics,* vol. 69, no. 7, p. 2061, 2006.

[82] C. Du, H. Wang, F. Yang, and P. C. Hammel, "Systematic variation of spin-orbit coupling with d-orbital filling: Large inverse spin Hall effect in $3d$ transition metals," *Physical Review B,* vol. 90, no. 14, p. 140407, 10/31/ 2014, doi: 10.1103/PhysRevB.90.140407.

[83] D. A. e. Bochvar, N. P. Gambaryan, and L. M. Epshtein, "The Concept of Vacant d Orbitals and the Causes of the Differences between the Properties of Nitrogen and Phosphorus Compounds," *Russian Chemical Reviews,* vol. 45, no. 7, p. 660, 1976.

[84] Y. Tokura and N. Nagaosa, "Orbital physics in transition-metal oxides," *science,* vol. 288, no. 5465, pp. 462-468, 2000.

[85] A. E. Reed and F. Weinhold, "On the role of d orbitals in sulfur hexafluoride," *Journal of the American Chemical Society,* vol. 108, no. 13, pp. 3586-3593, 1986.

[86] M. Risch *et al.*, "Redox Processes of Manganese Oxide in Catalyzing Oxygen Evolution and Reduction: An in Situ Soft X-ray Absorption Spectroscopy Study," *The Journal of Physical Chemistry C,* vol. 121, no. 33, pp. 17682-17692, 2017/08/24 2017, doi: 10.1021/acs.jpcc.7b05592.

[87] R. K. Sharma, A. C. Rastogi, and S. B. Desu, "Manganese oxide embedded polypyrrole nanocomposites for electrochemical supercapacitor," *Electrochimica Acta,* vol. 53, no. 26, pp. 7690-7695, 2008/11/01/ 2008, doi: https://doi.org/10.1016/j.electacta.2008.04.028.

[88] M. Zhang *et al.*, "Pushing the limit of 3 d transition metal-based layered oxides that use both cation and anion redox for energy storage," *Nature Reviews Materials,* vol. 7, no. 7, pp. 522-540, 2022.

[89] M. D. Radin and A. Van der Ven, "Simulating charge, spin, and orbital ordering: application to Jahn–Teller distortions in layered transition-metal oxides," *Chemistry of Materials,* vol. 30, no. 3, pp. 607-618, 2018.

[90] J. D. t. Dunitz and L. E. Orgel, "Electronic properties of transition-metal oxides-II: cation distribution amongst octahedral and tetrahedral sites," *Journal of Physics and Chemistry of Solids,* vol. 3, no. 3-4, pp. 318-323, 1957.

[91] K. Kalantar-zadeh, J. Z. Ou, T. Daeneke, A. Mitchell, T. Sasaki, and M. S. Fuhrer, "Two dimensional and layered transition metal oxides," *Applied Materials Today,* vol. 5, pp. 73-89, 2016/12/01/ 2016, doi: https://doi.org/10.1016/j.apmt.2016.09.012.

[92] H. Li, Y. Li, A. Aljarb, Y. Shi, and L.-J. Li, "Epitaxial growth of two-dimensional layered transition-metal dichalcogenides: growth mechanism, controllability, and scalability," *Chemical reviews,* vol. 118, no. 13, pp. 6134-6150, 2017.

[93] Q. Zhang *et al.*, "One-step hydrothermal synthesis of MnO2/graphene composite for electrochemical energy storage," *Journal of Electroanalytical Chemistry,* vol. 837, pp. 108-115, 2019/03/15/ 2019, doi: https://doi.org/10.1016/j.jelechem.2019.02.031.

[94] S. S. Shendage *et al.*, "Sensitive and selective NO2 gas sensor based on WO3 nanoplates," *Sensors and Actuators B: Chemical,* vol. 240, pp. 426-433, 2017/03/01/ 2017, doi: https://doi.org/10.1016/j.snb.2016.08.177.

[95] V. P. Santos, S. A. C. Carabineiro, P. B. Tavares, M. F. R. Pereira, J. J. M. Órfão, and J. L. Figueiredo, "Oxidation of CO, ethanol and toluene over TiO2 supported noble metal

catalysts," *Applied Catalysis B: Environmental*, vol. 99, no. 1, pp. 198-205, 2010/08/31/ 2010, doi: https://doi.org/10.1016/j.apcatb.2010.06.020.

[96] Y. Wang *et al.*, "NH3 gas sensing performance enhanced by Pt-loaded on mesoporous WO3," *Sensors and Actuators B: Chemical*, vol. 238, pp. 473-481, 2017/01/01/ 2017, doi: https://doi.org/10.1016/j.snb.2016.07.085.

[97] C. Wang, L. Yin, L. Zhang, D. Xiang, and R. Gao, "Metal oxide gas sensors: sensitivity and influencing factors," *sensors*, vol. 10, no. 3, pp. 2088-2106, 2010.

[98] J.-b. Wang *et al.*, "A review of graphene synthesisatlow temperatures by CVD methods," *New Carbon Materials*, vol. 35, no. 3, pp. 193-208, 2020/06/01/ 2020, doi: https://doi.org/10.1016/S1872-5805(20)60484-X.

[99] Y. Liang, H. Dong, D. Aurbach, and Y. Yao, "Current status and future directions of multivalent metal-ion batteries," *Nature Energy*, vol. 5, no. 9, pp. 646-656, 2020/09/01 2020, doi: 10.1038/s41560-020-0655-0.

[100] Y.-L. Huang, C. Pellegrinelli, and E. D. Wachsman, "CO2 and O2 Co-Exchange on Multivalent Metal Oxides," *The Journal of Physical Chemistry C*, vol. 123, no. 29, pp. 17711-17718, 2019/07/25 2019, doi: 10.1021/acs.jpcc.9b03774.

[101] Y. Liao, X. Zhang, R. Peng, M. Zhao, and D. Ye, "Catalytic properties of manganese oxide polyhedra with hollow and solid morphologies in toluene removal," *Applied Surface Science*, vol. 405, pp. 20-28, 2017/05/31/ 2017, doi: https://doi.org/10.1016/j.apsusc.2017.02.012.

[102] C. Wu *et al.*, "Electrochemically activated spinel manganese oxide for rechargeable aqueous aluminum battery," *Nature Communications*, vol. 10, no. 1, p. 73, 2019/01/08 2019, doi: 10.1038/s41467-018-07980-7.

[103] D. Wang *et al.*, "A Superior δ-MnO2 Cathode and a Self-Healing Zn-δ-MnO2 Battery," *ACS Nano*, vol. 13, no. 9, pp. 10643-10652, 2019/09/24 2019, doi: 10.1021/acsnano.9b04916.

[104] W. Zhang, H. Jin, Y. Du, Y. Zhang, Z. Wang, and J. Zhang, "Hierarchical Lamellar-Structured MnO2@graphene for High Performance Li, Na and K ion Batteries," *ChemistrySelect*, https://doi.org/10.1002/slct.202003584 vol. 5, no. 40, pp. 12481-12486, 2020/10/29 2020, doi: https://doi.org/10.1002/slct.202003584.

[105] T. Ozkaya, A. Baykal, H. Kavas, Y. Köseoğlu, and M. S. Toprak, "A novel synthetic route to Mn3O4 nanoparticles and their magnetic evaluation," *Physica B: Condensed Matter*, vol. 403, no. 19, pp. 3760-3764, 2008/10/01/ 2008, doi: https://doi.org/10.1016/j.physb.2008.07.002.

[106] V. C. Bose, K. Maniammal, G. Madhu, C. L. Veenas, A. S. A. Raj, and V. Biju, "DC electrical conductivity of nanocrystalline Mn3O4 synthesized through a novel sol-gel route," *IOP Conference Series: Materials Science and Engineering*, vol. 73, p. 012084, 2015/02/17 2015, doi: 10.1088/1757-899x/73/1/012084.

[107] F. K. Tan, J. Hassan, Z. A. Wahab, and R. a. S. Azis, "Electrical conductivity and dielectric behaviour of manganese and vanadium mixed oxide prepared by conventional solid state method," *Engineering Science and Technology, an International Journal*, vol. 19, no. 4, pp. 2081-2087, 2016/12/01/ 2016, doi: https://doi.org/10.1016/j.jestch.2016.08.002.

[108] C. Julien, M. Massot, R. Baddour-Hadjean, S. Franger, S. Bach, and J. P. Pereira-Ramos, "Raman spectra of birnessite manganese dioxides," *Solid State Ionics*, vol. 159, no. 3, pp. 345-356, 2003/04/01/ 2003, doi: https://doi.org/10.1016/S0167-2738(03)00035-3.

[109] Y. Liu *et al.*, "Manganese dioxide nanosheet arrays grown on graphene oxide as an advanced electrode material for supercapacitors," *Electrochimica Acta,* vol. 117, pp. 528-533, 2014/01/20/ 2014, doi: https://doi.org/10.1016/j.electacta.2013.11.121.

[110] L. Wang, W. Ma, Y. Li, and H. Cui, "Synthesis of δ-MnO₂ with nanoflower-like architecture by a microwave-assisted hydrothermal method," (in English), *Journal of Sol-Gel Science and Technology,* vol. 82, no. 1, pp. 85-91, Apr 2017 2021-03-26 2017, doi: http://dx.doi.org/10.1007/s10971-016-4275-x.

[111] B. Zhao *et al.*, "Self-assembly of ultrathin MnO2/graphene with three-dimension hierarchical structure by ultrasonic-assisted co-precipitation method," *Journal of Alloys and Compounds,* vol. 663, pp. 180-186, 2016/04/05/ 2016, doi: https://doi.org/10.1016/j.jallcom.2015.12.018.

[112] C. Gómez-Navarro *et al.*, "Electronic Transport Properties of Individual Chemically Reduced Graphene Oxide Sheets," *Nano Letters,* vol. 7, no. 11, pp. 3499-3503, 2007/11/01 2007, doi: 10.1021/nl072090c.

[113] S. Dhingra, J.-F. Hsu, I. Vlassiouk, and B. D'Urso, "Chemical vapor deposition of graphene on large-domain ultra-flat copper," *Carbon,* vol. 69, pp. 188-193, 2014/04/01/ 2014, doi: https://doi.org/10.1016/j.carbon.2013.12.014.

[114] K. M. Daniels *et al.*, "Electrochemical Hydrogenation of Dimensional Carbon," *ECS Transactions,* vol. 58, no. 4, pp. 439-445, 2013/08/31 2013, doi: 10.1149/05804.0439ecst.

[115] D. Chen *et al.*, "Probing the Charge Storage Mechanism of a Pseudocapacitive MnO2 Electrode Using in Operando Raman Spectroscopy," *Chemistry of Materials,* vol. 27, no. 19, pp. 6608-6619, 2015/10/13 2015, doi: 10.1021/acs.chemmater.5b03118.

[116] C. M. Julien, M. Massot, and C. Poinsignon, "Lattice vibrations of manganese oxides: Part I. Periodic structures," *Spectrochimica Acta Part A: Molecular and Biomolecular Spectroscopy,* vol. 60, no. 3, pp. 689-700, 2004/02/01/ 2004, doi: https://doi.org/10.1016/S1386-1425(03)00279-8.

[117] V. R. Galakhov *et al.*, "Mn $3s$ exchange splitting in mixed-valence manganites," *Physical Review B,* vol. 65, no. 11, p. 113102, 02/12/ 2002, doi: 10.1103/PhysRevB.65.113102.

[118] A. Bauer *et al.*, "High-precision determination of atomic positions in crystals: The case of $6H$- and $4H$-SiC," *Physical Review B,* vol. 57, no. 5, pp. 2647-2650, 02/01/ 1998, doi: 10.1103/PhysRevB.57.2647.

[119] Z. M. Chan *et al.*, "Electrochemical trapping of metastable Mn³⁺ ions for activation of MnO₂ oxygen evolution catalysts," *Proceedings of the National Academy of Sciences,* vol. 115, no. 23, pp. E5261-E5268, 2018, doi: doi:10.1073/pnas.1722235115.

[120] W. Melitz, J. Shen, A. C. Kummel, and S. Lee, "Kelvin probe force microscopy and its application," *Surface Science Reports,* vol. 66, no. 1, pp. 1-27, 2011/01/01/ 2011, doi: https://doi.org/10.1016/j.surfrep.2010.10.001.

[121] W. Feng-Ping, M. Y. Rafique, A. M. Toufiq, and M. Z. Iqbal, "Canted antiferromagnetic and optical properties of nanostructures of Mn2O3 prepared by hydrothermal synthesis," *Chinese Physics B,* vol. 21, no. 11, p. 117311, 2012.

[122] X. Gu, J. Yue, L. Li, H. Xue, J. Yang, and X. Zhao, "General Synthesis of MnOx (MnO2, Mn2O3, Mn3O4, MnO) Hierarchical Microspheres as Lithium-ion Battery Anodes,"

Electrochimica Acta, vol. 184, pp. 250-256, 2015/12/01/ 2015, doi: https://doi.org/10.1016/j.electacta.2015.10.037.

[123] M. H. Oliveira *et al.*, "Formation of high-quality quasi-free-standing bilayer graphene on SiC(0001) by oxygen intercalation upon annealing in air," *Carbon*, vol. 52, pp. 83-89, 2013/02/01/ 2013, doi: https://doi.org/10.1016/j.carbon.2012.09.008.

[124] S. H. Shim, D. LaBounty, and T. S. Duffy, "Raman spectra of bixbyite, Mn2O3, up to 40 GPa," *Physics and Chemistry of Minerals*, vol. 38, no. 9, p. 685, 2011/06/12 2011, doi: 10.1007/s00269-011-0441-4.

[125] H. Veeramani *et al.*, "Low-Temperature Green Synthesis of Multivalent Manganese Oxide Nanowires," *ACS Sustainable Chemistry & Engineering*, vol. 1, no. 9, pp. 1070-1074, 2013/09/03 2013, doi: 10.1021/sc400129n.

[126] C. S. Widodo, H. Sela, and D. R. Santosa, "The effect of NaCl concentration on the ionic NaCl solutions electrical impedance value using electrochemical impedance spectroscopy methods," *AIP Conference Proceedings*, vol. 2021, no. 1, p. 050003, 2018/10/17 2018, doi: 10.1063/1.5062753.

[127] X. Li *et al.*, "Effects of electrode thickness and crystal water on pseudocapacitive performance of layered birnessite MnO2," *Nanotechnology*, vol. 31, no. 21, p. 215406, 2020/03/10 2020, doi: 10.1088/1361-6528/ab73bf.

[128] T. P. Mofokeng, S. Shabalala, A. B. Haruna, P. V. Mwonga, Z. N. Tetana, and K. I. Ozoemena, "Scalable synthesis of K+/Na+ pre-intercalated α-MnO2 via Taylor fluid flow-assisted hydrothermal reaction for high-performance asymmetric supercapacitors," *Journal of Electroanalytical Chemistry*, vol. 948, p. 117809, 2023/11/01/ 2023, doi: https://doi.org/10.1016/j.jelechem.2023.117809.

[129] A. S. Poyraz *et al.*, "Synthesis of cryptomelane type α-MnO2 (KxMn8O16) cathode materials with tunable K+ content: the role of tunnel cation concentration on electrochemistry," *Journal of Materials Chemistry A,* 10.1039/C7TA03476H vol. 5, no. 32, pp. 16914-16928, 2017, doi: 10.1039/C7TA03476H.

[130] M. Forghani and S. W. Donne, "Method Comparison for Deconvoluting Capacitive and Pseudo-Capacitive Contributions to Electrochemical Capacitor Electrode Behavior," *Journal of The Electrochemical Society,* vol. 165, no. 3, p. A664, 2018/03/08 2018, doi: 10.1149/2.0931803jes.

[131] J. Zhou *et al.*, "Novel Synthesis of Birnessite-Type MnO2 Nanostructure for Water Treatment and Electrochemical Capacitor," *Industrial & Engineering Chemistry Research,* vol. 52, no. 28, pp. 9586-9593, 2013/07/17 2013, doi: 10.1021/ie400577a.

[132] B.-A. Mei, O. Munteshari, J. Lau, B. Dunn, and L. Pilon, "Physical Interpretations of Nyquist Plots for EDLC Electrodes and Devices," *The Journal of Physical Chemistry C,* vol. 122, no. 1, pp. 194-206, 2018/01/11 2018, doi: 10.1021/acs.jpcc.7b10582.

[133] X. Feng and D. F. Cox, "Oxidation of MnO(100) and NaMnO2 formation: Characterization of Mn2+ and Mn3+ surfaces via XPS and water TPD," *Surface Science,* vol. 675, pp. 47-53, 2018/09/01/ 2018, doi: https://doi.org/10.1016/j.susc.2018.04.022.

[134] G. Maresca, M. Ottaviani, K. M. Ryan, S. Brutti, and G. B. Appetecchi, "Improved Compatibility of α-NaMnO2 Cathodes at the Interface with Ionic Liquid Electrolytes," *ChemSusChem,* vol. n/a, no. n/a, p. e202400514, 2024/05/16 2024, doi: https://doi.org/10.1002/cssc.202400514.

[135] S. F. Zaman and K. J. Smith, "A study of K-promoted MoP–SiO2 catalysts for synthesis gas conversion," *Applied Catalysis A: General*, vol. 378, no. 1, pp. 59-68, 2010/04/15/ 2010, doi: https://doi.org/10.1016/j.apcata.2010.01.046.

[136] I. Frateur, A. Carnot, S. Zanna, and P. Marcus, "Role of pH and calcium ions in the adsorption of an alkyl N-aminodimethylphosphonate on steel: An XPS study," *Applied Surface Science*, vol. 252, no. 8, pp. 2757-2769, 2006/02/15/ 2006, doi: https://doi.org/10.1016/j.apsusc.2005.04.012.

[137] G. Jung *et al.*, "Comparison of the characteristics of semiconductor gas sensors with different transducers fabricated on the same substrate," *Sensors and Actuators B: Chemical*, vol. 335, p. 129661, 2021/05/15/ 2021, doi: https://doi.org/10.1016/j.snb.2021.129661.

[138] D. Gu *et al.*, "Visible-light activated room temperature NO2 sensing of SnS2 nanosheets based chemiresistive sensors," *Sensors and Actuators B: Chemical*, vol. 305, p. 127455, 2020/02/15/ 2020, doi: https://doi.org/10.1016/j.snb.2019.127455.

[139] T. Alkathiri *et al.*, "2D Palladium Sulphate for Visible-Light-Driven Optoelectronic Reversible Gas Sensing at Room Temperature," *Small Science*, vol. 2, no. 3, p. 2100097, 2022/03/01 2022, doi: https://doi.org/10.1002/smsc.202100097.

[140] V. A. Drits, E. Silvester, A. I. Gorshkov, and A. Manceau, "Structure of synthetic monoclinic Na-rich birnessite and hexagonal birnessite: I. Results from X-ray diffraction and selected-area electron diffraction," *American Mineralogist*, vol. 82, no. 9-10, pp. 946-961, 1997.

[141] I. V. Leontyev and A. A. Stuchebrukhov, "Electronic Polarizability and the Effective Pair Potentials of Water," *Journal of Chemical Theory and Computation,* vol. 6, no. 10, pp. 3153-3161, 2010/10/12 2010, doi: 10.1021/ct1002048.

[142] Y. Wang *et al.*, "Remdesivir in adults with severe COVID-19: a randomised, double-blind, placebo-controlled, multicentre trial," *The Lancet,* vol. 395, no. 10236, pp. 1569-1578, 2020/05/16/ 2020, doi: https://doi.org/10.1016/S0140-6736(20)31022-9.

[143] E. Alvarez *et al.*, "Limitations of COVID-19 testing and case data for evidence-informed health policy and practice," *Health Research Policy and Systems,* vol. 21, no. 1, p. 11, 2023/01/25 2023, doi: 10.1186/s12961-023-00963-1.

[144] B. Giri, S. Pandey, R. Shrestha, K. Pokharel, F. S. Ligler, and B. B. Neupane, "Review of analytical performance of COVID-19 detection methods," *Analytical and bioanalytical chemistry,* vol. 413, no. 1, pp. 35-48, 2021.

[145] M. Tabata and Y. Miyahara, "From new materials to advanced biomedical applications of solid-state biosensor: a review," *Sensors and Actuators B: Chemical,* vol. 352, p. 131033, 2022.

[146] K. Mullis, F. Faloona, S. Scharf, R. Saiki, G. Horn, and H. Erlich, "Specific enzymatic amplification of DNA in vitro: the polymerase chain reaction," *Biotechnology Series,* pp. 17-17, 1992.

[147] K. B. Mullis, "The unusual origin of the polymerase chain reaction," *Scientific American,* vol. 262, no. 4, pp. 56-65, 1990.

[148] L. Garibyan and N. Avashia, "Research techniques made simple: polymerase chain reaction (PCR)," *The Journal of investigative dermatology,* vol. 133, no. 3, p. e6, 2013.

[149] O. Vandenberg, D. Martiny, O. Rochas, A. van Belkum, and Z. Kozlakidis, "Considerations for diagnostic COVID-19 tests," *Nature Reviews Microbiology,* vol. 19, no. 3, pp. 171-183, 2021.

[150] G. Seo *et al.*, "Rapid Detection of COVID-19 Causative Virus (SARS-CoV-2) in Human Nasopharyngeal Swab Specimens Using Field-Effect Transistor-Based Biosensor," *ACS Nano,* vol. 14, no. 4, pp. 5135-5142, 2020/04/28 2020, doi: 10.1021/acsnano.0c02823.

[151] A. D. Paltiel, A. Zheng, and P. E. Sax, "Clinical and economic effects of widespread rapid testing to decrease SARS-CoV-2 transmission," *Annals of internal medicine,* vol. 174, no. 6, pp. 803-810, 2021.

[152] S. J. Goldsmith, "Radioimmunoassay: Review of basic principles," *Seminars in Nuclear Medicine,* vol. 5, no. 2, pp. 125-152, 1975/04/01/ 1975, doi: https://doi.org/10.1016/S0001-2998(75)80028-6.

[153] R. M. Lequin, "Enzyme Immunoassay (EIA)/Enzyme-Linked Immunosorbent Assay (ELISA)," *Clinical Chemistry,* vol. 51, no. 12, pp. 2415-2418, 2005, doi: 10.1373/clinchem.2005.051532.

[154] M. Alhajj, M. Zubair, and A. Farhana, "Enzyme linked immunosorbent assay," *StatPearls,* 2023.

[155] N. Momenbeitollahi, T. Cloet, and H. Li, "Pushing the detection limits: strategies towards highly sensitive optical-based protein detection," *Analytical and Bioanalytical Chemistry,* vol. 413, no. 24, pp. 5995-6011, 2021/10/01 2021, doi: 10.1007/s00216-021-03566-3.

[156] S. K. Arya and P. Estrela, "Recent Advances in Enhancement Strategies for Electrochemical ELISA-Based Immunoassays for Cancer Biomarker Detection," *Sensors,* vol. 18, no. 7, doi: 10.3390/s18072010.

[157] Y. Wu *et al.*, "Enhanced Fluorescence ELISA Based on HAT Triggering Fluorescence “Turn-on” with Enzyme–Antibody Dual Labeled AuNP Probes for Ultrasensitive Detection of AFP and HBsAg," *ACS Applied Materials & Interfaces,* vol. 9, no. 11, pp. 9369-9377, 2017/03/22 2017, doi: 10.1021/acsami.6b16236.

[158] J.-M. Nam, C. S. Thaxton, and C. A. Mirkin, "Nanoparticle-Based Bio-Bar Codes for the Ultrasensitive Detection of Proteins," *Science,* vol. 301, no. 5641, pp. 1884-1886, 2003/09/26 2003, doi: 10.1126/science.1088755.

[159] L. Gao, Q. Yang, P. Wu, and F. Li, "Recent advances in nanomaterial-enhanced enzyme-linked immunosorbent assays," *Analyst,* 10.1039/D0AN00597E vol. 145, no. 12, pp. 4069-4078, 2020, doi: 10.1039/D0AN00597E.

[160] H. Peng *et al.*, "Versatile High-Performance Electrochemiluminescence ELISA Platform Based on a Gold Nanocluster Probe," *ACS Applied Materials & Interfaces,* vol. 11, no. 27, pp. 24812-24819, 2019/07/10 2019, doi: 10.1021/acsami.9b08819.

[161] Z. Zhang, Y. Cong, Y. Huang, and X. Du, "Nanomaterials-based electrochemical immunosensors," *Micromachines,* vol. 10, no. 6, p. 397, 2019.

[162] G. Manasa, R. J. Mascarenhas, S. J. Malode, and N. P. Shetti, "Graphene-based electrochemical immunosensors for early detection of oncomarker carcinoembryonic antigen," *Biosensors and Bioelectronics: X,* vol. 11, p. 100189, 2022/09/01/ 2022, doi: https://doi.org/10.1016/j.biosx.2022.100189.

[163] R. Wang, J.-J. Feng, Y. Xue, L. Wu, and A.-J. Wang, "A label-free electrochemical immunosensor based on AgPt nanorings supported on reduced graphene oxide for ultrasensitive analysis of tumor marker," *Sensors and Actuators B: Chemical,* vol. 254, pp. 1174-1181, 2018/01/01/ 2018, doi: https://doi.org/10.1016/j.snb.2017.08.009.

[164] H. Lv *et al.*, "Enhanced peroxidase-like properties of Au@Pt DNs/NG/Cu2+ and application of sandwich-type electrochemical immunosensor for highly sensitive detection of CEA," *Biosensors and Bioelectronics,* vol. 112, pp. 1-7, 2018/07/30/ 2018, doi: https://doi.org/10.1016/j.bios.2018.04.025.

[165] V. K. Singh *et al.*, "Fabrication of sensitive bioelectrode based on atomically thin CVD grown graphene for cancer biomarker detection," *Biosensors and Bioelectronics,* vol. 105, pp. 173-181, 2018/05/15/ 2018, doi: https://doi.org/10.1016/j.bios.2018.01.014.

[166] J. Gao *et al.*, "Poly-l-Lysine-Modified Graphene Field-Effect Transistor Biosensors for Ultrasensitive Breast Cancer miRNAs and SARS-CoV-2 RNA Detection," *Analytical Chemistry,* vol. 94, no. 3, pp. 1626-1636, 2022/01/25 2022, doi: 10.1021/acs.analchem.1c03786.

[167] D. Sadighbayan, M. Hasanzadeh, and E. Ghafar-Zadeh, "Biosensing based on field-effect transistors (FET): Recent progress and challenges," *TrAC Trends in Analytical Chemistry,* vol. 133, p. 116067, 2020/12/01/ 2020, doi: https://doi.org/10.1016/j.trac.2020.116067.

[168] S. Ryu *et al.*, "Atmospheric Oxygen Binding and Hole Doping in Deformed Graphene on a SiO2 Substrate," *Nano Letters,* vol. 10, no. 12, pp. 4944-4951, 2010/12/08 2010, doi: 10.1021/nl1029607.

[169] S. D. Costa, J. E. Weis, O. Frank, M. Fridrichová, and M. Kalbac, "Monitoring the doping of graphene on SiO 2/Si substrates during the thermal annealing process," *Rsc Advances,* vol. 6, no. 76, pp. 72859-72864, 2016.

[170] J. C. Meyer, A. K. Geim, M. I. Katsnelson, K. S. Novoselov, T. J. Booth, and S. Roth, "The structure of suspended graphene sheets," *Nature,* vol. 446, no. 7131, pp. 60-63, 2007/03/01 2007, doi: 10.1038/nature05545.

[171] K. I. Bolotin, K. J. Sikes, J. Hone, H. L. Stormer, and P. Kim, "Temperature-dependent transport in suspended graphene," *Physical review letters,* vol. 101, no. 9, p. 096802, 2008.

[172] J. E. Lee, G. Ahn, J. Shim, Y. S. Lee, and S. Ryu, "Optical separation of mechanical strain from charge doping in graphene," *Nature communications,* vol. 3, no. 1, p. 1024, 2012.

[173] H. Chen *et al.*, "A cation–π interaction confined graphene oxide membrane for separation of light paraffins and olefins," *Chemical Communications,* 10.1039/D3CC00619K vol. 59, no. 35, pp. 5257-5260, 2023, doi: 10.1039/D3CC00619K.

[174] J. C. Kotsakidis *et al.*, "Freestanding n-Doped Graphene via Intercalation of Calcium and Magnesium into the Buffer Layer–SiC(0001) Interface," *Chemistry of Materials,* vol. 32, no. 15, pp. 6464-6482, 2020/08/11 2020, doi: 10.1021/acs.chemmater.0c01729.

[175] V. N. Petrova and C. A. Russell, "The evolution of seasonal influenza viruses," *Nature Reviews Microbiology,* vol. 16, no. 1, pp. 47-60, 2018.

[176] N. S. Laursen and I. A. Wilson, "Broadly neutralizing antibodies against influenza viruses," *Antiviral research,* vol. 98, no. 3, pp. 476-483, 2013.

[177] N. S. Lipman, L. R. Jackson, L. J. Trudel, and F. Weis-Garcia, "Monoclonal Versus Polyclonal Antibodies: Distinguishing Characteristics, Applications, and Information Resources," *ILAR Journal,* vol. 46, no. 3, pp. 258-268, 2005, doi: 10.1093/ilar.46.3.258.

[178] A. Vojdani, E. Vojdani, A. L. Melgar, and J. Redd, "Reaction of SARS-CoV-2 antibodies with other pathogens, vaccines, and food antigens," *Frontiers in Immunology,* Original Research vol. 13, 2022.

[179] H. H. Garcia *et al.*, "Low sensitivity and frequent cross-reactions in commercially available antibody detection ELISA assays for Taenia solium cysticercosis," *Tropical Medicine & International Health,* https://doi.org/10.1111/tmi.13010 vol. 23, no. 1, pp. 101-105, 2018/01/01 2018, doi: https://doi.org/10.1111/tmi.13010.

[180] H. K. Yoon and T. H. Yoo, "A novel protease activity assay method based on an engineered autoinhibited protein using an enzyme-linked immunoassay," *Analyst,* vol. 138, no. 23, pp. 7164-7168, 2013.

[181] C. López-Otín and C. M. Overall, "Protease degradomics: a new challenge for proteomics," *Nature reviews Molecular cell biology,* vol. 3, no. 7, pp. 509-519, 2002.

[182] H.-D. Jakubke, P. Kuhl, and A. Könnecke, "Basic Principles of Protease-Catalyzed Peptide Bond Formation," *Angewandte Chemie International Edition in English,* https://doi.org/10.1002/anie.198500851 vol. 24, no. 2, pp. 85-93, 1985/02/01 1985, doi: https://doi.org/10.1002/anie.198500851.

[183] P. Kasperkiewicz, M. Poreba, K. Groborz, and M. Drag, "Emerging challenges in the design of selective substrates, inhibitors and activity-based probes for indistinguishable proteases," *The FEBS journal,* vol. 284, no. 10, pp. 1518-1539, 2017.

[184] C. Paththamperuma and R. C. Page, "Fluorescence dequenching assay for the activity of TEV protease," *Analytical Biochemistry,* vol. 659, p. 114954, 2022.

[185] T. Liu, S. Luo, P. Libby, and G.-P. Shi, "Cathepsin L-selective inhibitors: A potentially promising treatment for COVID-19 patients," *Pharmacology & Therapeutics*, vol. 213, p. 107587, 2020/09/01/ 2020, doi: https://doi.org/10.1016/j.pharmthera.2020.107587.